INFORMATION TO USERS

This manuscript has been reproduced from the microfilm master. UMI films the text directly from the original or copy submitted. Thus, some thesis and dissertation copies are in typewriter face, while others may be from any type of computer printer.

The quality of this reproduction is dependent upon the quality of the copy submitted. Broken or indistinct print, colored or poor quality illustrations and photographs, print bleedthrough, substandard margins, and improper alignment can adversely affect reproduction.

In the unlikely event that the author did not send UMI a complete manuscript and there are missing pages, these will be noted. Also, if unauthorized copyright material had to be removed, a note will indicate the deletion.

Oversize materials (e.g., maps, drawings, charts) are reproduced by sectioning the original, beginning at the upper left-hand corner and continuing from left to right in equal sections with small overlaps.

ProQuest Information and Learning
300 North Zeeb Road, Ann Arbor, MI 48106-1346 USA
800-521-0600

UMI®

Corrosion of GaAs: Band Bending and Decomposition Mechanism

by

Yin Huang ©

A thesis submitted to the Faculty of Graduate Studies and Research in partial fulfillment of the requirements for the degree of Doctor of Philosophy

in

Material Engineering

Department of Chemical & Materials Engineering

Edmonton, Alberta

Spring 2005

Abstract

Although GaAs has been widely used in industry, such as manufacturing of opto/ microelectronic devices, its susceptibility to corrosion in damp or aqueous environment is a major problem hindering its further utilization in solar cell development. The corrosion is directly related to the chemical and (photo-) electrochemical nature of GaAs, which mainly includes the band bending at the interface and the mechanism of corrosion.

In this thesis, the corrosion of GaAs was investigated by several electrochemical methods in combination with surface characterization techniques, including optical microscopy, scanning electron microscopy (SEM) and X-ray photoelectron spectroscopy (XPS), in two solutions: 0.5 M H_2SO_4 and 2.7 M NH_4OH. Open circuit potentials, steady-state polarization curves, direct Mott-Schottky measurements and electrochemical impedance spectroscopy were performed on a series of *n*- and *p*-GaAs samples with different doping levels. Morphologies and chemical compositions of the corroded surfaces were then examined.

Open circuit potential studies of GaAs showed that the GaAs / aqueous electrolyte interface was not a simple ideal case. Both the GaAs itself (*i.e.*, doping type and level) and the solution composition influenced the open circuit potentials, which implies that the Fermi energy level of GaAs is only partially pinned by the redox couples in the solution. From the collected polarization curves, the Tafel slope for *n*-GaAs was ~350-400 mV which is unexpectedly large. The breakdown of *n*-GaAs was explained by an avalanche mechanism, through comparison of theoretical calculations and experimental results. Earlier breakdown than expected, based on theoretical calculations, was explained as being due to surface defects, resulting in a locally high electric field.

Flatband potentials from direct Mott-Schottky measurements and impedance spectra were compared and discussed. The frequency dependence in the Mott-Schottky measurements was explained to be due to modeling with an inadequate equivalent circuit. In addition, the surface characterization results suggested that corrosion in 0.5 M H_2SO_4 was Ga selective, but less so in 2.7 M NH_4OH. Based on the impedance results, the corrosion mechanism was identified as being the so-called X-C type, with the corrosion intermediates being the oxidant for further oxidation. The mechanism was simulated mathematically.

Acknowledgements

The past four years have been one of the most incredible times of my life. This Ph.D. program had a great impact on me in the way how to think, how to learn and also how to look ahead. I have gained much, much more than what I anticipated. Many people have helped me in various ways and gave me the strength to keep on. Without them, this thesis would not be possible.

Firstly, I am grateful to have Prof. Douglas G. Ivey and Prof. Jingli Luo to be my supervisors. The research work was based on their excellent cooperation with numerous problems solved. I have learned a lot from Prof. Ivey on the surface characterization techniques and from Prof. Luo, every discussion was casting light on the further work. I truly appreciate their patience in allowing me to be an independent researcher. They are exceptional scientists.

I am thankful to have so many talented group members to stay along with. Dr. A. He has done me a big favor in SEM and TEM surface analysis. Mr. C. Yang and Mr. Y.M. Zeng, Dr. J.G. Yu and Dr. H.Y. Ma are great friends to study and work. Quite a few heated discussions are really helpful to the research and also our daily lives. I am also indebted to Mr. G.S. Weng for his work in this project. Thanks are also given to Ms. X. Pang, Ms. X. Lin, Dr. B.T. Lu, Mr. C.W. Chen, and Mr. A. Lu who have made my life colorful.

I am indebted to the help from the department staffs. Without them everything could not be so smooth.

Thanks to the Natural Science and Engineering Research Council (NSERC) for financial support and Nortel Network Works for all GaAs samples.

Finally, I would like to dedicate this thesis to my family. My parents have always supported me in my life, although I have been back to visit them for several years. Continuous support and encouragement from wife is sincerely appreciated with my whole heart. And with my lovely spirit, our newborn daughter, Mulan, everything makes sense.

Table of Contents

List of Figures

List of Tables

List of Symbols

E	energy of electronic states (eV)
$F(E)$	the probability that an electronic state with energy E is occupied by electron
E_F	Fermi energy level (eV)
E_C	energy of the bottom of conduction band (eV)
E_V	energy of the top of the valence band (eV)
E_C^S	energy of the bottom of conduction band at the surface (eV)
E_V^S	energy of the top of the valence band at the surface (eV)
E_g	band gap (eV)
E_i	intrinsic energy level
$E_{F,n}$	quasi Fermi energy level for electrons
$E_{F,p}$	quasi Fermi energy level for holes
k	Boltzmann constant (J K^{-1} mol^{-1})
T	absolute temperature (K)
n	density of electrons in CB (cm^{-3})
p	density of holes in VB (cm^{-3})
n_0	density of electrons in CB at thermal equilibrium (cm^{-3})
p_0	density of holes in VB at thermal equilibrium (cm^{-3})
n_s	density of electrons in CB at the surface (cm^{-3})
p_s	density of holes in VB at the surface (cm^{-3})
n_i	intrinsic density of electron or hole (cm^{-3})
Δn	density of excessive electrons (cm^{-3})
Δp	density of excessive hole (cm^{-3})
N_C	effective density of states of the CB (cm^{-3})
N_V	effective density of states of the VB (cm^{-3})
N_D	donor concentration (cm^{-3})
N_A	acceptor concentration (cm^{-3})
n_{eff}	effective doping density

e^-	electron
h^+	hole
e	electron charge, 1.60×10^{-19} C
h	Plank constant, 6.63×10^{-34} J s
m	number of the electrons involved in an electrochemical reaction
O	oxidation state for a redox couple
R	reduction state for a redox couple
v	electrochemical reaction rate (mol l^{-1} s^{-1})
k_f	forward reaction rate constant
k_b	backward reaction rate constant
k_f^{eq}	forward reaction rate constants at the equilibrium potential
k_b^{eq}	backward reaction rate constants at the equilibrium potential
β	symmetry factor which measures the influence of the change of potential on the activation energy of both the forward and backward reactions
β_n	kinetic rate constants for the recombination process
β_p	kinetic rate constants for the hole capturing process
β_a	factor to convert surface coverage to surface concentration
η	overpotential
R	gas constant, 8.314 J K^{-1}
V_{app}	applied potential to the electrode
V_{eq}	equilibrium state electrode potential
$_nE_{decomp}$	cathodic decomposition potential
$_pE_{decomp}$	anodic decomposition potential
I	current
j	current density
A	electrode surface area
F	Faraday's constant, 96500 C mol^{-1}
j_{dl}	charging current density of double layer capacitor
t	time

φ_{SC}	potential drop across the space charge region
φ_H	potential drop across the Helmholtz layer
φ_{SS}	potential drop across the surface states
ϕ_b	band bending in the space charge region
V_o	internal Schottky barrier height
V_{fb}	flatband potential
V_{fb}^*	flatband potential measured at altered conditions, refer to the normal conditions
ΔV_{fb}	the change of flat band potential, $\Delta V_{fb} = V_{fb}^* - V_{fb}$
V_{br}	breakdown potential
V_{inv}	potential at which inversion layer forms
N	donor or acceptor concentration
ε_0	permittivity of a vacuum, 8.85×10^{-12} F m^{-1}
ε_{SC}	dielectric constant of the semiconductor in space charge region
j_v	valence band current density
j_c	conduction band current density
$j_{v,0}$	exchange valence band current density
$j_{c,0}$	exchange conduction band current density
P_{AB}	partial pressure for compound AB
$[AB]$	concentration of species AB
$C_{O,S}$	concentrations of O at the surface
$C_{R,S}$	concentrations of R at the surface
$[ess]$	surface concentration of empty surface states
θ	surface coverage of adsorbates
f	frequency used in ac electrochemical methods
R	resistance
R_S	serial or solution resistance
RC	the electrical circuit of a resistor in series with a capacitor
R_{MS}	serial resistance in the equivalent circuit used in direct Mott-Schottky measurement

C_{MS}	capacitance in the equivalent circuit used in direct Mott-Schottky measurement
R_{ct}	electrochemical resistance due to charge transfer
C_{dl}	double layer capacitance ($\mu F\ cm^{-2}$)
C_H	capacitance of Helmholtz layer ($\mu F\ cm^{-2}$)
C_{diff}	capacitance of diffuse layer ($\mu F\ cm^{-2}$)
C_{SC}	capacitor of the space charge region ($\mu F\ cm^{-2}$)
C_{SS}	capacitance of surface states
$R_{r,1},\ R_{r,2},\ C_R$	circuit elements in fitting recombination impedance
Z	impedance
Z'	real part of impedance
Z''	imaginary part of impedance
Z_{theo}	theoretical impedance calculated from equivalent circuit
Z'_{theo}	real part of the theoretical impedance calculated from equivalent circuit
Z''_{theo}	imaginary part of the theoretical impedance calculated from equivalent circuit
Z_F	Faradaic impedance
S_N	the sum to minimize in impedance fitting
v_i'	weighting coefficient for the real part in impedance fitting
v_i''	weighting coefficient for the imaginary part in impedance fitting
R_i'	residual between experimental data and theoretical prediction for the real part of impedance
R_i''	residual between experimental data and theoretical prediction for the imaginary part of impedance
NN	number of impedance data from experiments
a	Tafel intercept
b	Tafel slope
ω	angular frequency
i	equal to root of -1
P	tunneling probability

m^*	effective mass of electrons
W	width of the space charge region
E_{br}	breakdown electrical field

List of Abbreviation

CB	conduction band
VB	valence band
OCP	open circuit potential
NHE	normal hydrogen electrode
SCE	saturated calomel electrode
SHE	standard hydrogen electrode
CT	charge transfer
CV	current-voltage relationship
IMPS	intensity modulated photocurrent spectroscopy
EIS	electrochemical impedance spectroscopy
RRDE	rotating ring-disk electrode
PL	photoluminescence
HER	hydrogen evolution reaction
XPS	X-ray photoelectron spectroscopy
SEM	scanning electron microscopy
EDX	energy dispersive X-ray spectroscopy
SE	secondary electron
CNLS	complex non-linear least square
PFM	peak fitting module included in commercial software Microcal$^{\copyright}$ Origin^{TM}.

Chapter 1   Introduction

1.1 Why study gallium arsenide

Semiconductors play a very important role in daily life. From diodes to transistors, from radio to television to computers based on VLSI (very large scale integrated) technology, they are indispensable in industry and also for entertainment. The last five decades have been the era of silicon (Si), because it is the leading actor among the semiconductor family [1-3]. However, interest in other semiconductors, mainly III-V compound semiconductors, has grown due to the physical and chemical property limits of Si. Gallium arsenide (GaAs) is one type of III-V semiconductor.

Perhaps the primary benefit of GaAs, compared to Si, is its dynamic electron properties. The effective mass[1] of the electrons in GaAs is far less than that in Si (Appendix B). This implies that for the same external conditions, the electrons in GaAs can be accelerated to higher velocities and thus respond quicker to a change in applied conditions [1-3]. This difference enables devices operating under higher frequencies with faster switching speeds. In addition, GaAs has a direct band gap, making optoelectronic devices possible, which were not available with Si and germanium (Ge)[2].

---

[1] Effective mass of charge carriers in semiconductors is one parameter calculated from the band structure based on quantum mechanics theory. Band structure can be referred to Chapter 2 (Figure 2-3).

[2] In recent years, scientists have succeeded in modifing (adjusting) the band structure of Si, Ge and other semiconductors, particularly on the nanoscale. Optoelectronic devices based on these semiconductors are possible now, *e.g.* reference [4].

1

The breakthrough in growth and fabrication techniques for GaAs was driven by the defense and space industries, including higher frequency circuits for radar, secure communications and sensors. Mature GaAs techniques introduced new commercial markets: wireless local area networks (WLANs), personal communication systems (PCSs), direct broadcasting satellites (DBS) for transmission and reception by the consumer, global positioning systems (GPSs) and global cellular communication (GaAs MANTECH, http://gaasmantech.org).

1.2 Problems with GaAs

GaAs-based optoelectronic and microelectronic device manufacturing has been a great success. There are several issues with GaAs, however. There is less understanding of reliability and failure issues for GaAs (http://gaasmantech.org). GaAs is expensive to prepare and fabricate, and many chemical and electrochemical problems are encountered during cleaning and oxidation [5]. Si is known to be stable, as is its oxide SiO_2. However, GaAs is easily oxidized by oxygen in air and its oxides are porous and not good insulators. When GaAs is in contact with water, decomposition, adsorption and corrosion happen spontaneously [6-8]. All of these degrade the performance of GaAs, leading to earlier breakdown and larger resistivity. Recently, corrosion problems on GaAs have attracted more and more attention [9]. It was realized that the corrosion of GaAs is a valence band electrochemical process; the hole concentration at the surface is the most essential parameter to characterize both the thermodynamic stability and the kinetic corrosion rate. The concentration of charge carriers at the GaAs surface is directly related to the flatband potential and band bending, which are still not fully understood [10].

1.3 Organization of this thesis

Thermodynamically, the stability of GaAs depends on the doping level, surface conditions and operating environments. Kinetic corrosion rates also rely on these conditions. The aim of this thesis is to analyze how the stability and corrosion are related

2

to typical conditions used in industry, mainly in strong acidic solutions. Following this chapter are background information and a literature review, presenting general knowledge and details of GaAs corrosion. Chapter 3 gives the experimental conditions used in this work. The results generated by various techniques (normal electrochemical and photoelectrochemical methods and surface characterization techniques) are given in Chapter 4, followed by a comprehensive discussion (Chapter 5) on open circuit potential, polarization curves, breakdown, corrosion mechanism, surface pretreatments and band bending. Chapter 6 consists of Conclusions and possible Future Work.

References:

[1]   Zeghbroeck, B. V. *Principles of Semiconductor Devices*; http://ece-www.colorado.edu/~bart/book/: 2004.

[2]   Sze, S. M. *Semiconductor Devices, Physics and Technology*; John Wiley & Sons: 2002.

[3]   Singh, J. *Semiconductor Devices: Basic Principles*; John Wiley & Sons, Inc.: 2001.

[4]   Zhifeng Ding, Bernadette M. Quinn, Santosh K. Haram, Lindsay E. Pell, Brian A. Korgel, and Allen J. Bard, *Science*, 296, **2002**, 1293.

[5]   Quirk, M. *Semiconductor manufacturing technology*; Prentice Hall: Upper Saddle River, NJ, 2001.

[6]   Bard, A. J. and Wrighton, M. S., *J. Electrochem. Soc.* **1977**, 124, 1706.

[7]   Gerischer, H., *Faraday Discussion* **1981**, 70, 137.

[8]   Gerischer, H., *J. Electroanal. Chem.* **1977**, 82, 133.

[9]   Schmuki, P., Fraser, J., Vitus, C. M., Graham, M. J. and Isaacs, H. S., *Localized Corrosion of GaAs Surfaces and Formation of Porous GaAs*, in *Critical Factors in Localized Corrosion II*, Natishan, P. M., et al., Editors. 1996, The Electrochemical Society. p. 226.

[10] Gengsheng, W., *Corrosion Behavior of GaAs*, in *Department of Chemical & Materials Engineering*. 2002, University of Alberta: Edmonton.

Chapter 2   Background and literature review

This chapter starts with a general description of semiconductor physics and electrochemistry / photoelectrochemistry. Building on this, a comprehensive review on the latest development in GaAs corrosion / decomposition are presented. After a brief discussion of the problems, the objectives of this thesis are then proposed.

2.1 General knowledge of semiconductor (GaAs) and semiconductor physics

Why study semiconductors? What kind of materials can be called semiconductors? What is the difference between semiconductors and metals? How does a semiconductor work? This section will briefly answer the above questions to give an overall picture of the semiconductor world, facilitating understanding of this thesis.

2.1.1 GaAs as a semiconductor

The definition of a semiconductor came from the classification of materials by electrical resistivity or conductivity. As is known, metals are good electrical conductors and insulators are not. For example, copper (Cu) has been used to manufacture wires and cables, while ceramics and plastics are used as electrical sockets for safety reasons. Semiconductors have electrical conductivities in between conductors and insulators. Quantitatively, the electrical resistivities ρ of these three different materials are listed in Table 2-1.

4

GaAs is a III-V compound semiconductor composed of the Group IIIA element gallium (Ga) and the Group VA element arsenic (As). First reports on GaAs appeared in the late 1920s, but the electronic properties of III-V compound semiconductors were not studied until the 1950s. The GaAs crystal consists of two face-centered cubic sublattices, with relative offset of one quarter of the diagonal of the cube (Figure 2-1). This crystal structure is known as zinc blende and is responsible for the semi-conducting behavior of GaAs, because of the strong covalent bonds between Ga and As (tetragonal coordination). The zinc blende structure prevails in most compound semiconductors, *e.g.*, InAs, GaP, and InP. Compound semiconductors can also result from the bonding between Group II and Group VI elements (ZnS, ZnO, CdS, ZnSe) or between Group IV and Group VI elements (PbS, PbSe). There are also ternary or quaternary compound semiconductors containing three or more elements in the compound *e.g.*, GaAsP, InGaAsP, AlGaAs, etc.

Being a semiconductor, GaAs possesses the special chemical and physical properties. For example, the conductivity of GaAs is a strong function of temperature and is very sensitive to impurities; the resistivity can be decreased by illumination. Two kinds of charge carriers exist in semiconductors: electrons and holes.

2.1.2   Basics of semiconductor physics

2.1.2.1   Band model

From the laws of quantum mechanics, the electron energy of an isolated atom can have only discrete values. When many atoms are brought together, the discrete energy levels in each atom overlap and degenerate to form new energy levels with smaller gaps. For a crystal with numerous atoms, this energy gap between certain energy levels is so small that at room temperature electrons can be easily excited by vibration and these energy levels can be treated as continuous levels, the so-called band. Similar to the HOMO (highest occupied molecule orbital) and LUMO (lowest unoccupied molecule orbital) for the formation of a molecule at absolute zero temperature, the highest occupied band in the crystal is called the valence band (VB) and the lowest unoccupied band is

5

called the conduction band (CB). These two bands are separated by an energy gap, called the band gap (E_g), which is characteristic of the material. For example, for metals, the highest occupied band is only half filled and there is no band gap. For GaAs, the band gap is around 1.42 eV at room temperature, which is in the range of visible light photon energy. Under normal conditions, there are only a few electrons that can acquire enough energy to be excited from the VB to the CB, resulting in poor conductivity for semiconductors.

The band model is the basis of all semiconductor physics and also applies to insulators, in which most of the bonds are also covalent. The only difference between a semiconductor and an insulator is that E_g is smaller for the semiconductor than for the insulator. Thus under some conditions, *e.g.*, exposure to light, the energy gap can be overcome for the semiconductor and it shows conducting behavior, called photoconductivity. The band model can also explain the special electrical characteristics: when the temperature increases, the electrons obtain more kinetic energy and have a higher probability to overcome the energy gap and thus the electrical resistivity decreases.

2.1.2.2 Charge carriers

In metalic crystals, electrons are the only charge carriers because the metal ions are localized and only the electrons are free. But in semiconductors and insulators, the electrons in the valence band are more localized and cannot be treated as an electron gas. If one electron is excited by some extra energy from one atom and forms a so-called hole, then this atom may try to capture an electron from its adjacent atom to fill the hole due to its instability and high energy. This repeating process is the same behavior as the random movement of a positive charge (hole). Based on this, a hole is treated as another charge carrier in semiconductors or insulators, in addition to the electrons. For a semiconductor, if electrons are the majority charge carrier, which means the number of electrons is more than the numbers of holes, the semiconductor is considered to be *n*-type. If holes are the majority charge carrier, the semiconductor is *p*-type.

6

2.1.2.3 Doping

For a pure Si crystal, the number of electrons and holes must be the same because the crystal should be neutral. The semiconductor is called intrinsic. If impurities are added, such as phosphors (P), which has five outer shell electrons, there are more electrons than required for covalent bonding. Hence, a P-doped Si semiconductor is *n*-type. On the other hand, when Si is B-doped (boron, three outer shell electrons) excess holes are created with the B anions, resulting in *p*-type Si. The doped semiconductor is also called an extrinsic semiconductor. In the band model concept, the adding of impurities into the intrinsic semiconductor introduces new energy levels. Such impurity levels can be conveniently separated into donors, which donate electrons, generally to the conduction band, and acceptors, which accept electrons and either create holes in the valence band or extract electrons from conduction band (illustrated in Figure 2-2). Some dopants can be either donors or acceptors, and these are called amphoteric dopants. This only applies to compound semiconductors. For example, Si doped GaAs can be either p-type or n-type. If Si replaces Ga in the GaAs crystal structure, it is *n*-type because of excess electrons. If Si replaces As in GaAs, it is *p*-type because of excess holes.

2.1.2.4 Fermi energy level

When the electrons in a semiconductor are in thermodynamic equilibrium, the probability that an electronic state with energy E is occupied by electron is given by the Fermi-Dirac distribution function:

$$F(E) = \frac{1}{\exp\left(\dfrac{E - E_F}{kT}\right) + 1} \tag{2.1}$$

where k is the Boltzmann constant, T is the absolute temperature and E_F is the Fermi energy level. The probability of occupation by an electron is exactly 0.5 at $T = 0K$. The significance of E_F can be found from the electron distribution at 0K. No thermal excitation happens at absolute zero, which suggests that all energy level states under E_F

7

are filled, and all energy states above E_F are empty. In fact, in electrochemistry, the Fermi level for a redox pair is the same as the equilibrium redox potential.

In the semiconductor band structure, the Fermi energy level is usually located in the forbidden region, between the CB and the VB ($E_v < E_F < E_c$). Generally, the difference between E_F and E_v or E_c is larger than kT, and then the probability of electron occupation in the CB or the probability of hole occupation in the VB is simplified to the Boltzman distribution.

In the CB:

$$F(E) = \exp\left(\frac{E_F - E}{kT}\right) \tag{2.2}$$

In the VB:

$$1 - F(E) = \exp\left(\frac{E - E_F}{kT}\right) \tag{2.3}$$

From Eqs (2.2) and (2.3), one can show that in the CB electrons are mainly distributed close to the CB bottom edge and in the VB holes are mainly distributed closed to the VB top edge. The density of electrons (number of electrons per unit volume) in the CB and the density of holes (number of holes per unit volume) in the VB can be written as:

$$n = N_c \exp\left(\frac{E_F - E_c}{kT}\right) \tag{2.4}$$

$$p = N_v \exp\left(\frac{E_v - E_F}{kT}\right) \tag{2.5}$$

where n is the density of electrons in the CB and p is the density of holes in the VB. N_c and N_v are the effective density of states of the CB and the VB, respectively. The following can also be determined:

$$np = N_c N_v \exp\left(-\frac{E_g}{kT}\right) = n_i^2 \tag{2.6}$$

8

where n_i is the intrinsic density of electrons or holes and it only relies on the nature of the semiconductor and temperature. Eq. (2.6) is commonly used to calculate the density of minority carriers in doped semiconductors, because the density of majority carriers can be determined from the doping concentration if full ionization of the dopant is assumed.

2.1.2.5 Differences between Si and GaAs

This comparison is aimed to give a direct picture why Si cannot replace GaAs in the semiconductor industry. All the differences in properties arise from the distinctive band structure [1] (Figure 2-3). The shape of the VB of the two semiconductors is quite similar; however, different CB structures can be found. Firstly, GaAs has a direct band gap; the minimum of the CB is directly over the maximum of the VB. This enables a direct transition for electrons from the VB to the CB by absorbing a photon with enough energy in GaAs. This property is very important to GaAs as it can be used to make light emitting diodes and semiconductor lasers. Alternatively, GaAs can be used as a photon detector by measuring the current flowing due to electrons excited by incident light. For Si, a combination of photons and phonons (to alter the momentum) must be absorbed for a transition from the VB to the CB and this results in a very low efficiency. Secondly, the curvature of the CB minimum and VB maximum of the band are directly related to the effective mass of the charge carriers. The curvature of the GaAs CB bottom is obviously much sharper than that for Si, indicating that the electrons in GaAs are much lighter than in Si (Appendix B). Therefore, another advantage of GaAs versus Si is that GaAs-based devices can respond faster than Si-based devices and thus can meet higher-frequency requirements.

Despite the superior advantages over Si, some difficulties remain in GaAs-based device fabrication. Compared to the oxide of Si (SiO_2), a natural compact insulator, oxides of GaAs are porous and cannot be used to separate layers during lithography. Another problem is the stability of GaAs. It has been found that GaAs will decompose and degrade its performance when it is exposed to an aqueous environment. Corrosion is

9

likely to occur on the GaAs surface. This shortcoming also hampers the development of GaAs-based solar cells.

2.2 (Photo)electrochemistry of semiconductors

As mentioned above, corrosion is a major problem in using GaAs to produce devices such as solar cells. Below is a brief overview of relevant knowledge of corrosion.

2.2.1 Overview of electrochemistry related to corrosion

2.2.1.1 Electrochemical interface

Classically, corrosion is defined as the "destructive result of chemical reaction between a metal or metal alloy and its environment" [2]. This definition can be extended to semiconductors. Corrosion is considered to be destructive and undesirable because the material is corroded and wasted. However, corrosion can directly or indirectly produce a positive end result if the process is under control. A typical controlled-corrosion process is etching, which is widely used in the characterization and analysis of metals/alloys. For example, the fabrication process for making circuit boards consists of etching of copper and other metals selectively to produce circuit traces.

Nearly all corrosion processes in aqueous environments involve transfer of electronic charge in aqueous solutions, indicating the electrochemical nature of corrosion. For example, the corrosion of Zn in neutral aqueous solution follows these electrochemical reactions:

$$Zn - 2e^- \rightarrow Zn^{2+} \qquad \text{anode reaction} \qquad (2.7)$$

$$O_2 + 4e^- + 4H^+ \rightarrow 2H_2O \qquad \text{cathode reaction} \qquad (2.8)$$
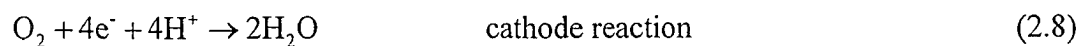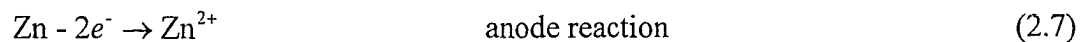
The above also applies to the corrosion of semiconductors, e.g., for GaAs exposed to light in acid solutions:

10

$$GaAs + 3H_2O + 6h^+ \rightarrow Ga^{3+} + H_3AsO_3 + 3H^+ \qquad (2.9)$$
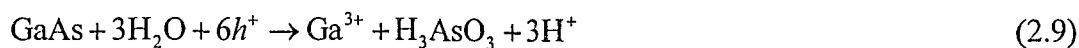
Since photons are involved in this process, it is called photocorrosion, which is only inherent to semiconductors.

(Photo)corrosion is an interfacial phenomenon. The interface in electrochemistry in general refers to the special region where the electrode and the electrolyte contact. A typical interface established between a metal electrode and an aqueous electrolyte is shown in Figure 2-4. The common name for the interfacial region is the "double-layer", which arises from the first theory to describe this charged interphase region by Helmholtz in the 19th century. As a simple picture, it was imagined that the excess charges on the metal side are balanced by an equal number of excess charges, also arranged to be all in one plane, on the solution side. The double-layer behaves as a simple parallel-plate capacitor.

In this model (Figure 2-4) [3], the solution side of the double-layer is made up of several "layers". The layer closest to the electrode is the inner layer, containing solvent molecules and sometimes other species (ions or molecules) that are called specifically adsorbed species. This inner layer is also called the compact layer or Helmholtz layer. The locus of the electrical centers of these specifically adsorbed species is called the inner Helmholtz plane (IHP). The solvated ions can only approach to the outer Helmholtz plane (OHP). The interaction of the solvated ions with the electrode involves only long-range electrostatic forces, independent of the chemical properties of the ions and the electrode. These ions are said to be nonspecifically adsorbed. Due to thermal agitation in the solution, the nonspecifically adsorbed ions are distributed in a 3-dimensional region, called the diffuse layer, extending from the IHP into the bulk of the solution. The thickness of the diffuse layer depends on the total ionic concentration of the electrolyte solution. For the above model, the equivalent circuit of the double-layer can be considered to be two capacitors in series:

$$\frac{1}{C_{dl}} = \frac{1}{C_H} + \frac{1}{C_{diff}} \qquad (2.10)$$

11

where C_H is the capacitance of the Helmholtz layer and C_{diff} is the capacitance of the diffuse layer.

2.2.1.2 Electrochemical kinetic equation

Consider the simple electrochemical reduction reaction (first-order):

$$O + me^- \underset{k_b}{\overset{k_f}{\rightleftharpoons}} R \qquad (2.11)$$

where m is the number of electrons involved, k_f and k_b are forward and backward reaction rate constants, respectively. The reaction rate can be expressed as:

$$v = k_f C_{O,S} - k_b C_{R,S} \qquad (2.12)$$

where $C_{O,S}$ and $C_{R,S}$ are the concentrations of O and R species at the surface, respectively. Since this is an electrochemical reaction, the rate constants are dependent on the electrode potential. This is also a main characteristic of an electrochemical reaction where the reaction rate is adjustable by an external applied potential to the electrode. The relationship of the rate constants with the applied potential for reaction (2.11) can be written as:

$$k_f = k_f^{eq} \exp\left(-\frac{\beta F \eta}{RT}\right) \qquad (2.13)$$

$$k_b = k_b^{eq} \exp\left(\frac{(1-\beta) F \eta}{RT}\right) \qquad (2.14)$$

where k_f^{eq} and k_b^{eq} are the forward and backward reaction rate constants at the equilibrium potential, respectively, β is the symmetry factor which measures the influence of the change of potential on the activation energy of both the forward and backward reactions, and η is the overpotential which is the potential difference between the applied electrode potential and the equilibrium state electrode potential ($\eta = V_{app} - V_{eq}$). In electrochemistry, conventional experiments measure the relationship of current or current density of the system with the change in applied electrode potential. The current is actually proportional to the reaction rate:

12

$$I = -nFAv \tag{2.15}$$

or

$$j = -nFv \tag{2.16}$$

where I is the current, j is the current density, n is the number of electrons involved in the reaction, A is the electrode surface area, and F is Faraday's constant. Thus, for reaction (2.11), the relationship between current density and the electrode potential is:

$$j = -nF\left[k_f^{eq} C_{O,S} \exp\left(\frac{-\beta F\eta}{RT}\right) - k_b^{eq} C_{R,S} \exp\left(\frac{(1-\beta)F\eta}{RT}\right) \right] \tag{2.17}$$

Eq. (2.17) is also called the Butler-Volmer equation.

2.2.1.3 Equivalent circuit model of the interface

As mentioned above, the double layer interface can be treated as two capacitors in series if no electrochemical reactions take place. This concept can be expanded. The electrode and electrolyte junction behave like a black box, in which potential or current is applied and the current or potential response of the black box is studied. Apparently, the current response under an applied potential consists of two parts: double layer charging and electrochemical reactions. The double layer charging process is similar to a capacitor charging or discharging with the potential change:

$$j_{dl} = C_{dl} \frac{dV_{app}}{dt} \tag{2.18}$$

The current response of the electrochemical reactions can be handled with Eq. (2.17). Thus a simplified equivalent circuit of the electrochemical interface is a double layer capacitor in parallel with the impedance of the electrochemical reactions (Figure 2-5). Further information can be obtained from references [3-5].

13

2.2.2 Electrochemistry and photoelectrochemistry of semiconductors

Similar to the interface in electrochemistry of metals, the electrochemistry / photoelectrochemistry of semiconductors also focuses on the interface between the semiconductor and electrolyte. A classical textbook on semiconductor electrochemistry is from Morrison [6] and more recent work and progress in this field can be obtained from review papers [7-10] or chapters in the recent book by Memming [1].

2.2.2.1 Space charge layer

In electrochemistry, the energy level of a solution is represented by the reduction/oxidation (redox) potential. To describe the semiconductor/electrolyte interface, the Fermi energy level of a solution must be defined. The electrochemical redox potential of a solution is always a relative value, commonly to a reference electrode, *i.e.*, normal hydrogen electrode (NHE) or saturated calomel electrode (SCE). Researchers have tried to accurately measure the absolute potential of the NHE so that the redox potential of a solution can be comparable to the Fermi energy level of metals/semiconductors. It has been calculated by several groups to be 4.44±0.02 V. However, the potential is widely accepted to be 4.5V, calculated by Lohmann because this value has been quoted by Gerischer, whose reviews are read by most semiconductor electrochemists [7].

The situation of a semiconductor/electrolyte contact is shown in Figure 2-6. Since the redox potential of a solution is constant for a certain concentration or activity, after contact, the Fermi level of the semiconductor must be equal to the Fermi level of the solution at equilibrium. As there are much fewer carriers in the semiconductor than in a metal, the contact potential can develop very deeply (1-100 μm) into the bulk of the semiconductor, resulting in band edge bending to prevent carrier (electrons or holes) flow

14

into the electrolyte. The layer of the band bending (from interface to bulk of semiconductor) is called the space charge layer (Figure 2-6[3]).

Therefore, the interface structure of a semiconductor/electrolyte is more complicated than the double layer model used for a general metal/electrolyte interface. The interface is now divided into three layers: the space charge layer under the semiconductor surface, the Helmholtz compact layer and the diffusion layer on the solution side.

Under an applied potential, there are three forms of space charge layer that can be obtained on a semiconductor, in contact with metal or electrolytes or surface states, *e.g.*, absorption (Figure 2-7). The band bending discussed above is the case of natural band bending when the semiconductor is in contact with a metal or an electrolyte with redox pairs. The space charge layer formed in this situation is called "a depletion layer". For example, in an *n*-type semiconductor where the majority charge carriers are electrons, electrons in the CB have a tendency to flow into the solution side (electrolyte) or metal, since the electrons in the semiconductor have a higher potential energy. The band bending formation is to prevent a continuous flow of the electrons from the semiconductor. As a result, at equilibrium the surface region is "depleted" of majority carriers. Minority carriers are not present (swept out of the region by the electric field), and only the unmovable ions are left (Figure 2-7a).

An inversion layer is formed when excess majority carriers are extracted so that the majority carrier band (for *n*-type, it is the CB, and for *p*-type, the VB) cannot supply all the majority carriers required and carriers from the minority carrier band are needed. Thus, when charge transfer takes place at the surface, not only the majority charge carriers, but also the minority charge carriers, contribute to the current generated (Figure 2-7b). Figure 2-7c is the flat band situation, which can be produced by applied potential

---

[3] In this figure, the energy levels of the redox couples in the solution are shown as a distribution. This is due to the hydration of both redox pairs. Generally, the distribution is considered to be Gaussian. More details can be found from books on electrochemistry aspects.

15

or in the case of no contact with other materials and no surface states (*e.g.*, freshly cleaved samples in ultra-high vacuum). If the majority charge carriers are injected instead of extracted, the band bending direction will be different to depletion layer bending, indicating that the majority charge carriers accumulate in the space charge region. The surface concentration of the majority charge carriers will be higher than that in the bulk (Figure 2-7d).

2.2.2.2 Potential distribution, surface states and Mott-Schottky relationship

For a metal / electrolyte interface, the potential applied will mainly drop inside the double layer region because charges on a metal only distribute on its surface. This results in a very high electric field in the Helmholtz layer (compact layer), if the concentration of ions in the electrolyte is high enough. However, for a semiconductor / electrolyte interface, due to the existence of space charge layers, the potential applied (V_{app}) also distributes into the space charge region:

$$V_{app} = \varphi_{SC} + \varphi_{H}$$ (2.19)

φ_{SC} and φ_{H} are the potentials falling in the space charge region and Helmholtz layer, respectively. For a typical depletion situation, since the depletion region extends as deep as several hundreds of nanometers, which is much larger than the width of Helmholtz layer, capacitance of the space charge region, C_{SC}, is much smaller than C_{H}. This leads to a dominant potential portion in the depletion region, as shown in Figure 2-8.

If surface states are present and are in series with the space charge region, Eq. (2.19) should be revised to:

$$V_{app} = \varphi_{SC} + \varphi_{H} + \varphi_{SS}$$ (2.20)

where φ_{SS} represents the potential portion taken by the surface states. Surface states are related to the energy levels existing in the band gap of a semiconductor due to localized charges. The source of surface states can be various: dangling bonds, defects, adsorbates, etc. Only under vacuum conditions and for a freshly cleaved sample can a surface be

16

perfect. Based on this, surface states should be always considered in semiconductor electrochemistry. The roles that surface states play are not only the potential portion they take. They can also mediate charge transfer across the interface, *i.e.*, they offer another path for charge to travel from the electrolyte to the semiconductor or vice versa, promoting the corrosion process.

With reference to the potential distribution equation, if the potential drop in the interface is mainly constrained to the space charge region on the semiconductor side, the interface behaves like a Schottky barrier for a semiconductor/metal contact. The energy of the band edge at the surface of the semiconductor, before and after the contact with the electrolyte, is constant with respect to the Fermi level of the contact electrolyte, which is called band edge pinning. Figure 2-9 shows the different forms of band bending for a semiconductor electrode in contact with an electrolyte containing different redox couples. For the more positive redox potential of redox couple 2, the band will exhibit more bending so that the Fermi energy level of the semiconductor electrode will be the same as the potential of the redox couple. The band edge is pinned because the potential drop or contact potential developed is mainly in the space charge region. On the other hand, if the amount of surface states is large, then in the extreme situation, the contact with the electrolyte does not affect the potential drop of the space charge region. Thus, the presence of a high density of surface states on the semiconductor usually "pins" the Fermi energy level at the surface, resulting in the formation of a Schottky barrier even before contact between the semiconductor and the electrolyte (Figure 2-10). The Fermi energy level of the semiconductor will be same as that for the surface states.

The quantitative expression for the space charge region is given by the Mott-Schottky equation. This is the relationship between the capacitance of the space charge region and the band bending.

$$\frac{1}{C_{SC}^2} = \frac{2(\phi_b - kT/e)}{eN\varepsilon_0\varepsilon_{SC}} \tag{2.21}$$

where ϕ_b is the band bending of the space charge region, N is the donor or acceptor concentration, and ε_0 and ε_{SC} are the permittivity of a vacuum and dielectric constant of

17

the semiconductor in the space chare region, respectively. By defining the flatband potential V_{fb} (Eq.(2.22)), the potential applied to flatten the bent band, the relationship of the space charge region capacitance versus the applied potential can be obtained.

$$\phi_b = V_{app} - V_{fb} \qquad (2.22)$$

Assuming that the capacitance of the Helmholtz layer is much larger than C_{SC}, this equation yields the dominant impedance of the interface. Usually this relationship is used to derive the flat band potential V_{FB} and to estimate the degree of band bending.

2.2.2.3 Charge transfer across the semiconductor/electrolyte interface

Modern charge transfer (CT) theory at a semiconductor / electrolyte interface was reviewed recently by Koval and Howard [11] and Lewis [12]. A brief introduction is presented here.

Early investigations on the semiconductor /electrolyte interface used the comparable model of the semiconductor / metal contact, which is also called the Schottky contact model. In such a model, only the semiconductor side needs to be considered for successful charge transfer with respect to the work function of the metal. It should be mentioned that the famous Mott-Schottky relationship is also based on the Schottky contact model. However, when discussing the charge transfer across the semiconductor / electrolyte interface, the differences between metal and electrolyte must be distinguished:

(1)   A metal has a much higher density of electronic states distributed in continuum, compared to the far lower density of states in a restricted range of energies for an electrolyte. In most cases, a Gaussian distribution of the energy states in redox couples is used (Figure 2-6).

(2)   In a pure Schottky contact, current flows only due to charge migration and drift across the interface. For a semiconductor in an electrolyte, the interface might

18

contain adsorbates or corrosion products (*e.g.*, oxide layer), the result of which will be a drastic change in the current-voltage properties.

A model for the charge transfer between semiconductor electrodes and electrolytes was developed by Marcus and Gerischer, and reviewed by Batchelor and Hamnett [8]. Here the Gerischer model is described because it is simpler and more popular. The fundamental assumption of the theory is that electron exchange can only take place between electronic states with energies less than one k_BT difference. The Frank-Condon principle in spectroscopy is also adapted so that during the charge transfer [8], no nucleus configuration or atom momentum change can occur. Hence, it is known that overlapping of the redox electronic states with the two bands in the semiconductor will determine how fast charge transfer can happen.

If charge transfer is not relevant to the electrolyte, obviously the Schottky contact model may still be applied; for example, the case of semiconductor corrosion in indifferent electrolytes without surface states involved. The classical Schottky barrier model assumes that the band edges are fixed at the surface, that is, all potential applied is taken by the space charge region. Therefore, it can be predicted that the rate of hole injection from an oxidizing agent to the semiconductor VB, or the rate of electron transfer into the semiconductor CB from a reducing agent, should be independent of the applied potential. On the other hand, if the charges are from the semiconductor side, then the transfer rate is determined by the potential applied. Assuming that the concentration of holes is given by Boltzmann statistics, the total valence band current can be written:

$$j_V = j_{V,0}[\exp(e\eta/kT) - 1] \tag{2.23}$$

where η is the overpotential and $j_{V,0}$ is the exchange current density at the equilibrium potential. Similarly, for an *n*-type semiconductor, the density of electrons in the conduction band is controlled by the applied potential and

$$j_C = j_{C,0}[\exp(e\eta/kT) - 1] \tag{2.24}$$

19

With these expressions, the current-potential behavior of both n- and p-type semiconductors can be predicted provided the effect of ionic transport in the solution can be neglected, as shown in Figure 2-11.

Although the Gerischer model can give an important insight into semiconductor electrochemistry, its predictions frequently deviate from experimental results. In this model it has been assumed that the main surface interactions are with the bulk valence- and conduction- band wave functions and that the potential drop across the Helmholtz layer should remain constant. In fact, the electronic structure is likely to be distorted at the interface. It also becomes more difficult to predict the route of charge transfer in narrower band-gap semiconductors such as GaAs and InP, since thermal broadening of the majority of redox energy levels is similar in size to the band-gap itself. This model has much difficulty in describing surface states.

2.2.2.4 Photoelectrochemistry of semiconductors

The study of photo-effects is the most important part of modern semiconductor electrochemistry because of potential application in solar energy conversion. Under light exposure, the thermal equilibrium in the semiconductor is disturbed, so that electron and hole densities are increased to above their equilibrium values and $np > n_i^2$. Accordingly, the electron and hole densities are not determined by the same Fermi level. It is useful to define quasi-Fermi levels, $E_{F,n}$ and $E_{F,p}$, for electrons and holes, respectively, as given by

$$E_{F,n} = E_C - \ln\left(\frac{N_C}{n}\right) \tag{2.25}$$

$$E_{F,p} = E_V - \ln\left(\frac{N_V}{p}\right) \tag{2.26}$$

Consider excitation of electrons and holes by light within a doped n-type semiconductor so that $\Delta n \ll n_0$ and $\Delta p \gg p_0$ (n_0 and p_0 are the electron and hole concentrations at thermal equilibrium, respectively. $\Delta n = n - n_0$ and $\Delta p = p - p_0$). Then the

20

Fermi level for electrons, $E_{F,n}$, remains unchanged with respect to the equilibrium case, whereas that of holes, $E_{F,p}$, is shifted considerable downwards. The quasi-Fermi levels play an important role in the process at the semiconductor-liquid interface, because the relative position of the quasi-Fermi level with respect to that in solution yields the thermodynamic force that drives an electrochemical reaction. Figure 2-12 shows the different positions of quasi-Fermi levels at different potentials for an n-type semiconductor electrode. For the anodic polarization conditions in dark, due to the consumption of holes at surface by the redox couple in the solutions, the Boltzmann equilibrium is not maintained, resulting in a relatively low concentration of holes in a certain depth under the semiconductor surface (Figure 2-12a). Similarly, under cathodic polarization conditions in the dark, the concentration of holes is higher in a certain depth under the semiconductor surface than that expected from Fermi-Dirac equilibrium (Figure 2-12c). Under illumination conditions, the quasi Fermi energy level of holes shifts downward and the cases shown in Figure 2-12b and d are the illumination situation in combination with the anodic and cathodic polarization respectively, resulting in a "valley" for the $E_{F,p}$.

Figure 2-13 schematically shows the situation of photo-illumination of an n-type semiconductor. The holes photogenerated in the valence band are accelerated toward the surface by the space charge region electric field and may react with one or more redox couples in the solution. At the same time the photogenerated electrons are swept into the interior of the semiconductor due to repulsion from the space charge layer.

The above background knowledge is fundamental for the field of semiconductor electrochemistry and photoelectrochemistry and is also the basis of the following critical review on GaAs corrosion and photocorrosion.

21

2.3 Comprehensive literature review of GaAs corrosion

2.3.1 Thermodynamics

Theoretically, all semiconductor electrodes in electrolytes will undergo either reductive or oxidative decomposition if a suitable potential is applied or a suitable redox couple is present in the electrolyte. The extent of the corrosion is determined by the competition between the corrosion process and reaction with a stabilizing agent (also a redox couple). If no such redox couple exists, all of the current flowing through the electrode contributes to corrosion.

2.3.1.1 Pourbaix diagram

Traditionally, a Pourbaix diagram can be utilized to determine the stability of a material and the corrosion products. A Pourbaix diagram[4] of GaAs in water made by Park and Barber [13] is shown in Figure 2-14. The major redox reactions that are responsible for the instability of GaAs are:

a) Oxidation

$$GaAs + 5H_2O \rightarrow Ga(OH)_3(s) + AsO_2^- + 7H^+ + 6e^-$$
$$E = 0.123 - 0.069pH + 0.098log[AsO_2^-]$$

(2.27)

b) Reduction

$$GaAs + 3H^+ + 3e^- \rightarrow Ga + AsH_3(g)$$
$$E = 0.115 - 0.089pH - 0.029 \log P_{AsH_3}$$

(2.28)

c) Equilibrium

$$GaAs + 2H_2O + 2H^+ \rightarrow Ga(OH)_2^+ + AsH_3(g)$$
$$pH = 2.63 - \log\left([Ga(OH)_2^+]P_{AsH_3}\right)$$

(2.29)

---
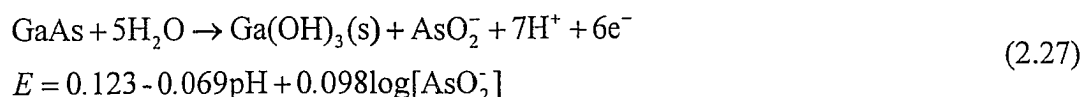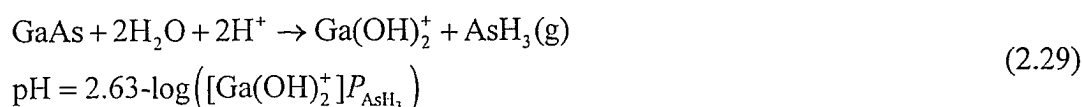
[4] Note: some obvious errors in the Pourbaix diagram from the reference have been corrected.

22

P_{AsH_3} is the partial pressure of AsH$_3$. These reactions are located in such a wide pH and potential range that only a very small region of stability is available, as shown in the diagram.

From the diagram it can be concluded, and also verified by experimental results, that the products of GaAs anodic photocorrosion depend strongly on the pH of the electrolyte. In neutral and less acidic electrolytes, insoluble oxides are formed on the GaAs surface and tend to deteriorate its photoactivity [14]. In alkaline solutions, Ga(OH)$_3$ is formed and the oxidation product of As are soluble. In concentrated acidic electrolytes (pH<2), anodic oxidation of n-GaAs leads to the formation of unoxidized elemental arsenic in the oxide and in the GaAs/oxide interfacial region [15].

Another different potential-pH diagram was produced by Li and Peter [16] (Figure 2-15). The formation of surface phases on GaAs can be inferred from Figure 2-15b, which shows the solubility of Ga(III) and As(III) species as a function of pH. While As$_2$O$_3$ is appreciably soluble over the entire pH range, Ga(OH)$_3$ is expected to form a surface film at intermediate pH values. At high pH (e.g., 13), both Ga(III) and As(III) are sufficiently soluble that surface oxide formation can be excluded. Figure 2-15a can be used to interpret that the surface stoichiometry of GaAs will tend to change outside the region of stability in such a way that a Ga-rich surface forms at very negative potentials, whereas As will accumulate at more positive potentials before As(III) dissolution becomes possible. For example, at pH = 0, GaAs can be reduced to elemental Ga at -0.75 V, however, at this potential the reduction of hydrogen ions will take place before the reduction of GaAs. In other words, the reduction decomposition of GaAs is protected by the aqueous solution. On the other hand, also at pH = 0, GaAs can be oxidized easily to As and Ga^{3+} at potential more positive than ~-0.38 V, and at pH = 7, the unstable potential starts from ~ -0.5 V, which explains the problem of anodic instability of GaAs in normal conditions and environments.

Although differences in the two available Pourbaix diagrams can be found, for example, the stable GaAs region in the diagram by Barber in Figure 2-14 is located at

high pH and low potential and within the entire pH range at sufficiently negative potentials in Figure 2-15, both diagrams are in agreement that GaAs will be unstable at positive potentials, regardless of the corrosion products. In a commonly used strong acid cleaning solution without other redox couples, with a corresponding Fermi energy level of the solution of about 0.0 V vs. SHE and pH close to 0, GaAs is unstable and decomposes[5].

A similar approach to check the thermodynamic stability of GaAs is to examine the typical standard potentials of the decomposition reactions, *i.e.*, decomposition potentials.

2.3.1.2 Decomposition potentials

Gerischer [17], Bard and Wrighton [18], and also Park and Barber [13] have discussed the thermodynamics of decomposition reactions of semiconductors based on decomposition potentials. According to them, when the standard potential for cathodic dissolution of the electrode material (cathodic decomposition potential, $_nE_{decomp}$) is located above the conduction band edge, *i.e.*, the standard potential is more negative than the conduction band edge, then the electrode should be stable cathodically. On the other hand, the electrode is anodically stable if the anodic dissolution standard potential (anodic decomposition potential, $_pE_{decomp}$) is located below the valence band edge of the electrode, *i.e.*, the equilibrium potential is more positive than the valence band edge. If the standard potential of the decomposition reaction of the electrode resides between the conduction band edge and valence band edge, the electrode is considered to be unstable and corrosion can occur (Figure 2-16). Therefore, the semiconductor in Figure 2-16a is both anodically and cathodically stable and Figure 2-16b shows the situation where the semiconductor is both anodically and cathodically unstable. The semiconductor in Figure 2-16c is anodically stable and cathodically unstable; while the one in Figure 2-16d is

---

[5] The Pourbaix diagram in Figure 2-15 is likely more reliable than the one in Figure 2-14. From the experimental results presented here, GaAs can be cathodically protection, that is, at relatively negative potentials, GaAs can be stabilized even in strong acidic solutions. In addition, the original diagram in Figure 2-14 from the literature contains some minor errors which have been corrected.

24

cathodically stable and anodically unstable. Figure 2-17 shows the positions of band edges and decomposition energy levels for GaAs. Both the anodic and cathodic decomposition potentials are inside the band gap, suggesting that both anodic and cathodic decomposition may occur following the reactions shown in Figure 2-17 for neutral solutions. Here the potential for NHE = -4.50 V is adopted. Other decomposition potential graphs can also be obtained at different pH values, which will conform to the Pourbaix diagram.

2.3.2 Flatband potential measurements

Flatband potentials for GaAs, both n- and p-type, have been determined by capacitance methods from linear Mott-Schottky curves in several papers [16, 19-26]. These direct measurements using the Mott-Schottky equation are based on the assumption that the equivalent circuit across the interface is only a capacitor for the space charge region in series with a resistor for the electrolyte solution. The imaginary part of the Mott-Schottky measurements is $\dfrac{1}{2\pi f C_{sc}}$, where f is the frequency applied in the experiment and C is the capacitance of the space charge layer. The limitation of using this circuit to determine the flatband potential was discussed by Cardon $et\ al$ [22].

The values obtained have seldom been used to discuss the band bending nor have they been related to current-potential behavior. In the above publications, the Mott-Schottky curves at different frequencies could be regressed to a common intercept at the potential axis, which means that the flatband potential does not depend much on frequency. LaFlere $et\ al.$ [27, 28] have carried out much of the work on flatband potentials for GaAs electrodes. They investigated the frequency dependence of the impedance for n- and p-type GaAs surfaces and compared the Schottky junction formed with Au and the junction formed in contact with an electrolyte. p-GaAs had a larger frequency-dependence than n-GaAs, which could be explained by the relative stability of n-GaAs in solution. They concluded that on well-etched GaAs crystals the residual

25

frequency dependence was due to dielectric relaxation phenomena, caused by polar double layer constituents, which can be characterized by a complex dielectric constant if the layer is homogeneous. This means the simple circuit of a solution resistor and space charge region capacitor is not enough to describe the interface.

Table 2-2 shows the flatband potentials summarized by Frese [29], in which most of the values were measured by LaFlere (see references in [29]). For samples with doping levels from 10^{16} to 10^{17} cm^{-3}, if no surface states exist, the difference between the Fermi energy level and the band edge in bulk can be considered to be the same. From Table 2-2, flatband potentials determined from Mott-Schottky measurements shift to more negative potentials with increasing solution pH for both n- and p-GaAs. This indicates the moving of band edges for samples with different pH, shown by the E_C^S and E_V^S values, the conduction band and valence band energies, respectively.

The flatband potential for n-GaAs in strong acidic solutions without other redox couples is acknowledged to be $\sim$-1.0 V, while in alkaline solutions, flatband potentials of -1.5 V vs. SCE or even more negative values have been obtained [30]. These results have been explained as being due to the interaction of GaAs with H_2O [1], as in the case of germanium/electrolyte systems. Confirmation was obtained by Abshere and Richmond [20] in their study, in which water additions to an n-GaAs (100)/methanol photoelectrochemical cell, protected by redox couples in solution, led the cell back to a state conducive to corrosion, finally pinning the Fermi energy level. It is recognized that the interaction of water with GaAs results in an adsorption layer (OH or H) at the surface, which can explain the different flatband potentials in forward and backward scanning measurements. Early study of pH and redox potential dependence of the flatband potential for n-GaAs in methanol by Ba et $al.$ [21] indicated that without a redox couple added in the solution, the flatband potential shifted -72 mV per pH unit for the (100) face and by -100 mV per pH unit for the (110) face. If a redox couple was present, the flatband potential would be independent of pH, virtually pinned by the Fermi energy level of the redox couple, which could be useful for correction of the band edge position at the interface of n-GaAs.

26

It has been recommended that flatband potential measurements for n-GaAs be performed at a very fast scan rate [1, 31]. The potential partition across the interface with the adsorption layer must be divided into three parts: space charge layer, double layer and adsorption layer. With the components of the adsorption layer changing, the potential drop in the space charge region would not behave the same as the case without adsorption. For example, the potential drop in an As-H layer would be different from an As-OH layer. Good linear Mott-Schottky curves at fast scan rates suggest that a change in dipole potential or adsorption species from H to OH, or vice versa, requires a certain amount of time.

Recently, Erne *et al.* [32] used electromodulated infrared spectroscopy to investigate the electrolyte interface of a polished n-GaAs single crystal under conditions where the semiconductor space-charge layer is depleted. This technique is based on the absorption of infrared light by free charge carriers. Although the infrared signal was weak, equivalent results with the Mott-Schottky measurements were obtained. This technique might be more useful than direct Mott-Schottky tests because it can also be used for the characterization of free charge carrier concentrations under other space charge layer conditions.

Flatband potentials under illumination were found to be somewhat more negative than the values obtained in darkness. This was explained by Li [16] and Allongue [33, 34] as being related to the positive charge of dissolution intermediates.

Flatband potential of GaAs-metal and GaAs-electrolyte contacts measured by the Mott-Schottky relationship were found to deviate from a linear dependence under forward bias by Laflere *et al.* [28]. The hysteresis was explained by the forward current. In other words, the capacitance obtained from Mott-Schottky measurements should be corrected, *i.e.*, the simplest equivalent circuit of R and C in series is not enough to describe the contacts and correction is needed. Further discussion can be found by

Cardon *et al.* [22] who indicated that many factors limit the accuracy of using RC in series to measure the interface capacitance.

2.3.3 Voltammetric experiments

Normal electrochemical methods based on the relationship of current density vs. the applied potential (CV) are the basis of all corrosion studies. CV behavior of materials can offer information on both the thermodynamic and kinetics / mechanisms of corrosion processes.

2.3.3.1 CV results in indifferent electrolytes

Holes vs. electrons

Indifferent electrolytes refer to aqueous solutions containing no active metal ions, with high ionic strength, *e.g.*, 0.5 M H_2SO_4, 28.5% H_3PO_4, 0.1 M KOH, etc. The current-potential characteristics of n- and p-GaAs electrodes in strong acid solutions from the literature are shown in Figure 2-18 [1, 35]. Here the cathodic process corresponds to the reduction of protons, *i.e.*, the H_2 evolution reaction (HER), whereas in the anodic range, the electrode is dissolved. Oxygen evolution is not observed here because it takes place only at stable oxide electrodes. It is interesting to see that the current-potential curves for n- and p-GaAs electrodes look very different. For instance, the cathodic current, due to the formation of H_2, rises steeply with increasing cathodic potential at the n-GaAs electrode whereas a very small current occurs at the p-GaAs electrode. This result is a clear indication that the electrons required for the reduction of protons are transferred from the conduction band to the protons. This conclusion is supported by the result that the cathodic current at the p-GaAs electrode is enhanced by light excitation. In the latter case, electrons are excited from the valence band into the conduction band from where the electrons are transferred to the protons.

28

The same type of argument shows that the anodic decomposition reaction occurs via the valence band. Here, it is clear that the corresponding anodic current at p-GaAs increases steeply with increasing anodic polarization, whereas a very small anodic current is found with n-type electrodes. The latter could also be increased by light excitation. Accordingly, holes from the valence band are required for the anodic decomposition of the semiconductor.

Altered Tafel plot

Altered Tafel plot measurements of GaAs and InP corrosion behavior with model simulations have been discussed by Allongue and Blonkowski [33, 34, 36]. The altered Tafel plot on semiconductor electrodes was defined as the measurement of the current as a function of the change of flat band potential $\Delta V_{fb}=V_{fb}^*-V_{fb}$ (V_{fb}^* is the flatband potential measured at altered conditions). As pointed out by the authors, using such Tafel plots to study the semiconductor corrosion has twofold significance. Firstly, correlations between ΔV_{fb} and the interfacial mechanism are expected since ΔV_{fb} is a close function of kinetics and transfer mechanisms. Secondly, such a Tafel plot is related to transfer processes only since a valid flatband potential can just be obtained for a large depletion region. Some interesting results are as follows: (i) Increasing the doping density reduced the shift ΔV_{fb} for a given current; (ii) n- and p-type GaAs gave the same Tafel plots; and (iii) increasing the doping concentration increased the corrosion kinetics of GaAs because the Tafel plot became steeper for the highly doped sample. The authors also found that Tafel plots were sensitive to the pH of the solution, the type of conductivity (n or p), the origin of holes and the semiconductor itself. The authors suggested that on p-GaAs the global corrosion current was proportional to the hole concentration at the surface ($p_S = N_A \exp(-e\phi_b / kT)$) in concentrated acid solutions, because the slope of Tafel plot was close to 60 mV/decade. However, in alkaline solutions, the Tafel plot slope was unusually small (ca. -30 mV/decade), suggesting that the corrosion current is practically proportional to p_s^2.

Surface recombination

The recombination process is another characteristic of semiconductor CV behavior. Under illumination, external minority charge carriers are generated and accumulate at the

29

surface, changing the surface voltage, Fermi energy level, band bending, etc. In Figure 2-18 the region between open circuit potential and the current plateau is the potential range where recombination can be distinguished. External minority charge carriers, that are photogenerated are consumed by the two competing processes: recombination and electrode dissolution or capture by a redox couple in solution. An intensity modulated photocurrent spectroscopy (IMPS) of n-GaAs / alkaline solution study [16] gave information about surface recombination, not recombination in the space charge region. The surface was found to be heterogeneous on a sufficiently coarse scale to produce two or more relaxation time constants at low values of band bending. With S^{2-} or Se^{2-} ions in solution, the theoretical model of surface intermediates involving surface recombination was verified. Modern photoluminescence (PL) techniques [37-43] have been applied to investigate the recombination process, also showing surface recombination by surface midgap states, not recombination in the space charge region. The lifetime of the minority charge carriers within the trap states is of the order of microseconds, much longer than that inside the semiconductor bulk (on the nanosecond scale).

The above voltammetric behavior of GaAs was studied in indifferent solutions, *i.e.*, H_2SO_4 or KOH solutions. Considerable work has also concentrated on the corrosion behavior in solutions containing redox couples to study the charge transfer and kinetic mechanisms between semiconductor / electrolyte interfaces.

2.3.3.2 CV behavior with redox couple in solution

Some of the CV work by Frese and Morrison [15, 29, 44-46], Miller [47, 48], Allongue [49, 50], Miller and Menezes [51] and Vanmaekelbergh and Gomes [52-55] was on the stabilization of GaAs with redox couples in solutions. Other work mainly focused on the charge transfer [12, 31, 47, 56-62].

Stabilization experiments

Stabilization work on GaAs with many stabilizing agents has been tried, for instance, $Fe^{II}(EDTA)$ [15, 45-47], $Fe(SCN)_6^{4-}$ [51]and Se^{2-} [49] and S^{2-} [48]. Single current-potential curves are not sufficient to characterize the oxidation process since,

although oxidizing agents may inject a substantial number of holes into the valence band, the holes that lead to surface oxidation and dissolution will not contribute to the net current measured. Instead, the rate of oxidation of the redox couple at the surface must be measured independently to obtain the total rate of hole injection. This was accomplished using rotated ring-disk electrode (RRDE) experiments. A stabilization coefficient was defined as the ratio of the current for oxidation of the stabilizing agent, which can be obtained from the ring current, over the total current measured on the disk electrode. The series for GaAs/Fe^{II}(EDTA) showed that for a well-etched surface of GaAs, the stabilization coefficient can exceed 99%. It was also demonstrated that a more damaged surface had a lower stabilization effect. The remaining current was considered to lead to corrosion. The stabilization coefficient for Se^{2-} in KOH solution was found to be close to 100% [49] and the electrodes after Ru (ruthenium) treatment gave results confirming that reaction intermediates were responsible for the band shift during potential scans.

GaAs / redox couple electrochemical system

Two GaAs / redox couple electrochemical systems have been widely investigated in the literature. One is the GaAs / H$_2$O$_2$ system [63-66] and another is the GaAs / Co(II) system [58, 67, 68]. The former was of interest because of two aspects: frequent use of H$_2$O$_2$ as an etchant for surface preparation, and cathodic oscillation during the reduction of H$_2$O$_2$ due to the formation of an active arsenic hydride phase (As$_2$H$_2$). The GaAs / Co(II) system, especially cobaltocene (Co(Cp)$_2$$^{0/+}$), is attractive because of its promising use in solar cells.

Quasi Fermi level concept

Although the quasi Fermi level [1, 35, 56, 57] has been accepted by many scientists, it is seldom applied to the phenomena on III-V semiconductors. The group of Memming has attempted to use it to compare reactions at *n*- and *p*-type electrodes of the same material, *e.g.*, GaAs, to study the charge transfer which is directly relevant to the Fermi energy levels. Cu$^+$/Cu^{2+} couples were taken as an example. The current-potential characteristic at *n*-GaAs can be predicted from experimentally measured results on *p*-GaAs by distinguishing the different parts of the current from/to the CB and VB. This

31

would be useful because the majority charge carriers' behavior in a semiconductor is not light sensitive and can be easily studied, that is, no quasi-Fermi level is required for analysis. Based on the assumption that if the same quasi-Fermi levels exist at n- and p-type electrodes, the same current-potential behavior and charge-transfer mechanism are expected and it might be possible to estimate the quasi-Fermi level of minority charge carriers.

2.3.3.3   CV behavior in organic electrolyte or mixtures

Promising GaAs-based photoelectrochemical cells were studied in non-aqueous electrolytes or mixtures [20, 68-70] because of the interaction of GaAs with water.

Results of n-GaAs in CH_3CN [69] showed partial Fermi level pinning over a wide range of redox potentials. A change of over 1.2 V in redox potential of the solution resulted in only a change of 300 mV in the open-circuit potential. Flatband potentials from Mott-Schottky measurements yielded a barrier height change of less than 300 mV. Kinetic studies showed that surface-state recombination is the dominant recombination mechanism at these interfaces. Partial Fermi level pinning complicated the mechanism and kinetic law extraction.

A combination of picosecond photoluminescence and electrochemical studies of the n-GaAs/methanol interface was presented by Abshere et al [20, 37]. The electrochemistry occurring at the interface was found to have a strong influence on the observed photoluminescence decay curve vs. voltage. It was found that the redox couple (Fe complexes) gave some protection from corrosion for GaAs. Addition of water could give more protection because of Fermi level pinning of the GaAs.

The investigation of oxide growth of both $n+$ (highly n doped) and $p+$ (highly p doped) GaAs in a mixture of ethylene glycol, water and tartaric acid was performed by Buda et al [70]. The applied pulsed current conditions produced a much more uniform oxide (as imaged in the scanning electron microscope) than the constant voltage and

32

constant current conditions. A 100nm thick oxide layer could be grown in only 4.6 minutes at 12 mAcm^{-2} pulsed current density (900 μs current pulse width and 10 ms interval). A 260 nm thick layer was obtained for a final voltage of 135 V at 4.3 mAcm^{-2} pulsed current density.

Besides the above research work, the reduction of protons [23, 24] and oxygen [71-74] on GaAs were also considered. The study of H adsorption from the reduction of H$^+$ is very important as the adsorption of H and OH onto GaAs influences the surface band bending and contributes to the potential distribution in most aqueous solutions. Similar to the work on germanium [19], the adsorbed composition of water at the surface changes from H to OH, from cathodic to anodic potential regions, shifting the band edge and flatband potential. The reduction of oxygen on p-GaP and p-GaAs [73, 74] showed that the current doubling can only be explained by the existence of surface states.

2.3.3.4 Impedance spectra

Impedance techniques are especially useful for probing the mechanism (charge transfer pathways) and interface potential distribution. The existence of a space charge region makes the impedance spectra more complicated than for metal electrodes. Under illumination conditions, photoimpedance or photocapacitance [50, 75] can also be performed to investigate surface states. Other possible useful opto-electric impedance techniques, including photocurrent and photovoltage response to modulated illumination have been discussed by Chazalviel [76]. Efforts have also been made to address the electrochemical impedance, both theoretically and experimentally, of charge transfer across the interface through surface states at semiconductor / redox couples, including GaAs [77].

The earliest impedance explanation of semiconductor electrodes was made by Memming [78], almost 40 years ago. It was pointed out that the intricate equivalent circuit for semiconductor electrodes might be reduced and simplified at some extreme

33

conditions. For instance, at high frequencies, a simple RC circuit might be sufficient to describe the interface and n-type germanium was taken as an example.

Investigation of the kinetics of the Cu^+/Cu^{2+} redox system at p-GaAs electrodes has been done using impedance spectroscopy by Uhlendorf et al [59]. The reactions, both anodic and cathodic, were diffusion-controlled processes via the valence band, competing with anodic GaAs decomposition. A second-order rate constant was determined to be 5×10^{-19} cm^{4}s^{-1}.

The frequency dependence of the space charge region capacitance C_{SC} of n- and p-GaAs was carried out by Laflere [27]. In his work, only Mott-Schottky measurements using the simple RC circuit were performed. However, frequency dispersion was found in the Mott-Schottky plot, for example, a non-linear region at negative potentials for n-GaAs and at positive potentials for p-GaAs. The phenomenon of frequency dispersion was shown to be more obvious for p-GaAs, and was significantly affected by the surface pretreatment. The possibility of determining the flat-band potential from frequency-dependent impedance was discussed.

Electrochemical photocapacitance spectroscopy by Allongue and Cachet [50] indicated that three surface states might exist, located around E_C-1.05 eV, E_C-1.15 eV and E_C-1.32 eV for the n-GaAs / 7M NaI (pH=0) system and the state were partially emptied by subgap illumination. These surface states were related to the corrosion intermediates of GaAs. Allongue and Cachet also performed steady state photocapacitance on the n-GaAs / 1M KOH system [75]. The state of E_C-0.85 eV was related to the large response of a deep electronic level (EL2) and the states at E_C-0.98 eV and E_C-1.30 eV were surface related.

The impedance analysis of the GaAs / electrolyte system was also discussed by Nemcsics [79]. It was found that the series resistance (R_S), including the bulk semiconductor resistance and the solution resistance, was related to the surface roughness. The rougher the surface, the smaller the series resistance.

In recent years a series of impedance work was done by Hens and Gomes on InP and GaAs. Theoretical discussion on the diffusion impedance [80] at semiconductor electrodes made the point that distinction between direct capture reactions and direct injection reactions could be distinguished from the impedance spectroscopy. The former was a Randles-like equivalent circuit and the latter would have a Warburg impedance if the reverse reaction was negligible. In the case of hole-injection reduction of Ce^{4+} on n-GaAs, no Warburg impedance was detectable because the hole injection rate was anodically and cathodically diffusion-limited and the dependence of the rate on the applied potential was negligible. For the InP / $Fe(CN)_6^{3-}$ system, only the cathodic hole injection rate was diffusion-limited and thus a Warburg impedance was detected, with a slope at a non-ideal value of 0.86. In other words, if the mass transport process is not coupling with the electrode potential, no diffusion process can be detected in the impedance. The results from the impedance on the n-GaAs / Fe^{3+} system [77] indicated that the charge transfer is more likely to be surface states mediated in both directions. The reduction of Fe^{3+} was also found to be strongly dependent on the surface pretreatment. Furthermore, the density of surface states increased with time, as suggested from the increasing reduction current for Fe^{3+}. Impedance comparison on InP and GaAs in indifferent electrolytes was studied to revisit the frequency dispersion phenomenon [81, 82]. The equivalent circuit of a perfect capacitor, in combination with a constant phase element, was used to model the space charge region. The frequency dependence of the interfacial capacitance was related to the electrolyte conductivity and electrode surface pretreatment. The origin of the dispersive element was attributed to the localized states at the semiconductor surface, interacting with the electrolyte. A detailed EIS study of photocorrosion of n-InP anodes [83] showed no recombination impedance, but an inductive loop. The former was explained by the assumption that recombination occurs by a rapidly oxidizing decomposition dissolution process and the inductive loop was proposed to be due to a slow oxidation step of either the fourth or the fifth decomposition intermediate.

35

2.3.3.5 Surface techniques

Surface techniques applied to the study of GaAs include scanning electron microscopy (SEM) [84, 85], energy dispersive X-ray analysis (EDX) [85], scanning tunneling microscopy (STM) [86-88], atomic force microscopy (AFM) [89], X-ray photoelectron spectroscopy (XPS) [90-96], X-ray diffraction (XRD) [84, 97-99], infrared spectroscopy (IR) [19, 23, 24, 32, 65, 100, 101], Raman spectroscopy [102, 103], electroreflectance (ER) [26, 66], photoluminescence (PL) [37-43], Auger electron spectroscopy (AES) [84, 104] and ellipsometry [24, 65, 84, 105].

STM studies are concerned with surface reconstruction, *e.g.*, (2×4) unit cells, and will not be reviewed.

Various surface composition identification techniques, *e.g.*, EDX and XPS, have indicated that there is an As-enriched surface after corrosion on both *n*- and *p*-GaAs in strong acidic solutions, as confirmed by the comparison of CV behavior between corroded electrodes and As-coated electrodes [14]. However, the electroless dissolution of *p*-GaAs, in aerated boric acid solutions at pH=4.6, formed Ga_2O_3 oxide at the electrode surface and the oxidation rate was promoted by Co(II) ions [67]. In high pH (pH>9), gallium enrichment was detected in the oxide formed.

A series of studies on oxide formation at high positive potentials (>4 V, up to 10V) was performed by the group of Lockwood, Schmuki and Bohn [39, 102, 106-114]. Surfaces were characterized by Raman spectroscopy, XPS and PL. A porous GaAs surface was found with deposition of microcrystallites (Ga_2O_3 and As_2O_3).

In summarizing the results of surface characterization by PL, IR and ellipsometry, GaAs was found to be oxidized even at OCP, in contrast to Si and Ge. The surface of GaAs was adsorbed with H or OH, depending on the potentials applied. The PL decay results showed clearly that the recombination process is via surface states.

36

2.3.4 Mechanisms

The mechanism for GaAs decomposition / corrosion is quite complicated since six elemental charge carriers and hence six consecutive electrochemical steps are involved in this anodic process [17, 115]. A several step oxidation process is very common for the decomposition of III-V semiconductors, e.g., GaP and InP. From the investigation of several stabilization reducing agents for GaAs and GaP, it was found that the decomposition mechanism depends on the composition of the electrolyte. Work from the group of Vanmaekelbergh and Gomes pointed out that the common point of the various mechanisms was that the oxidation of the reducing agents in the electrolyte occurred not by the holes directly, but from intermediates at the surface. Modeling of the stabilization coefficients, with the relationship of concentration of the reducing agents, was discussed by these authors [53] and a comprehensive model was proposed to explain the mechanism of III-V anodic decomposition [116]. Since the available experimental results could only provide information on one chemical reaction in the early stages of the decomposition process [52], only the first chemical reaction was discussed in the model.

Before presenting the detailed mechanisms in the literature, it should be noted that the common feature of all these mechanisms is the first electrochemical step. A valence band hole is trapped in a surface bond (denoted as X_0)[6], leading to a one-electron bond X_1^+, representing a positively charged surface intermediate that is mobile in a two-dimensional surface layer:

$$X_0 + h^+ \rightarrow X_1^+ \tag{2.30}$$

Since Ga is the less electronegative atom in GaAs, the positive charge was suggested to be mainly located on the Ga, so that chemically, X_1^+ was assumed to be Ga^+. Another step widely accepted is the chemical reaction of X_1^+ with water to produce X_1-OH because the final corrosion product contains OH, such as $Ga(OH)_3$, H_3AsO_3, etc.

---

[6] The notation of Vanmaekelbergh is used here for convenient description.

37

$$X_1^+ + nH_2O \rightarrow X_1-OH + H^+(H_2O)_{n-1} \tag{2.31}$$

Based on steps (2.30) and (2.31), possible pathways for continued reactions can be all listed (Figure 2-19). As mentioned before, Vanmaekelbergh and Gomes found in their stabilization experiments that surface intermediates, not holes, oxidized the reducing agent in the solution and thus the so-called X mechanism or X-C mechanism was determined for GaAs corrosion, instead of the H mechanism or H-C mechanism occurring on GaP. The X-C mechanism refers to the combined steps of 1, 2, 4 and 5 and the X mechanism is the combination of steps 1, 2 and 4 in Figure 2-19. Combination of steps 1, 2, and 3 is called the H mechanism and if step 6 is also included it is the H-C mechanism since the oxidants for continuing steps are holes, not the intermediates.

The comprehensive model proposed by Vanmaekelbergh and Gomes [116] was based on the assumption that the concentration of unbroken surface bonds X_0 is much higher than that of the decomposition intermediates X_1^+, X_1-OH, etc. Hence, the probability for a hole to be trapped in an unbroken surface bond will be much higher than for a reaction with a decomposition intermediate, even if the respective rate constants are the same. This assumption excludes the possibility of a H mechanism and the H-C mechanism occurs only if the concentration of mobile surface intermediates is reduced to a very small value as a result of chemical reaction in Eq. (2.31). Note, that intermediate X_1^+ is considered to be mobile on the surface, but X_1-OH is not. This model can explain the effect of the medium (solution contents) by using organic or mixed electrolytes in which the H(-C) mechanism was observed at low concentrations of water or OH⁻ eliminates the possible path of X_1-OH being an alternative intermediate.

From their flatband shift experiments on the altered Tafel plot, Allongue and Blonkowski [33, 34, 36] argued that if continuing oxidation was by the intermediate X_1^+ and reaction (2.30) is irreversible, then a simple calculation would infer that the corrosion current density would be proportional to $[X_1^+]^2$ and their altered Tafel slope would be independent of solution pH, in contradiction to their results. Their simulation showed that reactions involving free holes only were enough to account for the stabilization

38

experiment results. Therefore, the reaction scheme of GaAs corrosion accepted by Allongue and Blonkowski is the combined steps of 1, 2 and 6 and can be written as follows:

$$X_0 + h^+ \leftrightarrow X_1^+ \tag{2.32}$$

$$X_1^+ + nH_2O \rightarrow X_1 - OH + H^+(H_2O)_{n-1} \tag{2.33}$$

$$X_1 - OH + h^+ \rightarrow \text{corrosion product} \tag{2.34}$$

It should be noted that reaction (2.32) is reversible, unlike irreversible reaction (2.30). Furthermore, two corrosion states of GaAs (E_C-0.98 eV and E_C-1.15 eV, where E_C is the conduction band edge potential) were observed by their photocapacitance spectroscopy measurements [75]. These were associated with As sites and Ga sites, respectively and this could explain well the different corrosion behavior between GaAs and InP due to the relative energy levels of corrosion states and the VB.

2.3.5 Etching

Etching of GaAs can be categorized by physical and chemical approaches and (photo)electrochemical etching. Chemical etching is mainly for the purpose of surface cleaning [63, 95, 117-120]. Solutions generally used contain hydrogen peroxide or strong acids, e.g., HCl, H_3PO_4, HF or Br_2 [95].

(Photo)electrochemical etching work was mainly studied by the group of Kelly [118, 119, 121, 122]. Photoelectrochemical etching is of special interest, because the semiconductor material can be locally etched away by focusing a light beam on a certain spot (or by using a laser beam). When the photon energy, is above the band gap value (for GaAs infrared light is suitable), light is absorbed at the surface of a semiconductor, and electron-hole pairs are created. The built-in electric field in the semiconductor can transport these carriers either to or away from the interface between the semiconductor

39

and the electrolyte. For example, for n-type GaAs, the electric field typically drives holes to the interface and electrons to the bulk. There are two possible etching mechanisms: electrochemical oxidation with an external voltage source ("anodic etching") and electrochemical etching with an oxidizing agent ($e.g.$, H_2O_2) but no external voltage source ("electroless etching").

Electroless photoelectrochemical etching (laser-controlled micrometer-scale) was demonstrated by Ruberto et $al.$ [123] using $HNO_3:H_2O$ solution (1:20) for GaAs, and $HF:H_2O$ (1:10) for InP. UV illumination was found to photoelectrochemically etch not only n-type, but also p-type GaAs and InP within the small illumination zone. This was explained by the shallow absorption depth of the UV light.

With a scanning electrochemical microscope (SECM), high resolution etching of GaAs using the feedback mode has been achieved by Mandler and Bard [124]. Strong oxidants, such as Br_2, could be electrogenerated in situ at an ultramicroelectrode (UME) and used as etchants. The current flowing at the UME was also used to monitor the distance between the UME and the substrate surface.

Ma et $al.$ [125] studied the sample size effect in photoelectrochemical etching of n-GaAs. It was shown that the etching rate increased significantly with the ratio of sample size to X-ray illuminated area, which could be explained by the rate-limiting effect on the charge transfer across the semiconductor / electrolyte junction. It was also found that the etching rate was related to the non-illuminated area by a rather simple function.

2.3.6 Protection and surface modification

Protection of GaAs against corrosion was investigated mainly by surface modification, coating of adsorbates, $e.g.$, Se^{2-} [49] and S^{2-} [48, 126, 127] ions and self-assembled monolayers (SAM) of thiols [90, 125, 128-133]. The ions used were

40

specifically adsorbed onto GaAs and induced a high density of surface states, pinning the Fermi energy level. SAM of thiols acted under the same mechanism as for metals by adjusting the work function of GaAs. The difficulty in maintaining a long lifetime for the adsorbed film is due to easy oxidation of the GaAs surface. If the surface is not perfectly covered by adsorbates, oxide formation will occur and degrade the protective film.

2.4 Proposed objectives

Despite the numerous studies of GaAs systems, several main problems still remain:

(1) Band bending: This is the most important factor in characterizing the semiconductor, determining the surface concentrations of the charge carriers and thus the charge transfer rate across the interface. To obtain the true band bending is still a work in progress.

(2) Flatband potential: Although flatband determination from the Mott-Schottky equation is widely accepted, it is not that useful in reality due to complex surface states. To determine the appropriate potential range in which band bending can be found using flatband potential as reference is necessary.

(3) Mechanism: The two mechanisms presented in the above review need to be clarified.

(4) Doping levels: Corrosion of GaAs is expected to be dependent on the doping levels, especially the hole concentration because corrosion of GaAs is a valence band process.

(5) Breakdown mechanism: The breakdown of GaAs is found to occur earlier than expected. For Schottky contacts with gold (Au), different breakdown mechanisms are defined. However, these should be reconsidered for the less than perfect Schottky barrier of GaAs / electrolyte contacts.

41

This thesis mainly aims to address the above listed problems.

Table 2-1 Classification of materials by electrical resistivity.

Materials	Electrical Resistivity ρ
Conductors	< 1 mΩcm
Semiconductors	1 mΩcm ~ 10 MΩcm
Insulators	> 10 mΩcm
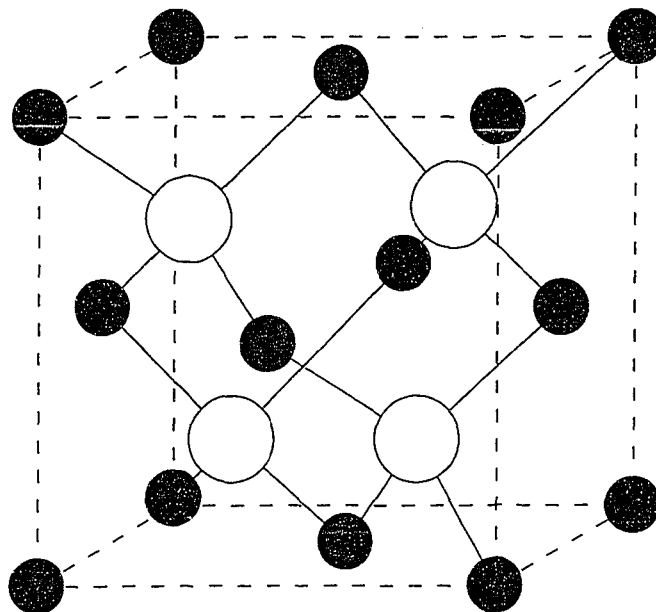
Figure 2-1 Crystal unit structure (zinc blende) of GaAs: two FCC sublattices offset ¼ of the cube diagonal. Solid circles represent Ga, while open circles represent As. The lattice constant is 0.565 nm.

43
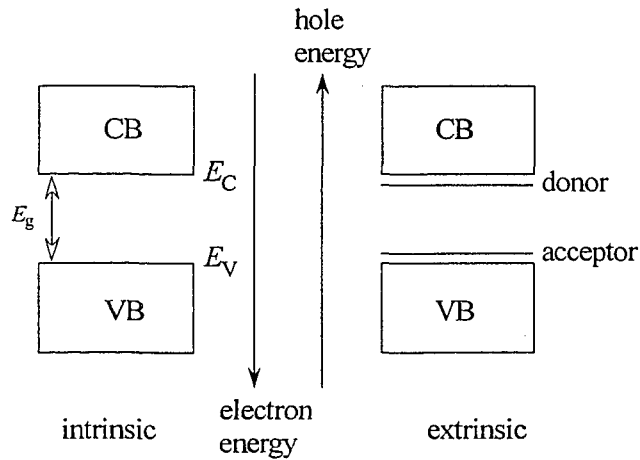
Figure 2-2 Illustration of intrinsic and extrinsic semiconductors. E_c is the energy at the CB edge, and E_v the energy at the VB edge. As shown, if the impurity energy level is close to the CB, electrons at that energy level can be easily excited to CB and the dopant is a donor. If the impurity energy level is close to the VB, electrons in VB can be easily excited from valence band to the energy level and the dopant is an acceptor.

(a)   (b)
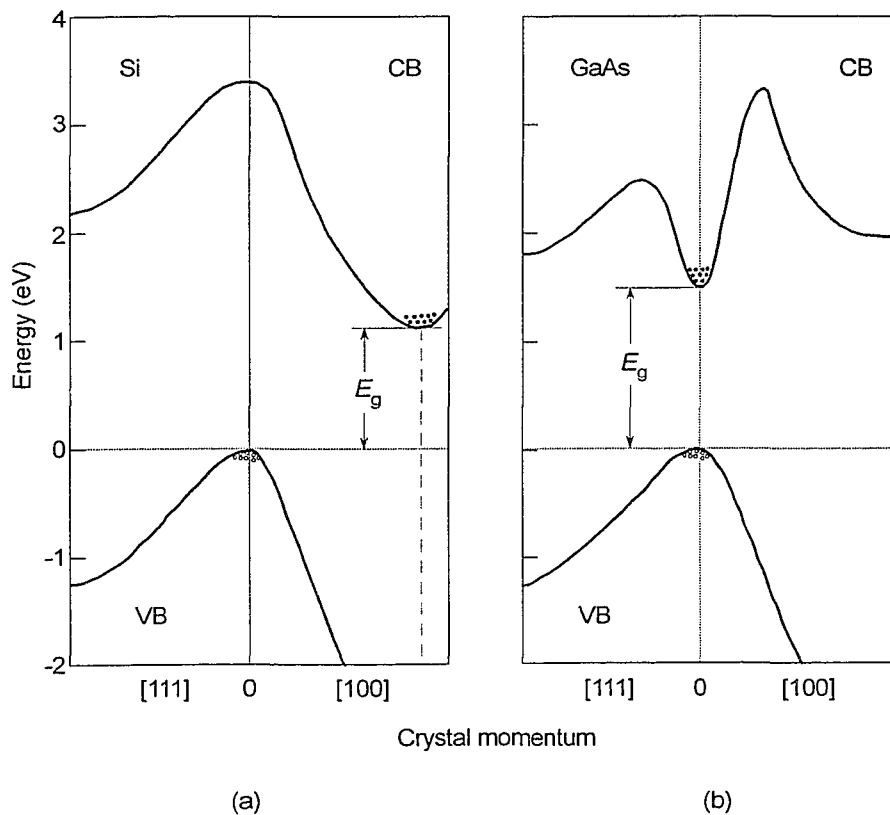
Figure 2-3 Comparison of energy band structure for Si and GaAs [1]: (a) Si, indirect band gap; (b) GaAs, direct band gap. Note the curvature of the bottom of the CB. Solid dots: electrons; open dots: holes.

44
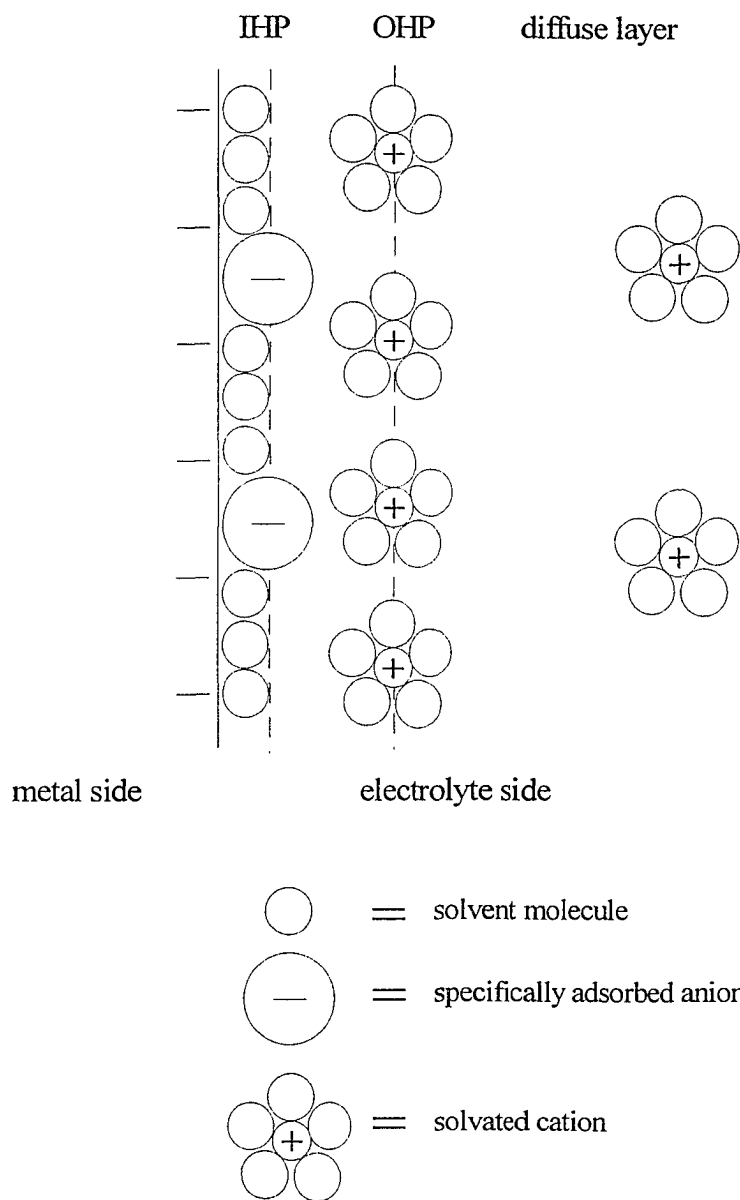
Figure 2-4 A typical diagram of the double-layer structure. From reference [3].

45
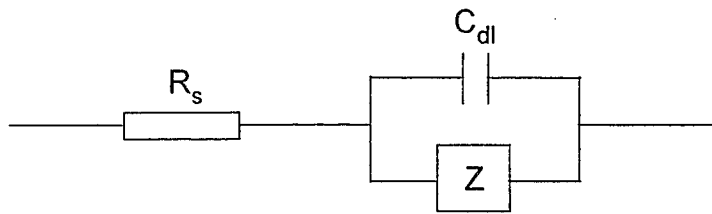
Figure 2-5 Equivalent circuit for a metal/electrolyte interface with electrochemical reactions. C_{dl} is the double layer capacitor. R_S is the solution resistance. The symbol of Z in the box represents other impedances. These may include other source impedances besides the electrochemical reaction part, *e.g.*, a virtual capacitor due to chemical adsorption.
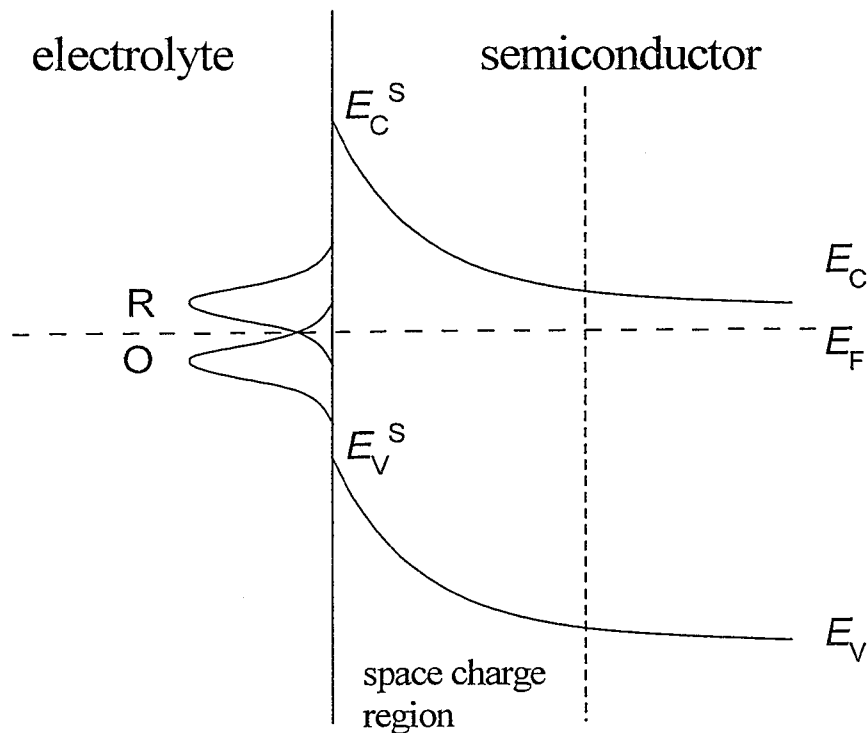
Figure 2-6 Band bending in *n*-type semiconductor in contact with the electrolyte solution (with redox couple O/R).

46
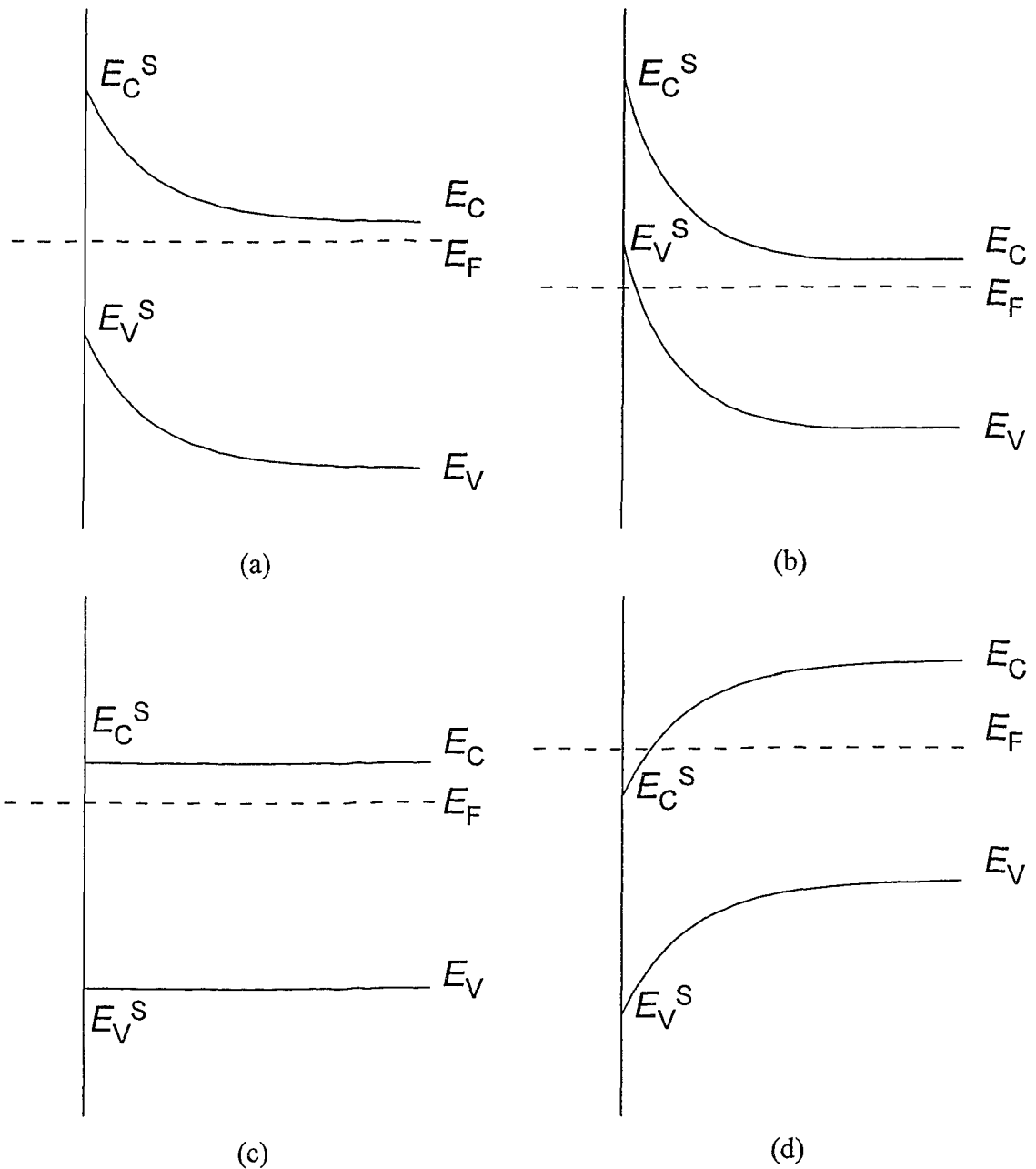
Figure 2-7 Types of space charge layers on an n-type semiconductor. (a) depletion layer (usually formed when contacting with other conductors or semiconductors); (b) inversion layer (might be induced by an adsorbate on the surface); (c) flat band situation (no contact with conductor / semiconductor or can be formed by external applied potential); (d) accumulation layer (external applied potential can make it happen).
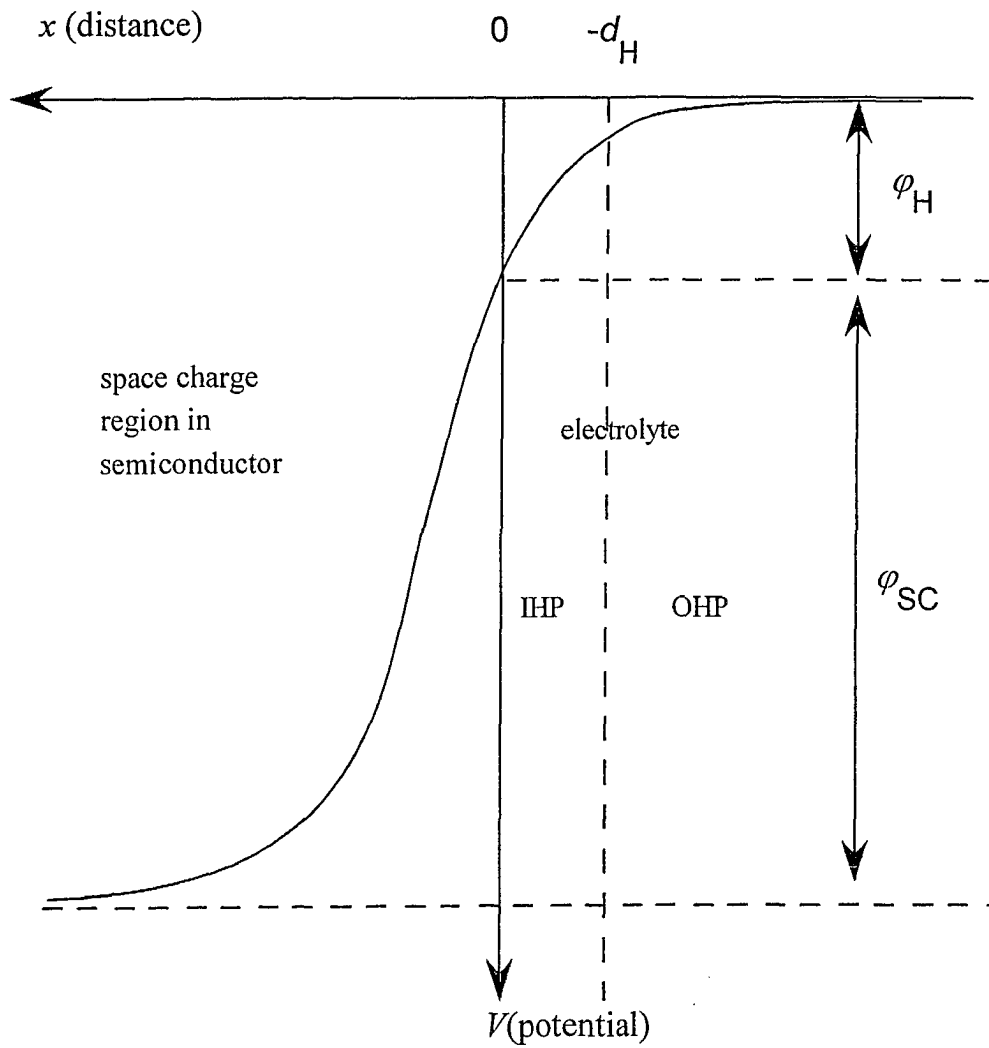
Figure 2-8 Schematic illustration of the potential distribution of a semiconductor / electrolyte interface under depletion situation. d_H is the width of the Helmholtz layer.

48
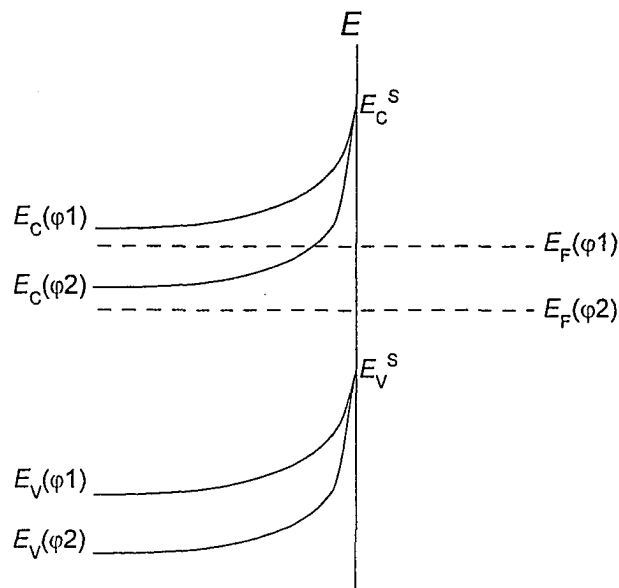
Figure 2-9 Schematic of band edge pinning of an n-type semiconductor in contact with two redox pairs of different redox potentials (Fermi energy level). The Fermi level of the semiconductor changes with the contact redox pair without moving the band edge. Therefore, in this case, there is more band bending for the contact with redox pair 2 which has a Fermi energy level of $E_F(\varphi2)$.

(a)   (b)
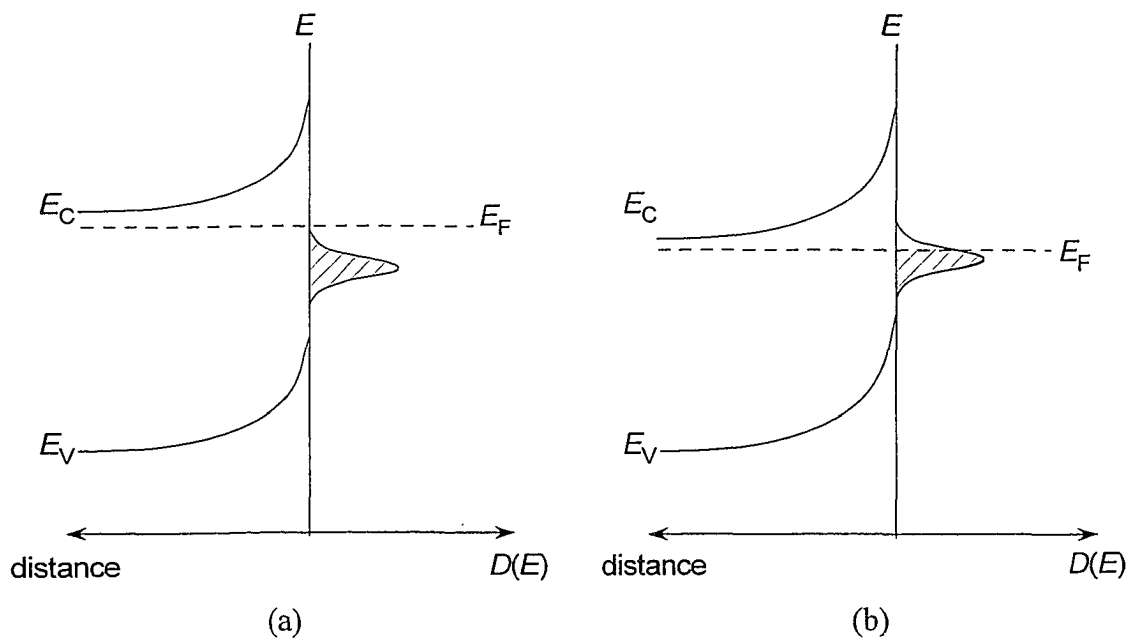
Figure 2-10 Schematic diagram to show Fermi level pinning by surface states of an n-type semiconductor. (a) for a small bias with a filled set of surface states; (b) for a larger bias in which the surface states have been partially ionized.

49
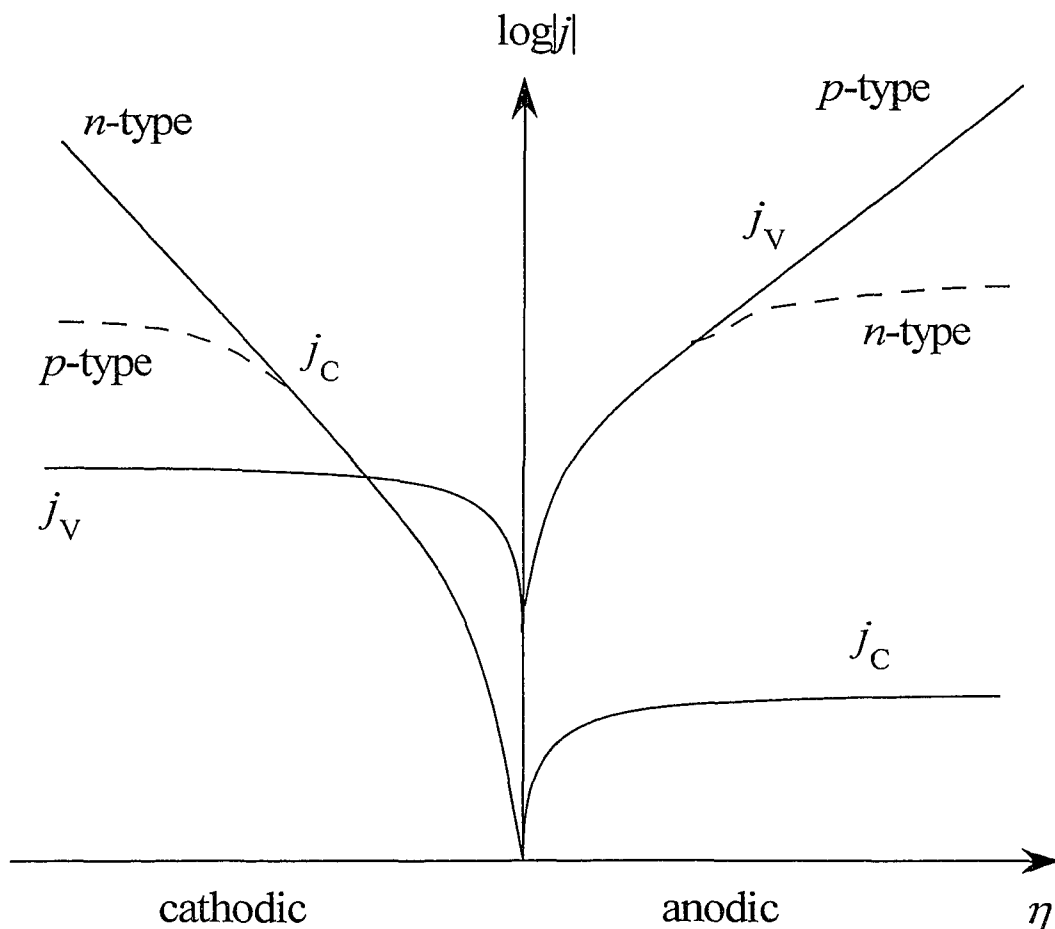
Figure 2-11 Current-potential behaviors for the partial currents in the VB (subscript V) and the CB (subscript C) in the Gerischer Model. Oxidation through the CB and reduction through the VB are almost potential independent (j_C in anodic region, j_V in cathodic region). Oxidation through the VB and reduction through the CB are potential dependent. For n-type, reduction through the CB is exponentially proportional to the potential, but for p-type, due to electrons as the minority carrier in p-type semiconductor, the current will "saturate" when the potential is negative enough. A similar situation applies to oxidation through the VB in the anodic region [1, 3, 8].

50
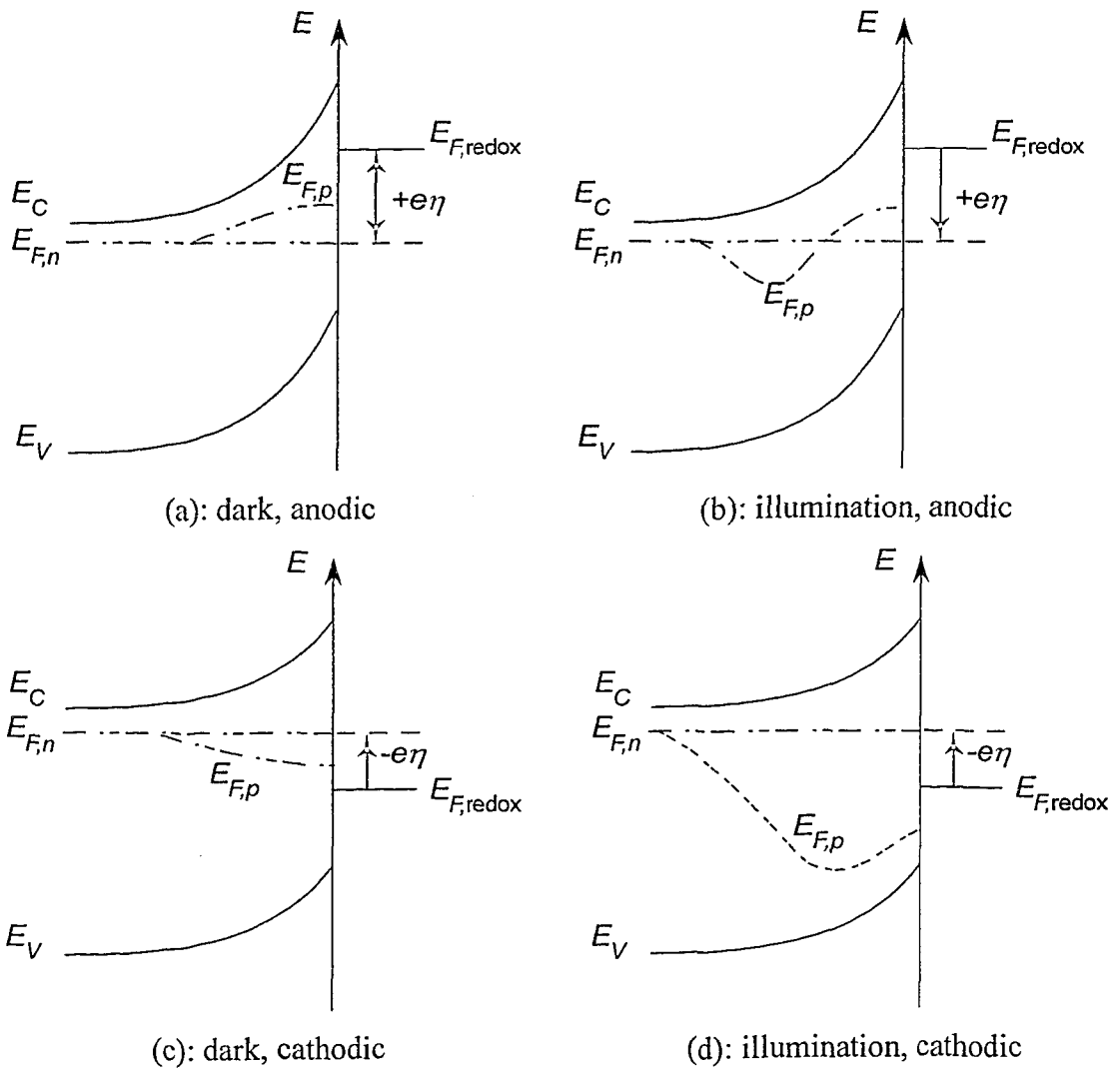
Figure 2-12 Positions of quasi-Fermi levels at different potentials for n-type semiconductors [1]. (a) and (b) are the cases of anodic polarization and (c) and (d) are the cases of cathodic polarization.
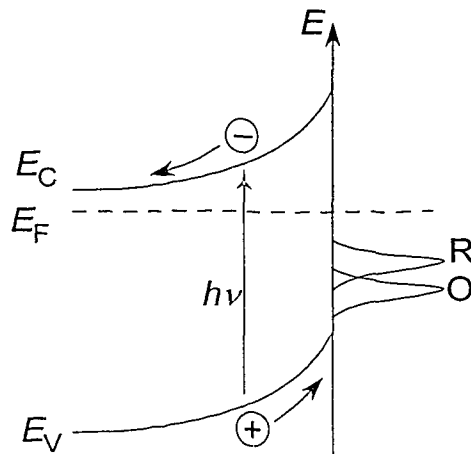
Figure 2-13 Energetic schematic diagram for photo-excitation at an n-type semiconductor electrode.

51
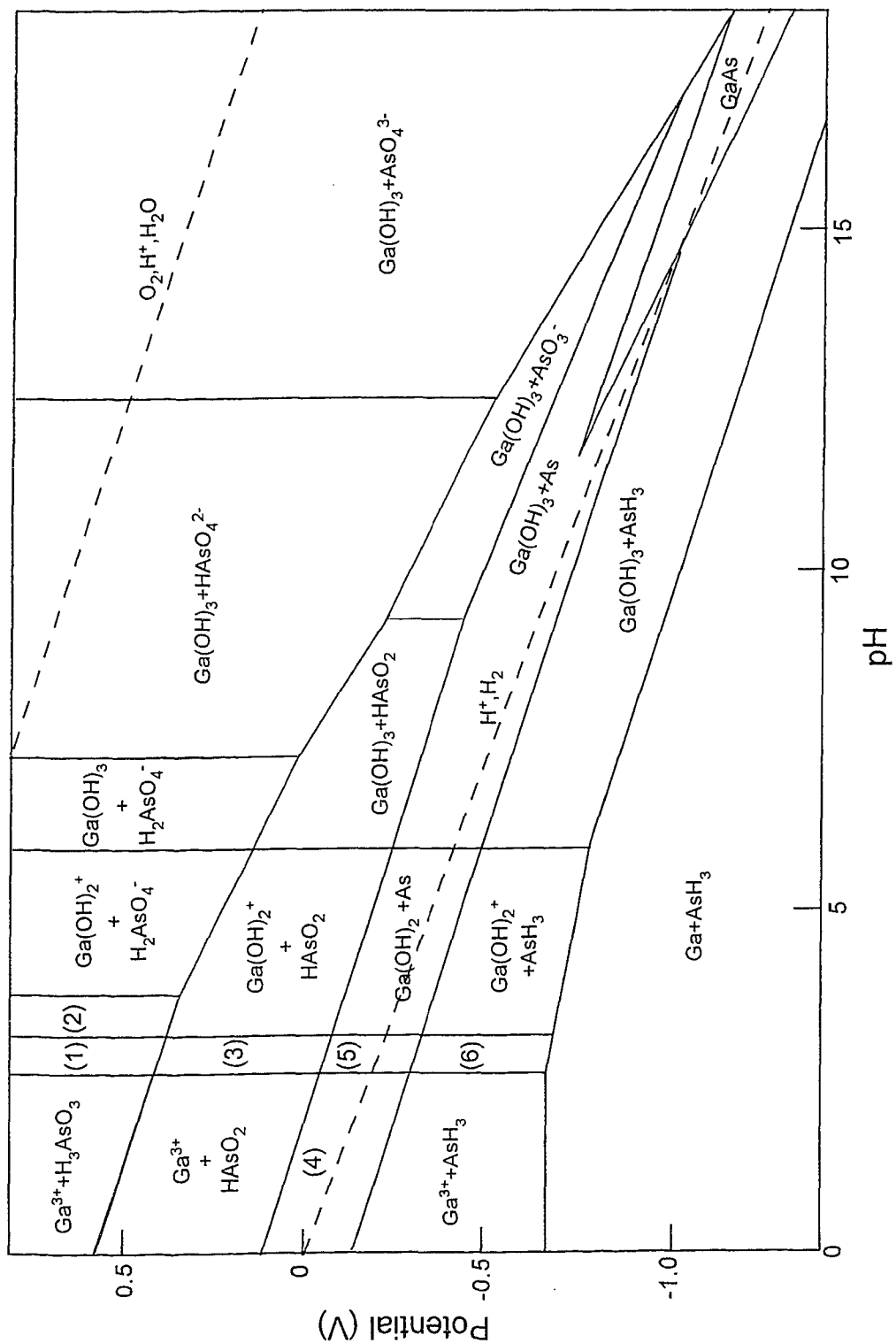
Figure 2-14 Pourbaix diagram of GaAs in water. (After reference [13]) Crowded regions are: (1) $Ga(OH)^{2+} + H_3AsO_4$; (2) $Ga(OH)_2^+ + H_3AsO_4$; (3) $Ga(OH)^{2+} + HAsO_2$; (4) $Ga^{3+} + As$; (5) $Ga(OH)^{2+} + As$; (6) $Ga(OH)^{2+} + AsH_3$.

52
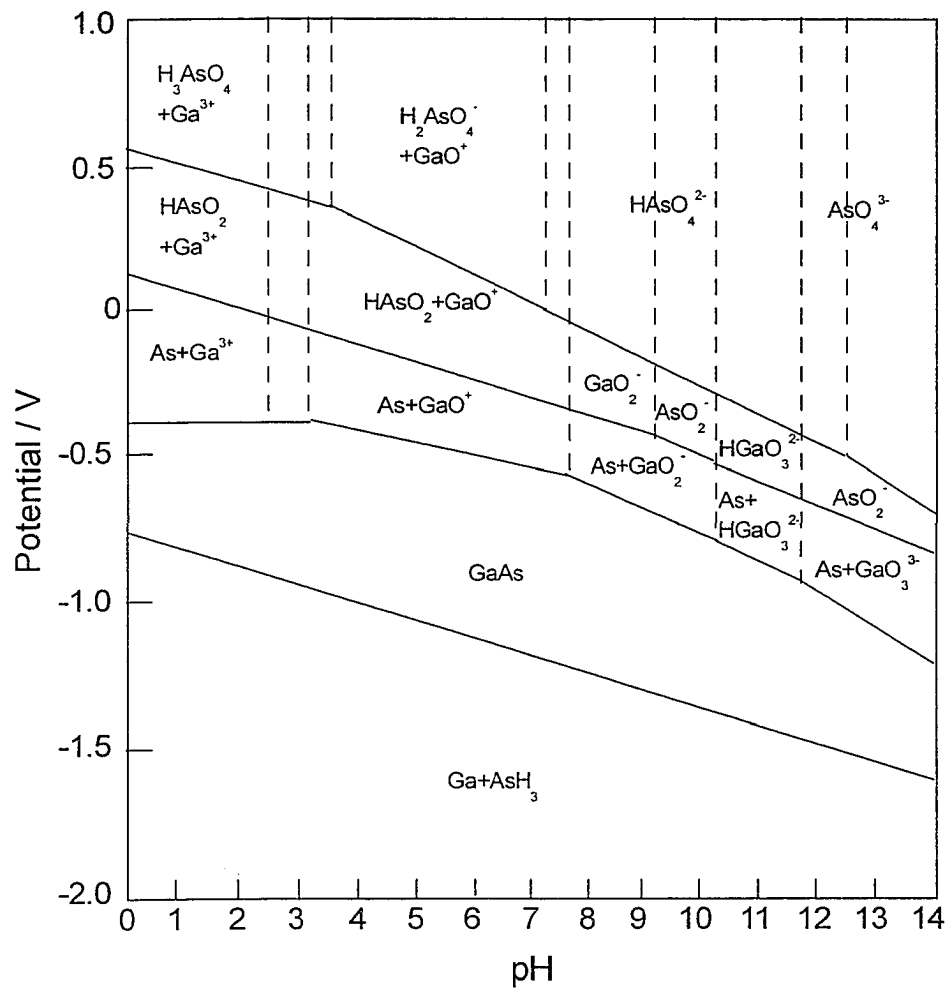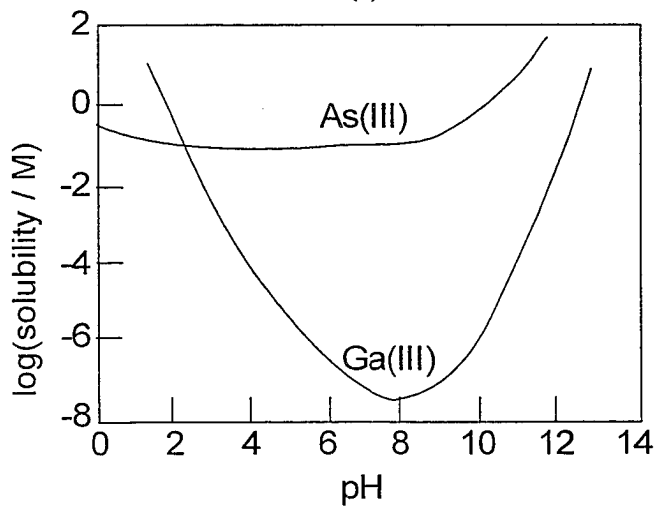
Figure 2-15 a) Equilibrium potential-pH diagram for the GaAs + H₂O system at 25°C. The hydrolysis reaction for GaAs was not included in this figure. b) Solubility of As(III) and Ga(III) species as a function of pH.
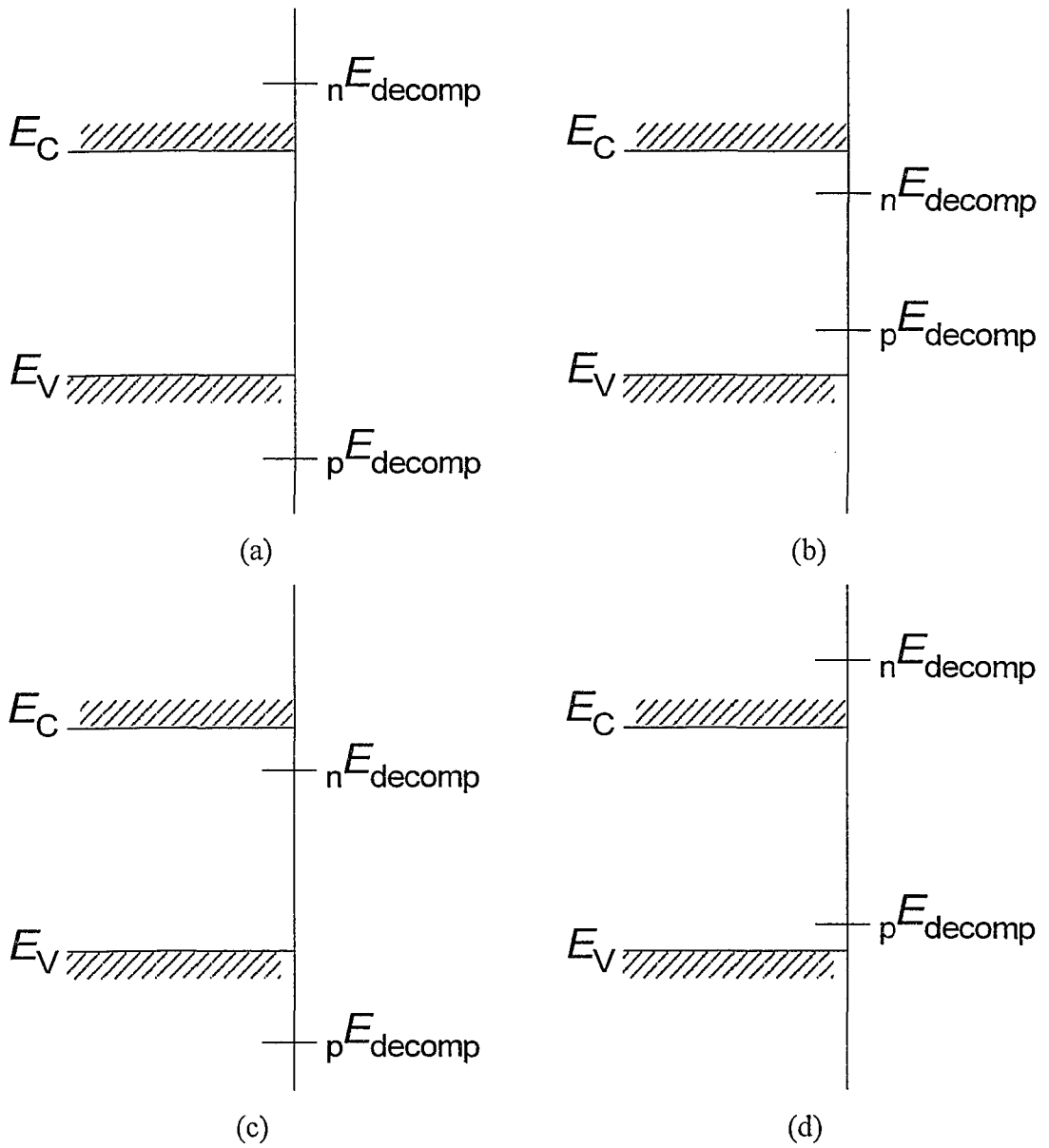
Figure 2-16 Possible positions of the decomposition energy levels relative to the band edges: a) for a relative stable semiconductor; b) instability if either electrons or holes reach the surface; c) and d) instability with regard to electrons and to holes, respectively [1].
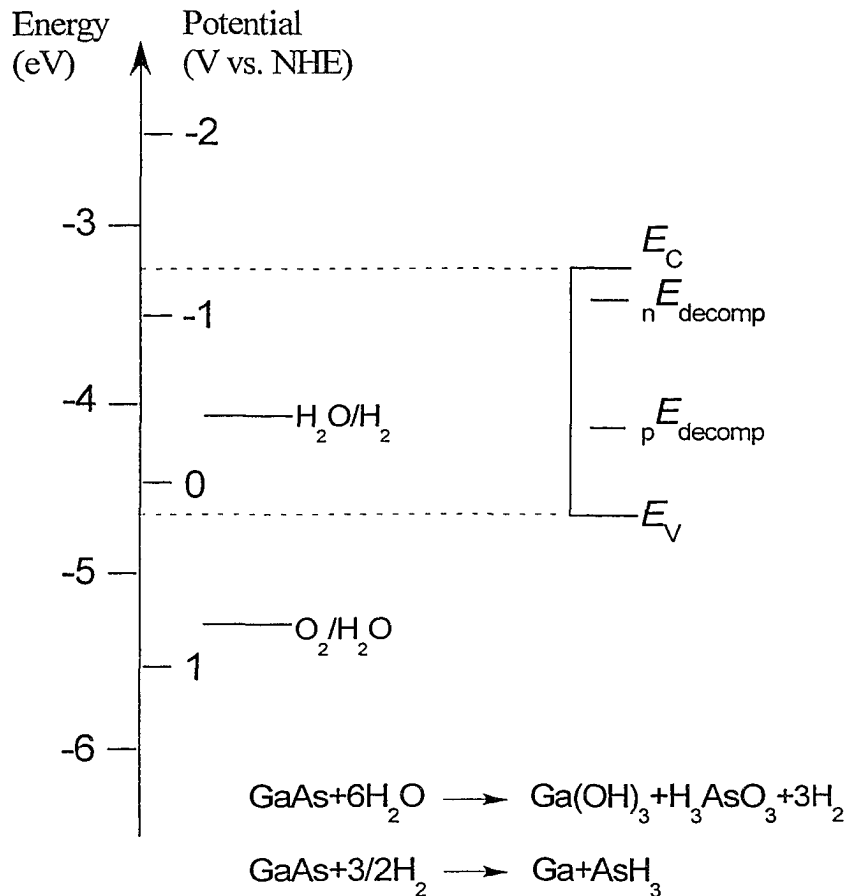
Figure 2-17 Positions and decomposition energy levels of GaAs in neutral solutions (pH = 7), from reference [13].

Table 2-2 Flat band potential and energy levels for GaAs electrodes under different pH conditions obtained by LaFlere from reference [29].

Type	Charge carrier density range (cm^{-3})	pH	V_{fb} (V vs. SHE)	E_c^s (eV vs. SHE)	E_v^s (eV vs. SHE)
n	$10^{16} - 10^{17}$	2.1	-0.95	+1.00	-0.40
		4.8	-1.10	+1.15	-0.25
		9.2	-1.35	+1.40	0.00
		12.0	-1.50	+1.55	+0.15
p	$10^{16} - 10^{17}$	2.1	+0.40	+0.90	-0.50
		4.8	+0.20	+1.10	-0.30
		9.2	0.00	+1.30	-0.10

55
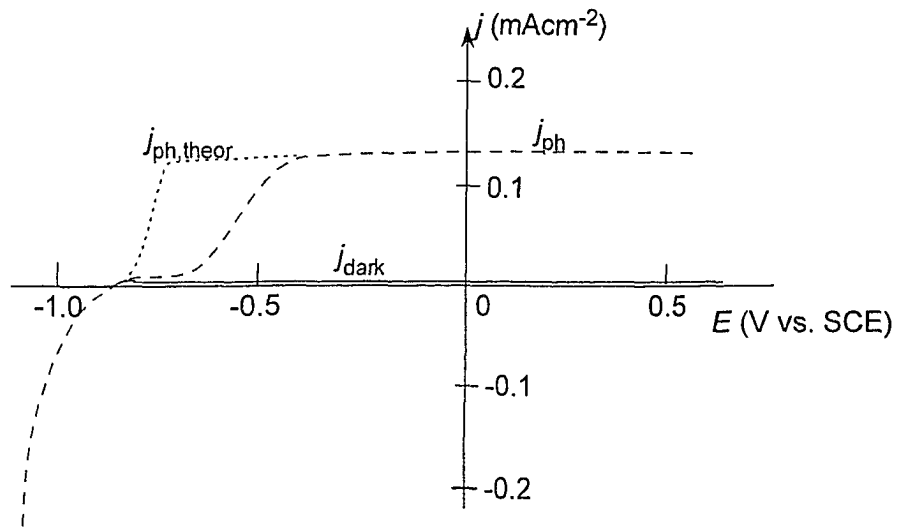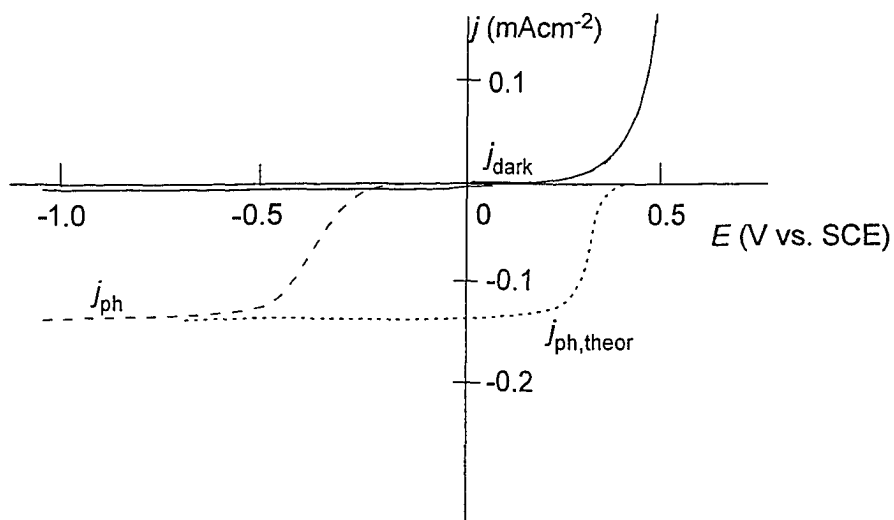
Figure 2-18 Current-potential characteristics for *n*- and *p*-GaAs electrodes in 0.1 M H₂SO₄. (a): *n*-GaAs, (b): *p*-GaAs. j_{dark}, j_{ph} and $j_{ph,theor}$ correspond to the dark, photo current and theoretical photo current densities, respectively. Deviation of j_{ph} and $j_{ph,theor}$ is due to the recombination process occurring in the space charge region.

56
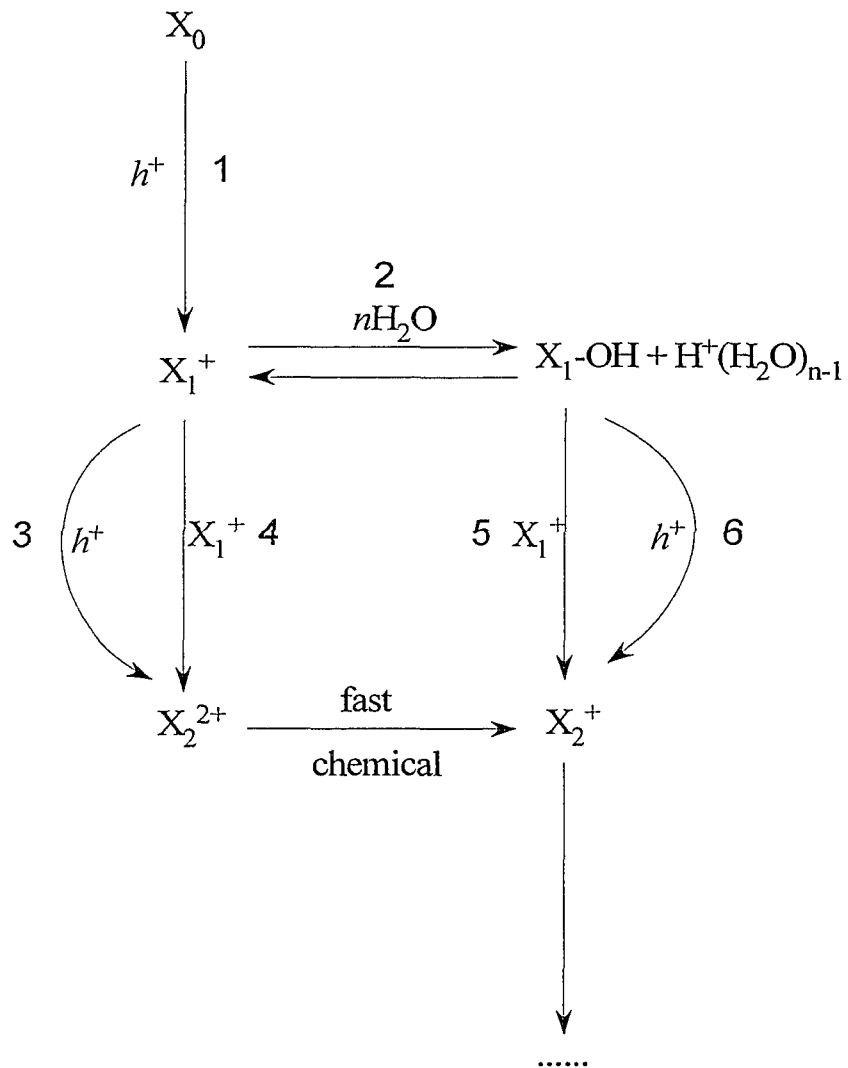
Figure 2-19 Possible pathways for GaAs continued oxidation after initial hole capture (see text for notation). Two main mechanisms have been argued in the literature. A combination of steps 1+2+4(+5) is called the H(-C) (hole oxidation and chemical step) mechanism and the other combination of 1+2+3(+6) is called the X(-C) (X_1 oxidation and chemical step) mechanism [116].

References:

[1]   Memming, R. *Semiconductor Electrochemistry*; Wiley-VCH: 2001.

[2]   Jones, D. A. *Principles and Prevention of Corrosion*; Prentice Hall: 1996.

[3]   Bard, A. J. and Faulkner, L. R. *Electrochemical Methods: Fundamentals and Applications*; John Wiley & Son Press: 1980.

[4]   Park, S.-M. and Jung-Suk, Y., *Anal. Chem.* **2003**, 75, 455A.

[5]   Macdonald, D. D., Sikora, E. and Engelhardt, G., *Electrochim. Acta* **1998**, 43, 87.

[6]   Morrison, S. R. *Electrochemistry at Semiconductor and Oxidized Metal Electrodes*; Plenum Press: 1980.

[7]   Uosaki, K. and Kita, H. In *Modern Aspects of Electrochemistry*; White, R. E., et al., Ed.; Vol. 18; Plenum Press: 1986.

[8]   Batchelor, R. A. and Hamnett, A. In *Modern Aspects of Electrochemistry*; Bockris, J. O. M., et al., Ed.; Vol. 22; Plenum Press: 1992.

[9]   Nozik, A. J. and Memming, R., *J. Phys. Chem.* **1996**, 100, 13061.

[10]   Peter, L. M., *Chem. Rev.* **1990**, 90, 753.

[11]   Koval, C. A. and Howard, J. N., *Chem. Rev.* **1992**, 92, 411.

[12]   Lewis, N. S., *J. Phys. Chem.* **1998**, B 102, 4843.

[13]   Park, S.-M. and Barber, M. E., *J. Electroanal. Chem.* **1979**, 99, 66.

[14]   Khader, M. M., *Langmuir* **1996**, 12, 1056.

[15]   Frese, K. W., Madou, M. J. and Morrison, S. R., *J. Electrochem. Soc.* **1981**, 128, 1939.

[16]   Li, J. and Peter, L. M., *J. Electroanal. Chem.* **1986**, 199, 1.

[17]   Gerischer, H., *J. Electroanal. Chem.* **1977**, 82, 133.

[18]   Bard, A. J. and Wrighton, M. S., *J. Electrochem. Soc.* **1977**, 124, 1706.

[19]   Maroun, F., Ozanam, F. and Chazalviel, J.-N., *J. Phys. Chem.* **1999**, B 103, 5280.

[20]   Abshere, T. A. and Richard M. Osgood, J., *J. Phys. Chem.* **2000**, B 104, 1602.

[21]   Ba, B., Cachet, H., Fotouhi, B. and Gorochov, O., *J. Electroanal. Chem.* **1993**, 351, 337.

[22]   Cardon, F. and Gomes, W. P., *J. Phys. D: Appl. Phys.* **1978**, 11, L63.

[23] Erne, B. H., Ozanam, F. and Chazalviel, J.-N., *J. Phys. Chem.* **1999**, B 103, 2948.

[24] Erne, B. H., Stchakovsky, M., Ozanam, F. and Chazalviel, J.-N., *J. Electrochem. Soc.* **1998**, 145, 447.

[25] Henrion, O., Klein, A. and Jaegermann, W., *Surf. Sci.* **2000**, 457, L337.

[26] Hutton, R. S., Peter, L. M., Batchelor, R. A. and Hamnett, A., *J. Electroanal. Chem.* **1994**, 375, 193.

[27] Laflere, W. H., Van Merihaeghe, R. L. and Cardon, F., *Surf. Sci.* **1976**, 59, 401.

[28] Laflere, W. H., Van Merihaeghe, R. L., Cardon, F. and Gomes, W. P., *J. Phys. D: Appl. Phys.* **1980**, 13, 2135.

[29] Frese, K. W. In *Semiconductor Electrodes*; Finklea, H. O., Ed.; Vol.; Elsevier: 1988.

[30] Notten, P. H. L. and Meerakker, J. E. A. M. V. D. *Etching of III-V Semicondutors -- An Electrochemical Approach*; Elsevier Science: 1991.

[31] Schroder, K. and Memming, R., *Ber. Bunsen-Ges. Phys. Chem.* **1985**, 89, 385.

[32] Erne, B. H., Ozanam, F. and Chazalviel, J.-N., *J. Phys. Chem.* **2000**, B 104, 11591.

[33] Allongue, P. and Blonkowski, S., *J. Electroanal. Chem.* **1991**, 317, 57.

[34] Allongue, P. and Blonkowski, S., *J. Electroanal. Chem.* **1991**, 317, 78.

[35] Meissner, D. and Memming, R., *Electrochim. Acta* **1992**, 37, 799.

[36] Allongue, P., Blonkowski, S. and Lincot, D., *J. Electroanal. Chem.* **1991**, 300, 261.

[37] Abshere, T. A. and Richmond, G. L., *J. Phys. Chem.* **1999**, B 103, 7911.

[38] Balko, B. A. and Richmond, G. L., *J. Phys. Chem.* **1993**, 97, 9002.

[39] Finnie, C. M. and Bohn, P. W., *Appl. Phys. Lett.* **1999**, 74, 1096.

[40] Hsieh, J. T., Hwang, J. M., Hwang, H. L., Ho, J. K., Huang, C. N., Chen, C. Y. and Hung, W. H., *Electrochem. Solid. St.* **2000**, 3, 395.

[41] Kauffman, J. F., Liu, C. S. and Karl, M. W., *J. Phys. Chem.* **1998**, B 102, 6766.

[42] Kriiger, Jung, C. and Gajewski, H., *J. Phys. Chem.* **1994**, 98, 12663.

[43] Uosaki, K., Shigematsu, Y., Kaneko, S. and Kita, H., *J. Phys. Chem.* **1989**, 93, 6521.

[44] Frese, K. W. and Morrison, S. R., *J. Vac. Sci. Technol., A* **1980**, 17, 609.

[45] Frese, K. W., Madou, M. J. and Morrison, S. R., *J. Phys. Chem.* **1980**, 84, 3172.

[46] Frese, K. W., Madou, M. J. and Morrison, S. R., *J. Electrochem. Soc.* **1981**, 128, 1527.

[47] Miller, B., *J. Electroanal. Chem.* **1984**, 168, 91.

[48] Miller, E. A. and Richmond, G. L., *J. Phys. Chem.* **1997**, B 101, 2669.

[49] Allongue, P. and Cachet, H., *J. Electrochem. Soc.* **1984**, 131, 2861.

[50] Allongue, P. and Cachet, H., *Electrochim. Acta* **1988**, 33, 79.

[51] Menezes, S. and Miller, B., *J. Electrochem. Soc.* **1983**, 130, 517.

[52] Gomes, W. P., Lingier, S. and Vanmaekelbergh, D., *J. Electroanal. Chem.* **1989**, 269, 237.

[53] Gomes, W. P. and Goossens, H. H. In *Advances in Electrochemical Science and Engineering*; Gerischer, H. and Tobias, C. W., Ed.; Vol.; VCH: Weinheim, 1994.

[54] Vanmaekelbergh, D., Gomes, W. P. and Cardon, F., *J. Electrochem. Soc.* **1982**, 129, 546.

[55] Vanmaekelbergh, D., Rigole, W., Gomes, W. P. and Cardon, F., *J. Chem. Soc., Faraday Trans.* **1983**, 79, 2813.

[56] Reineke, R. and Memming, R., *J. Phys. Chem.* **1992**, 96, 1310.

[57] Reineke, R. and Memming, R., *J. Phys. Chem.* **1992**, 96, 1317.

[58] Siemoneit, K., Reineke-Koch, R., Meier, A. and Memming, R., *Electrochim. Acta* **2000**, 45, 4577.

[59] Uhlendorf, I., Reineke-Koch, R. and Memming, R., *J. Phys. Chem.* **1996**, 100, 4930.

[60] Lewis, N. S., *Acc. Chem. Res.* **1990**, 23, 176.

[61] Farjardo, A. M. and Lewis, N. S., *Science* **1996**, 274, 969.

[62] Vereecken, P. M. and Searson, P. C., *J. Electrochem. Soc.* **2001**, 148, C733.

60

[63] Tomashik, Z. F., Kusyak, N. V. and Tomashik, V. N., *Inorg. Chem.* **2002**, 38, 434.

[64] Bryce, C. and Berk, D., *Ind. Eng. Chem. Res.* **1996**, 35, 4464.

[65] Erne, B. H., Ozanam, F., Stchakovsky, M., Vanmaekelbergh, D. and Chazalviel, J.-N., *J. Phys. Chem.* **2000**, B 104, 5961.

[66] Koper, M. T. M., Chaparro, A. M., Tributsch, H. and Vanmaekelbergh, D., *Langmuir* **1998**, 14, 3926.

[67] Sutter, E. M. M., Gall, M. L. and Debiemme-Chouvy, C., *J. Phys. Chem.* **2001**, B 105, 4840.

[68] Meier, A., Selmarten, D. C., Siemoneit, K., Smith, B. B. and Nozik, A. J., *J. Phys. Chem.* **1999**, B 103, 2122.

[69] Casagrande, L. G., Juang, A. and Lewis, N. S., *J. Phys. Chem.* **2000**, B 104, 5436.

[70] Buda, M., Cengher, D., Diaconescu, D. and Buda, M., *J. Appl. Electrochem.* **1998**, 28, 745.

[71] Goncalves, A.-M., Mathieu, c., Herlem, M. and Etcheberry, A., *J. Electrochem. Soc.* **2001**, 148, E8.

[72] Itagaki, M., Hasegawa, H., Watanabe, K. and Hachiya, T., *J. Electroanal. Chem.* **2003**, 557, 59.

[73] Li, J. and Peter, L. M., *J. Electroanal. Chem.* **1985**, 182, 399.

[74] Li, J., Peat, R. and Peter, L. M., *J. Electroanal. Chem.* **1986**, 200, 333.

[75] Allongue, P. and Cachet, H., *Ber. Bunsen-Ges. Phys. Chem.* **1988**, 92, 566.

[76] Chazalviel, J.-N., *Electrochim. Acta* **1990**, 35, 1545.

[77] Hens, Z. and Gomes, W. P., *J. Phys. Chem.* **1999**, B 103, 130.

[78] Memming, R., *Philips Res. Repts* **1964**, 19, 323.

[79] Nemcsics, A., *Phys. Status Solidi A* **1999**, 173, 405.

[80] Hens, Z. and Gomes, W. P., *J. Phys. Chem.* **1997**, B 101, 5814.

[81] Hens, Z. and Gomes, W. P., *Phys. Chem. Chem. Phys.* **1999**, 1, 3617.

[82] Hens, Z. and Gomes, W. P., *Phys. Chem. Chem. Phys.* **1999**, 1, 3607.

[83] Hens, Z. and Gomes, W. P., *J. Phys. Chem.* **2000**, B 104, 7725.

[84] Lingier, S. and Gomes, W. P., *Ber. Bunsenges. Phys. Chem.* **1991**, 95, 170.

[85] Steer, C. A., Weng, G. S., Luo, J. L. and Ivey, D. G., *Electrochemistry Communications* **2000**, 292, 754.

[86] Hirota, Y. and Fukuda, T., *Appl. Phys. Lett.* **1995**, 66, 2837.

[87] Xue, Q.-K., Hashizume, T. and Sakurai, T., *Appl. Surf. Sci.* **1999**, 141, 244.

[88] Yao, H., Yau, S.-L. and Itaya, K., *Appl. Phys. Lett.* **1996**, 68, 1473.

[89] Uosaki, K., Koinuma, M., Sekine, N. and Ye, S. In *Solid-Liquid Electrochemical Interfaces (ACS Symosium Series 656)*; Jerkiewicz, G., et al., Ed.; Vol.; American Chemical Society: 1997.

[90] Ye, S., Li, G., Noda, H., Uosaki, K. and Osawa, M., *Surf. Sci.* **2003**, 529, 163.

[91] Deng, Z. W., Kwok, R. W. M., Lau, W. M. and Cao, L. L., *Appl. Surf. Sci.* **2000**, 158, 58.

[92] Gerard, I., Debiemme-Chouvy, C., Vigneron, J., Bellenger, F., Kostelitz, S. and Etchberry, A., *Surf. Sci.* **1999**, 433-435, 131.

[93] Kubota, T., Ivan, J., Takahashi, M., Yoneda, K., Todokoro, Y. and Kobayashi, H., *Surf. Sci.* **2003**, 529, 329.

[94] Solomun, T., McIntyre, R., Richtering, W. and Gerischer, H., *Surf. Sci.* **1986**, 169, 414.

[95] Beerbom, M., Henrion, O., Klein, A., Mayer, T. and Jaegermann, W., *Electrochim. Acta* **2000**, 45, 4663.

[96] Gerard, I., Simon, N. and Etcheberry, A., *Appl. Surf. Sci.* **2001**, 175-176, 734.

[97] Uosaki, K., Koinuma, M., Kondo, K., Ye, S., Yagi, I., Noguchi, H., Tamura, K., Takeshita, K. and Matsushita, T., *J. Electroanal. Chem.* **1997**, 429, 13.

[98] Liu, H. C., Tsai, S. H., Hsu, J. W. and Shi, H. C., *Mater. Chem. Phys.* **1999**, 61, 117.

[99] Scherb, G., Kazimirov, A., Zegenhagen, J., Schultz, T., Feidenhans, F. and Fimland, B. O., *Appl. Phys. Lett.* **1997**, 71, 2990.

[100] Chazalviel, J.-N., Belaidi, A., Safi, M., Maroun, F., Erne, B. H. and Ozanam, F., *Electrochim. Acta* **2000**, 45, 3205.

[101] Chazalviel, J.-N., Erne, B. H., Maroun, F. and Ozanam, F., *J. Electroanal. Chem.* **2001**, 509, 108.

[102] Lockwood, D. J., *J. Solution Chem.* **2000**, 29, 1039.

[103] Aoki, I. V., Bernard, M.-C., Torresi, S. I. C. d., Deslouis, C., Melo, H. G. d., Joiret, S. and Tribollet, B., *Electrochim. Acta* **2001**, 46, 1871.

[104] Wilmsen, C. W., *Thin Solid Films* **1976**, 39, 105.

[105] Zangooie, S. and Woollam, J. A., *J. Mater. Sci. Lett.* **2000**, 19, 2171.

[106] Li, X. and Bohn, P. M., *J. Electrochem. Soc.* **2000**, 147, 1740.

[107] Finnie, C. M., Li, X. and Bohn, P. M., *J. Appl. Phys.* **1999**, 86, 4997.

[108] Lockwood, D. J., Schmuki, P., Labbe, H. J. and Fraser, J. W., *Physica* **1999**, E 4, 102.

[109] Schmuki, P., Sproule, G. I., Bardwell, J. A., Lu, Z. H. and Grahan, M. J., *J. Appl. Phys.* **1996**, 79, 7303.

[110] Schmuki, P., Fraser, J., Vitus, C. M., Graham, M. J. and Isaacs, H. S., *Localized Corrosion of GaAs Surfaces and Formation of Porous GaAs*, in *Critical Factors in Localized Corrosion II*, Natishan, P. M., et al., Editors. 1996, The Electrochemical Society. p. 226.

[111] Schmuki, P., Lockwood, D. J., Labbe, H. J. and Fraser, J., *Appl. Phys. Lett.* **1996**, 69, 1620.

[112] Schmuki, P. and Erickson, L. E., *Appl. Phys. Lett.* **1998**, 73, 2600.

[113] Schmuki, P., Erickson, L. E., Lockwood, D. J., Fraser, J. W., Champion, G. and Labbe, H. J., *Appl. Phys. Lett.* **1998**, 72, 1039.

[114] Schmuki, P., Erickson, L. E., Lockwood, D. J., Mason, N. J., Fraser, J. W., Champion, G. and Labbe, H. J., *J. Electrochem. Soc.* **1999**, 146, 735.

[115] Gerischer, H., *Faraday Discussion* **1981**, 70, 137.

[116] Vanmaekelbergh, D. and Gomes, W. P., *J. Phys. Chem.* **1990**, 94, 1571.

[117] Franz, G., Hoyler, C. and Sacher, D., *Jpn. J. Appl. Phys., Part 1* **1991**, 30, 2693.

[118] Kelly, J. J., Meerakker, J. E. A. M. v. d., Notten, P. H. L. and Tijburg, R. P., *Philips Technical Review* **1988**, 44, 61.

[119] Ven, J. v. d. and Kelly, J. J., *J. Electrochem. Soc.* **2001**, 148, G10.

[120] Simpson, W. C. and Yarmoff, J. A., *Annu. Rev. Phys. Chem.* **1996**, 47.

[121] Kelly, J. J., Kooij, E. S. and Meulenkamp, E. A., *Electrochim. Acta* **1999**, 45, 561.

[122] Notten, P. H. L., Meerakker, J. E. A. M. v. d. and Kelly, J. J. *Etching of III-V Semiconductors: an Electrochemical Approach*; Elsevier Advanced Technology: 1991.

[123] Ruberto, M. N., Zhang, X., Scarmozzino, R., Willner, A. e., Podlesnik, D. V. and Richard M. Osgood, J., *J. Electrochem. Soc.* **1991**, 138, 1174.

[124] Mandler, D. and Bard, A. J., *J. Electrochem. Soc.* **1990**, 137, 2468.

[125] Abdelghani, A. and Jacquin, C., *Mater. Lett.* **2000**, 46, 320.

[126] Gayen, S., Ermler, W. C. and Sandroff, C. J., *J. Phys. Chem.* **1991**, 95, 7357.

[127] Lebedev, M. V., *J. Phys. Chem.* **2001**, B 105, 5427.

[128] Adlkofer, K. and Tanaka, M., *Langmuir* **2001**, 17, 4267.

[129] Adlkofer, K., Eck, W., Grunze, M. and Tanaka, M., *J. Phys. Chem.* **2003**, B 107, 587.

[130] Baum, T., Ye, S. and Uosaki, K., *Langmuir* **1999**, 15, 8577.

[131] Boubour, E. and Lennox, R. B., *J. Phys. Chem.* **2000**, B 104, 9004.

[132] Ting Hou, C., Greenlief, M., Keller, S. W., Nelen, L. and Kauffman, J. F., *Chem. Mater.* **1997**, 9, 3181.

[133] Ashkenasy, G., Cahen, D., Cohen, R., Shanzer, A. and Vilan, A., *Acc. Chem. Res.* **2002**, 35, 121.

Chapter 3   *Experimental*

3.1 Materials

Both *n*- and *p*-type GaAs were used in this work. Each type of semiconductor consists of several doping levels (given by Nortel Networks), as listed in Table 3-1. As shown, most of the samples are not entire wafers doped at the levels in Table 3-1, but have epitaxial layers, 500 nm thick. For *n*-GaAs, the dopant is Si and for *p*-GaAs, the dopant is C.

Solutions were prepared with analytical grade reagents with distilled water. The acidic solution used in most of this work was 0.5 M H_2SO_4; and some tests were done in 28.5% H_3PO_4. The two acidic solutions have almost the same pH (0.05). 10% (v/v) ammonium hydroxide (2.7M, pH=11.5) was prepared for both the cleaning and testing.

3.2 Sample preparation

GaAs slices used were cleaved from 4 inch (100 mm) wafers (0.5 mm thick). Each slice was partially covered by electron beam deposited thin films to act as an ohmic contact. The ohmic metallization layer was Ti/Pt/Au for *p*-type GaAs and Pd/Ge/Au for *n*-type GaAs. The exposed plane for testing was the (100) plane. The back and edges of each slice were covered by lacquer with only part of the slice exposed to the solution (Figure 3-1).

Cleaning of the GaAs surface was done by etching the sample in a H_2SO_4:H_2O_2:H_2O (1:1:10) solution for 20 seconds, followed by cleaning in 2M HCl (20 seconds) and finally 2.7 M NH_4OH (2 minutes) to remove any etching products

65

remaining at the surface. Before each treatment, the electrode was rinsed with distilled water and then dried immediately with strong air flow. The commonly used more concentrated etching solution, $H_2SO_4:H_2O_2:H_2O$ (4:1:1), was not utilized because of its much faster etching rate. The GaAs surface was found to be blackened and dull after immersion in such a solution for ten seconds. For the samples used in this work, due to the thickness of the epitaxial layer, a milder solution was utilized. The solution content used in the work of Z. H. Lu [1] was followed, with an etching rate of ~0.32 μm/min. Etching for 20s removed ~0.1 μm GaAs. This cleaning procedure left a mirror-like surface.

3.3 Instrumentation and testing methods

3.3.1 Electrochemical cell and electrodes

A conventional three-electrode system cell was used, with GaAs as the working electrode, a Pt mesh as the counter electrode and a saturated calomel electrode (SCE) as the reference electrode (Figure 3-2). The counter electrode was put at a distance ~5 – 10 cm from the working electrode so that the electrolysis of water at the Pt mesh would not change the composition of the solution in the vicinity of the GaAs electrode. The reference electrode was placed close to the working electrode in order to measure the potential accurately. During the experiments, the cell was open to the air and not deaerated. For testing in dark conditions, the cell was put into a sealed paper box. Illumination conditions in this thesis refer to daylight conditions. It was shown in the experiments that the intensity of the daylight intensity was stable. All the experiments were carried out at room temperature (20°C).

3.3.2 Electrochemical instrumentation

All electrochemical experiments were performed on a Solartron 1287 electrochemical interface system or a Gamry 300 system. Electrochemical experiments

66

included open circuit potential measurements, DC polarization curves, Mott-Schottky measurements and impedance spectroscopy. Before all the tests, the open circuit potential was monitored until a constant value was reached. Generally, this process required ~20-25 minutes. For dc polarization curves, a scan rate of 1 or 5 mV/s was applied. For Mott-Schottky measurements, a 10 mV sinusoidal wave signal at a frequency of 1000 Hz was superimposed on the dc potential and stepped in 50 mV intervals. The data given by the instrument contains the real and imaginary parts of the ac signal versus the dc potential. This scheme was almost the same as impedance spectroscopy measurements, except that at every dc potential, the frequency was swept from 0.01 Hz to 100 kHz. All the data were then normalized by the electrode area. For impedance measurements, the cell was screened by aluminum foil to reduce the interference from the environment due to the small ac signal, especially at low frequencies.

3.3.3 Optical microscopy

An Olympus PME3-ADL optical microscope was used to observe the morphology of samples before and after testing as required. Images of the surface morphology were then digitally recorded. For some samples with small surface areas, the images were also used for surface area measurement with Image Pro Plus 4.0 software.

3.3.4 Scanning electron microscopy / energy dispersive X-ray spectroscopy

Scanning electron microscopy (SEM) micrographs of the sample surfaces and elemental compositions were obtained with a Hitachi S-2700 SEM equipped with a PGT Imix energy dispersive X-ray (EDX) analyzer (Ge x-ray detector). All images acquired were secondary electron (SE) images. EDX analysis was semi-quantitative and was performed at 20 kV.

3.3.5   X-ray photoelectron spectroscopy

X-ray photoelectron spectroscopy (XPS) analysis was performed on an AXIS 165 system with an Al Kα (1486.6 eV) X-ray source, operated at 210 W. Samples after treatment were transferred to the UHV system as soon as possible (~ 10 minutes). The X-ray source size was around 1mm with a take-off angle of 90°. A passing energy of 20 eV was used for survey spectra from 0 to 1200 eV. For high resolution spectra a passing energy of 0.1 eV was used. The high resolution spectra were done on Ga 2p, Ga 3d, As 3d, O 1s and C 1s peaks. The peak energy of 284.5 eV for C 1s was used every time for peak position calibration. Atomic composition percentages were analyzed automatically by the system using the Ga 2p, As 3d, O 1s and C 1s peaks. Table 3-2 summarizes the results of atomic concentration for an as-received sample (n-type, 1×10^{18} cm^{-3}) with respect to the physical etching time inside the vacuum chamber. It can be seen that the contamination of C at the surface was fully removed after 3 minutes of etching, while the O remains. The surface was As rich and the Ga / As ratio increased with the etching time, which is reasonable.

3.4   Data analysis approaches

3.4.1   Impedance fitting procedure

As with model fitting in most scientific work, a non-linear least square fitting (NLSF) procedure was applied. However, for electrochemical impedance data, NLSF must be performed on both the real part and imaginary part at the same time, which is referred to as complex non-linear least square (CNLS) fitting (from J. McDonald LEVM v 8.0 [2]). Before any fitting to the experiment data, an equivalent circuit was selected based on the criterion that every element in this circuit model must have a corresponding chemical / electrochemical process occurring in the system probed. The theoretical impedance expression Z_{theo} was then calculated from the equivalent circuit: the real and imaginary parts were separated as Z'_{theo} and $-Z''_{theo}$, respectively.

$$Z_{theo} = Z' - iZ''_{theo}$$ (3.1)

The fitting process is to minimize this sum:

$$S_N = \sum_{i=1}^{N} \left(v_i{}'(R_i{}')^2 + v_i{}''(R_i{}'')^2 \right)$$ (3.2)

where N is the number of data obtained from experiment results, $v_i{}'$ and $v_i{}''$ are the weighting coefficients for the real part and imaginary part respectively, and $R_i{}'$ and $R_i{}''$ are the residuals between the experiment data and theoretical model calculation of the real part and imaginary part, defined as follows:

$$R_i{}' = Z'_{i,theo} - Z'_{i,exp}$$ (3.3)

$$R_i{}'' = Z''_{i,theo} - Z''_{i,exp}$$ (3.4)

The weighting scheme adapted here is flexible. The simplest case is to treat every data point as equal in importance. The other approach used in this work is that the importance of a data point is proportional to the angular frequency of each data point. Higher frequency data has a larger weighting than lower frequency data, because in general, higher frequency data has a better signal-noise ratio. The other two approaches are similar. The weighting parameters $v_i{}'$ and $v_i{}''$ are assigned to the value of the real part and imaginary part of the experiment data or the modeling calculation results, respectively. These schemes are reasonable since the interface layers are likely capacitors and a high frequency signal is easier to pass, resulting in a smaller value for higher frequency impedance data than for lower frequency. All these can be realized using the freeware LEVM 8.05 developed by J. MacDonald [2].

69

3.4.2 XPS data analysis

The XPS data analysis work was done using the application Origin (http://www.originlab.com) with its peak fitting module (PFM). Gaussian functions without any weighting were used to deconvolute the overlapping peaks in the XPS spectra. A linear fixed baseline was applied. Parameter settings for the deconvolution are listed in Table 3-3.

70

Table 3-1 List of the GaAs samples used with their doping levels.

material type	doping density (cm^{-3})	doping element	thickness of doped layer
n-GaAs	1×10^{17}	silicon	entire wafer or 500 nm
	1×10^{18}	silicon	entire wafer or 500 nm
	2×10^{18}	silicon	500 nm
	5×10^{18}	silicon	500 nm
p-GaAs	1×10^{17}	carbon	500 nm
	1×10^{18}	carbon	500 nm
	4×10^{19}	carbon	500 nm
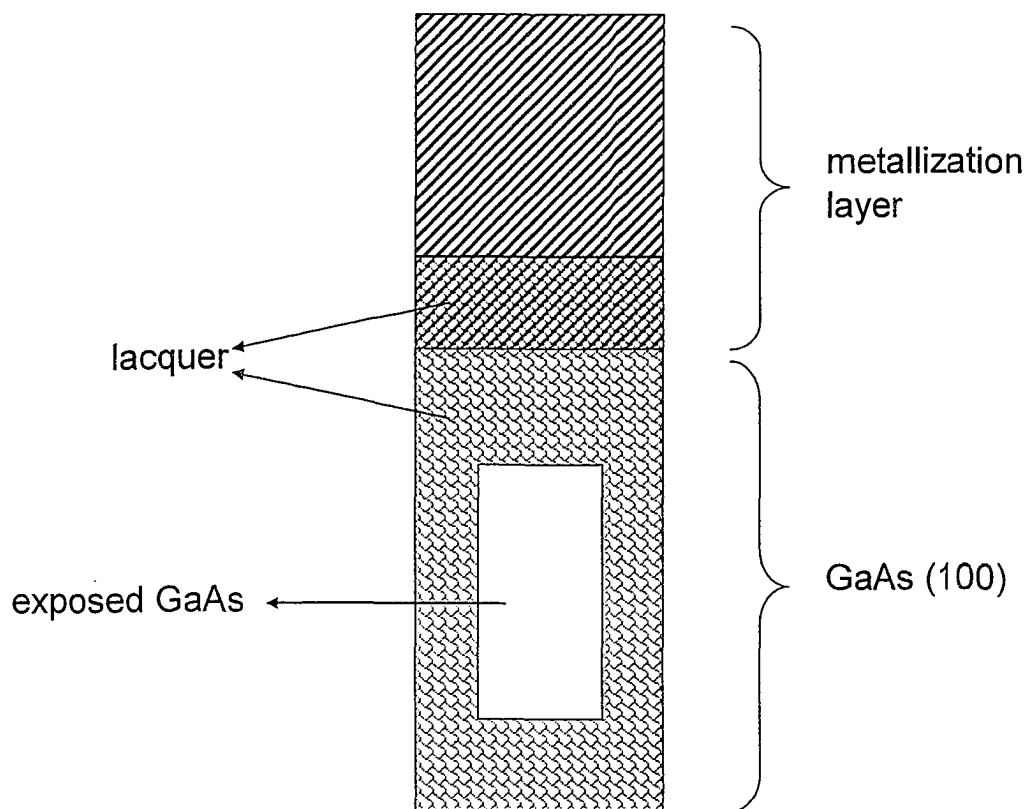
Figure 3-1 Schematic of GaAs specimens for electrochemical testing.

71
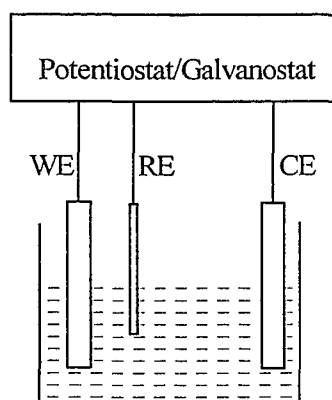
Figure 3-2 Schematic of a conventional three-electrode cell. WE: working electrode; RE: reference electrode; CE: counter electrode.

Table 3-2 Atomic concentration of an as-received GaAs sample (n-type, 1×10^{18} cm^{-3}) with respect to the physical etching time inside vacuum chamber. The etching rate is about several nanometers per minute.

etching time (minutes)	atomic concentration (%)			
	Ga 2p	As 3d	O 1s	C 1s
0	7.71	24.34	23.38	44.56
1	24.13	37.98	23.53	14.36
3	38.56	42.74	18.70	0.00
6	41.68	44.62	13.70	0.00

Table 3-3 Parameters used in XPS data deconvolution[7].

parameters	value
tolerance	0.05
confidence	0.99
prediction	0.95

---

[7] The fitting kernel is called Levenberg-Marquardt iterations. The *tolerance* is the defined as the precision requirement between the reduced chi-squares of two consecutive iterations. The *confidence interval* indicates how good an estimate the value of the fit curve is at a particular variable value. The *prediction interval* is the interval within which $100*a\%$ of all the experimental points in a series of repeated measurements are expected to fall at particular values of the variable, where a is the prediction level.

72

References

[1] Lu, Z. H., Lagarde, C., Sacher, E., Currie, J. F. and Yelon, A., *J. Vac. Sci. Technol., A* **1989**, 7, 646.

[2] McDonald, J., *LEVMW software*. 2004, http://www.physics.unc.edu/~macd.

73

Chapter 4   Results

═══

During this thesis work, as mentioned in the experimental part, the techniques used include normal electrochemical methods and surface characterization and, hence, this chapter is structured based on these two approaches.

4.1 Electrochemical methods

Normally electrochemical characterization of a reaction consists of two parts: thermodynamic data and kinetic curves. The former includes the open circuit potential (OCP), which is the equilibrium potential between the electrode and the electrolyte. When the electrode is inert, the OCP is characteristic of the redox couple in the electrolyte. On the other hand, in an inert solution, the electrode stability is inferred by the potential. The situation applicable to a semiconductor electrode is more subtle and complicated, since band bending and possible Fermi energy level pinning are also involved. Kinetics in electrochemistry represents the electrochemical reaction dependence on the externally applied or controlled potential. For a typical metal electrode, the reaction kinetic plot generally consists of three parts: the linear region, the Tafel region and the mass transport controlling region, as described in Chapter 2. Therefore, combining the data provides understanding of stability and corrosion rates. Moreover, electrochemical impedance spectroscopy (EIS) enables scientists to obtain detailed information on the mechanism of the reaction occurring at the interface, based on an equivalent circuit description and spectra simulation. Alteration of the dominant circuit elements, corresponding to the different reaction steps or surface layer formation / dissolution, is useful for understanding the whole reaction process.

4.1.1 Open circuit potentials

4.1.1.1 Theory

For an electrochemical cell at equilibrium, no net current flows. From a potential point of view, the Fermi energy level of the working electrode is the same as the counter electrode and the electrolyte as well. In most cases, the counter electrode is inert, *e.g.*, pure platinum mesh or platinum black with a large electrode area. Therefore, the potential the counter electrode measures is the redox couple in the electrolyte. For scientists who study redox couples in solution, inert electrodes (platinum, graphite, gold) are often used and the OCP detected is the equilibrium potential of the redox species, irrespective of the electrode material. The OCP of a dissolvable metal in solution will be a compromise of the equilibrium potential between the two redox potentials: metal / metal ions and the solution redox couple from the Butler-Volmer equation. For instance, the OCP of iron in deaerated acidic solution is the equilibrium potential of the two reactions: oxidation of iron into ferrous ions and the reduction of proton ions to hydrogen.

The system of a semiconductor electrode in aqueous solution requires consideration of the band bending in addition to the factors stated above in metal / electrolyte cells. Several extreme conditions are discussed here.

Case (1): The semiconductor electrode is inactive and stable in the solution at OCP and the adsorption from the solution side can be ignored. In this case, the work function of the semiconductor at the surface is fixed and equal to the value detected in vacuum (4.07 eV for GaAs). However, the band would bend into the bulk of the semiconductor, with an exponential dependence, to reach the same Fermi energy level as the redox potential of the solution. The OCP is the redox potential of the solution, not relevant to the semiconductor. Nevertheless, this OCP is not useless since it determines the band bending of the semiconductor at open circuit: the difference

75

between the known work function at the surface and the OCP. This situation best describes the systems such as TiO_2 in aqueous solution.

Case (2): The semiconductor electrode is very stable and inactive in the solution at OCP. Adsorption at the surface from the solution is very important. The adsorbates become surface states and fully pin the Fermi energy level. Good examples for such a case are silicon and germanium electrodes. The adsorption of water covers almost the entire surface and the dipole generated by the adsorption determines the potential distribution across the interface. Since the Fermi energy level of the semiconductor is pinned by the surface states, the OCP measured is the energy level of the surface states, typically in the band gap. The dipoles of the surface adsorbates are countered by the solution molecules in the double layer and thus they are affected by the pH of the solution (59 mV per unit of pH).

Case (3): Similar to the second case, band bending is not an important factor in determining the OCP. The semiconductor electrode is active in the solution and the equilibrium built across the interface is the same as for an active metal / electrolyte system. Again, the Butler-Volmer equation can be used to determine the OCP. This situation applies to those semiconductors with small band gaps or very high doping levels.

In order to investigate whether the situation of GaAs / aqueous solution is one of the three cases discussed above, these conditions were examined: the presence of metal ions (Case (1)), variable solution pH values (Case (2)) and variable doping levels (Case (3)), in combination with the illumination condition and doping type.

76

4.1.1.2 *Experimental results*

A. Stable OCP

The OCP of n-GaAs (1×10^{18} cm^{-3}) in 0.5 M H$_2$SO$_4$, after immediate immersion of the electrode into the solution under daylight conditions, is shown in Figure 4-1a. Initially the OCP is ~-0.45 V and increases to -0.31 V after about 25 minutes. In addition to a shifting of OCP, the irregular curve suggests that the GaAs surface is reactive and interacts with water in the solution. The results can be explained based on the thermodynamic data in Chapter 2. The long term instability indicates that the stabilization process is quite slow. The time dependence for the OCP for n-GaAs in 2.7 M NH$_4$OH is shown in Figure 4-1c. The corresponding p-GaAs OCPs are given in Figure 4-1b and d. The doping levels for both p- and n-GaAs were 1×10^{18} cm^{-3}. The change in OCP with time for p-GaAs in 0.5 M H$_2$SO$_4$ was much smaller (25 mV), compared with the ~150 mV found for n-GaAs. This may be due to the different oxidation rate for the different types of GaAs. A much higher concentration of holes is present at the p-GaAs / solution interface, making electrode stabilization easier. In the 2.7 M NH$_4$OH solution, the change in OCPs was small for both n- and p-GaAs (~35 mV and ~ 25 mV on n- and p-GaAs, respectively), which can be explained by the stabilization effect of NH$_4$OH (removal of surface oxides).

B. Illumination

Since the OCP is the equilibrium potential between the electrode and the solution, two factors may affect the OCP measured: redox couples and the semiconductor itself. It was suggested from Figure 4-1, that the long term instability of OCP indicates that the electrode surface influences the OCP. The influence of redox couples in the solutions will be discussed elsewhere. The types of surface conditions on the electrode include surface roughness, the presence of a surface layer and the concentration of charge carriers at the surface. The charge carrier concentration at the surface can be adjusted by the applied potential. For semiconductors, the charge carrier concentration can also be changed by illumination at sufficiently short wavelengths.

77

Figure 4-2 and Figure 4-3 show the OCP response to switching between daylight and dark conditions for n- and p-GaAs respectively. Several features can be identified. First, the response to changes in light conditions occurs over a period of several seconds. The time required to move from a stable OCP under dark conditions to a stable OCP under daylight conditions (or vice versa) is therefore not as long as that needed for a newly cleaned surface to stabilize. Illumination injects electron-hole pairs into GaAs, disturbing the thermal equilibrium previously formed. The quick response to illumination suggests that a new thermal equilibrium with external charge carrier injection can be formed by diffusion and recombination, in a much shorter time compared with the unstable surface chemical / electrochemical equilibrium. This inference supports the assumption used in this thesis that thermal equilibrium always holds for the semiconductor side and that using the Fermi-Dirac distribution equation to calculate the surface charge carrier concentration is plausible.

The second feature is the different OCP response to illumination for n- and p-GaAs. For n-GaAs, the OCP under dark conditions is higher than that for daylight conditions; the opposite observation was found for p-GaAs. Using the OCP concept for metal electrodes, a more positive OCP indicates the electrode is more resistant to anodic oxidation and an electrode with a more negative OCP is more easily oxidized. Under OCP conditions, the space charge layer of GaAs in contact with the aqueous solution is in the depletion condition. Therefore, driven by the electric field in the depletion region, minority charge carriers drift to the surface, while majority charge carriers are propelled to the bulk. For n-GaAs under illumination, light-injected holes remain at the surface and light-injected electrons are swept into the bulk. As a result, the hole concentration at the surface increases for n-GaAs, but decreases for p-GaAs. Because the corrosion of GaAs is a valence band process and the effect of the conduction band can be neglected, the hole concentration change at the surface by light directly influences the OCP, leading to easier oxidation of n-GaAs, but more difficult corrosion for p-GaAs. This is also why n-GaAs is quite stable in the dark but not when exposed to daylight. The third feature from Figure 4-2 and Figure 4-3 is that at same doping level, the change in OCP, also called photovoltage (V_{ph}), is not the same. V_{ph} is ~200 mV for n-GaAs at a doping of 1×10^{18}

78

cm^{-3}, but is only ~50 mV for p-type for the same doping. The photovoltage is larger on n-GaAs because the original hole concentration is so low that even a small injection of holes can make a significant difference. However, for p-GaAs, the injected electrons are almost all recombined with holes which are present in a large amount. A small injection of electrons would not change the OCP as much as for n-GaAs.

C. Doping levels

The doping level for GaAs directly determines the surface charge carrier concentration under dark conditions. For n-type, a higher doping level results in a smaller hole concentration in the bulk, in contrast to the case for p-type. Hence, it is expected that lower doping levels for n-GaAs are more susceptible to corrosion. Lower doping levels for p-type would lower the susceptibility to corrosion. Table 4-1 summarizes the OCPs obtained for n- and p-GaAs at several doping levels under both dark and illumination conditions.

In contrast to expectation, the OCPs for n-type GaAs over a doping range of 1×10^{17} to 2×10^{18} cm^{-3} do not vary much for both dark and daylight conditions. The expected trend was found on p-type. A possible reason for the discrepancy may be attributed to surface states. Although the concentration of surface states is low, the effect on n-type GaAs is much larger than that on p-type. OCPs for n-GaAs, except the 5×10^{18} sample, are pinned by the surface states, leading to very similar values. For 5×10^{18} cm^{-3} n-GaAs, a simple calculation (see Appendix A) shows that at this high doping level, GaAs is degenerate, $i.e.$, the Fermi energy level is located above the conduction band and the semiconductor would behave similar to a metal in dark conditions. This phenomenon can also explain why the OCP of 5×10^{18} cm^{-3} n-GaAs is close to the values obtained for p-GaAs, $i.e.$, because the charge carrier concentration at the interface is high.

D. Influence of pH

As shown in part A of this section, the OCP in the H_2SO_4 solution is more positive than that in the NH_4OH solution (Figure 4-1). Under daylight conditions, the OCP for n-

GaAs (1×10^{18} cm^{-3}) is about -310 mV vs. SCE in 0.5 M H$_2$SO$_4$ and about -870 mV in 2.7 M NH$_4$OH solution under daylight conditions. Under the same conditions for p-GaAs, the OCP is 70 mV and 440 mV in 0.5 M H$_2$SO$_4$ and 2.7 M NH$_4$OH solution respectively. The difference in OCP in the two solutions is 560 mV and 510 mV for n- and p-GaAs respectively. This is due to the differing pH values for the two solutions. The equilibrium redox reaction in the solution, with the GaAs Fermi energy level, is the reduction of oxygen to water in an indifferent electrolyte aqueous solution. Since the equilibrium potential of O$_2$, H$^+$/H$_2$O is 59 mV per unit of pH, as determined from the Nernst equation, the difference in potential for the two solutions is expected to be 660 mV, which is close to that measured (560 mV for n-GaAs and 510 mV for p-GaAs). The OCP dependence on solutions pH suggests that the Fermi energy level is partially pinned by the solution.

In order to investigate more fully the pH dependence of OCP, tests in different pH value solutions containing H$_2$SO$_4$ and Na$_2$SO$_4$ were performed. Ionic strength was adjusted to be similar by changing the concentration of Na$_2$SO$_4$. Results obtained from p-GaAs (1×10^{17} cm^{-3}) for pH values ranging from 0.0 to 2.5 are given in Figure 4-4. As the pH of the solution increases, the OCP decreases. The pH dependence for OCP is -53 mV per pH unit in the dark and -55 mV per pH unit under illumination conditions. These values are very close to the Nernst slope of -59 mV per pH unit, suggesting that the pH in the solution is a major factor affecting the OCP. However, the slightly difference from 59 mV per pH unit values also indicate that the OCP is not fully determined by the solution. In other words, the OCP is only partially pinned by the solution.

The OCP dependence on pH for p-GaAs in the series of H$_2$SO$_4$ solutions at different concentrations is in agreement with the results from both n- and p-GaAs in the two solutions. The OCP analysis indicates that the GaAs surface is not fully pinned by the solution. It should be mentioned that illumination has almost the same effect on OCP for the pH range tested.

80

E. Influence of metal ions in solution

In all the above studies on OCP, the redox couple in the solution is O_2, H^+/H_2O and the Fermi energy level at OCP was found to be pinned partially by this redox pair. Work was carried out to examine the influence of metal ions on OCP. Cu^{2+} and Ni^{2+} were utilized. Figure 4-5 shows the effect of Cu^{2+} ion concentration on OCP in 0.5 M H_2SO_4 for p-GaAs (1×10^{17} cm^{-3}). The results can be summarized as:

(1) Increasing Cu^{2+} concentration shifts the OCP more positive, both in dark and daylight conditions. This suggests that the Cu^{2+}/Cu couple, instead of the O_2, H^+/H_2O couple, is the redox couple in equilibrium with the GaAs electrode. Experimental results also show that there was no change in OCP after $[Cu^{2+}]$ exceeded 0.033 M.

(2) The difference in OCP for daylight and dark conditions is reduced with increasing $[Cu^{2+}]$. For a 0.5 M sulfuric acid solution without $[Cu^{2+}]$, the difference is about 36 mV. For $[Cu^{2+}] > 0.033$ M, the effect of light disappears, indicating that the OCP is fully pinned by the Cu^{2+}/Cu.

Results for Ni^{2+} were slightly different from those for Cu^{2+}, as shown in Figure 4-6. Similar to the results obtained from Cu^{2+}, increasing the $[Ni^{2+}]$ moves the OCP more positive. In addition, the effect of light on the OCP is less pronounced. When $[Ni^{2+}] > 8 \times 10^{-5}$ M, the OCP approaches constant values, ~70 mV in the dark and ~100 mV under illumination. However, the effect of light remains the same, unlike Cu^{2+} ions. This can be explained by the different electrochemical activity of Cu^{2+} and Ni^{2+}. The redox potential of Cu^{2+}/Cu is higher than that of Ni^{2+}/Ni, which means that Cu^{2+} can be more easily reduced than Ni^{2+}, $i.e.$, capturing of electrons and subsequent reduction of Cu^{2+} is faster than for Ni^{2+} under the same conditions. For the GaAs / Cu^{2+} system, the light-injected electrons can be completely consumed by the Cu^{2+} at the surface when the $[Cu^{2+}]$ concentration is high enough. However, on the GaAs / Ni^{2+} interface, the generated electrons can only be partially taken by Ni^{2+} at the potential tested.

81

A similar test cannot be applied to n-GaAs because of high concentration of electrons at surface and the metal ions can be easily reduced. The deposition of metals on the surface will introduce another Schottky barrier, resulting in an OCP that cannot be compared.

4.1.1.3   OCP summary

Based on the above experiments and discussion of the OCP for both n- and p-type GaAs, these conclusions can be made:

(1)   The surface of GaAs after cleaning is very sensitive to the environment, although the stabilization process is slow.

(2)   The GaAs / aqueous solution interface is not the ideal case discussed in the theory part. The OCP measured is determined by both semiconductor and the solution sides for the doping levels tested.

(3)   For the semiconductor side, doping level and illumination are the two factors that can change the surface charge carrier concentrations. The effect of doping level is found to be larger for p-type than n-type, while the effect of light is more prominent for n-type compared with p-type.

(4)   For the solution side, the pH of the solution and other metal redox couples (in any contaminant scale) can change the OCP. The dependence of OCP on pH shows that Fermi energy level at open circuit is partially pinned. Sufficient addition of Cu^{2+} can fully pin the OCP, while Ni^{2+} is less effective.

82

4.1.2 Steady-state current-voltage behavior

4.1.2.1 Theory

Steady-state experiments in electrochemistry mean that the scan rate of voltage or current, depending on the operating mode, is so small that the charging of the double layer and the space charge layer in the semiconductor are negligible and the data collected only focus on the reaction. For dynamic scanning of voltage, the current response of a capacitor can be characterized as $C\dfrac{dE}{dt}$, where C is the capacitance and $\dfrac{dE}{dt}$ the scan rate. Typical scan rates used in such tests vary from 0.1 to 1 mV/s. Taking the double layer capacitance value as 20 μFcm^{-2}, the current density due to capacitor charging is 2 – 20 $nAcm^{-2}$. For semiconductors, the capacitance of the depletion layer will be much smaller than the double layer capacitance and the background current density for charging can be safely ignored. Therefore, the current density measured by the instrument is mainly from the reactions occurring at the surface, which are dependent on the surface charge carrier concentration, adjusted by the applied potential and the surface energy levels, *i.e.*, the surface states. The current density discussed below is therefore from the charge transfer across the interface.

Similar to the studies on metal electrodes, the Butler-Volmer equation can also be applied to describe the charge transfer processes occurring at the semiconductor electrode / electrolyte interface. The equilibrium rate constant is not only dependent on activation of the Fermi energy level, but is also dependent on the surface charge carrier concentration. This is because the electronic energy level distribution on a metal electrode is continuous and the free charge carrier concentration the metal can offer is a constant, characterized by the conductivity. On a semiconductor electrode, due to the limited charge carriers, the distribution determines the number of charge carriers at the surface which are involved in electrochemical reactions. The capacitance of the space charge layer varies with the applied potential, which changes the band bending. This

83

means that the conductivity of the electrodes is not constant and it is necessary to distinguish whether the surface charge carrier concentration or overpotential limits the reaction rate and thus the current density. Based on this, kinetic analysis of the current-voltage behavior can be the combination of two limiting cases: space charge layer control and Helmholtz layer control. For the former case, the potential applied is entirely imposed on the space charge region to change the surface charge carrier concentration (Figure 4-7). The kinetic rate constants related to the corrosion process are potential independent. An ideal semiconductor / electrolyte contact matches this condition. The well-known Schottky barrier concepts can be applied. The other limiting case is the same as the situation on metal electrodes. The potential drop in the Helmholtz layer is equal to the applied potential referred to the reference. The surface charge carrier concentrations are fixed due to unvaried band bending. The kinetic description is expected to exactly follow the Butler-Volmer equation. This situation is not illustrated here and can be applied to the common metal / electrolyte interface.

Under the two limiting cases, the steady state polarization curves can be theoretically produced if the oxidization mechanism is known and the Tafel slope can be obtained. Details on how to utilize this theory for GaAs corrosion will be presented in Chapter 5.

4.1.2.2 Experimental Results

A. n-GaAs

The results for the steady-state polarization measurements of n-GaAs (1×10^{18} cm^{-3}) in 0.5 M H$_2$SO$_4$ under both dark and daylight conditions are shown in Figure 4-8. Corrosion potentials (OCP) can be found from the turning points in the polarization curves, where the observed current density changed from anodic to cathodic values or vice versus. These values are almost the same as those obtained from direct OCP tests in Section 4.1.1. Besides the OCP, the two curves also differ from each other in shape. The middle part of the curve in the dark condition shows a linear region, while under illumination conditions there is a current plateau (vertical line). The different behavior

84

can only be explained by the different hole concentration at the surface (p_s). Illumination of GaAs injects hole and electron pairs. While electrons are swept into the semiconductor bulk, holes remain at the surface, increasing the corrosion current density. Due to the constant hole injection rate by light, the current density remains unchanged over a potential region, *i.e.*, the current density at the plateau is limited by the light intensity. The slope, also called the Tafel slope in this work, from the curve under dark conditions is about 0.3-0.45 V based on several tests, which is much higher than the standard Tafel slope for a single-electron charge transfer reaction, 0.06 V. Discussion on this discrepancy is presented in Chapter 5.

The polarization curve under daylight conditions in Figure 4-8 shows three distinctive regions for the anodic part, marked as regions L1, L2 and L3, corresponding to the three regions (D1, D2 and D3) under dark conditions. In region L1, the current density is small due to the recombination of photo-injected holes and the electrons in conduction band and also the small overpotential applied. The current reaches a plateau in region L2, where the recombination effect can be excluded. The semiconductor breaks down in region L3, also found in region D3, which may be due to tunneling through the space charge region or inversion layer formation. Several tests also show that the electrode surface pretreatment directly influences how "vertical" region L2 is. Region L2 tilts when specimens have rough surfaces, for example, after long-term etching (Figure 4-9). The limiting current density in daylight conditions is about 30-50 μAcm^{-2}, much lower than that found in the literature ($\sim$1 mAcm^{-2}) [1, 2].

The polarization curves for *n*-GaAs under daylight conditions in the two different solutions (0.5 M H_2SO_4 and 2.7 M NH_4OH) are given in Figure 4-10. The two curves differ in corrosion potential and breakdown potential, while the corrosion current densities in the saturated region are similar, limited by the daylight intensity. As discussed for the OCP (Section 4.1.1), the Fermi energy level at equilibrium is almost pinned by the redox couple (metal ions or oxygen/water) in the solution side. It is believed that the band bending at OCP in the two solutions are close or same. Assuming that the breakdown potential is only dependent on the band bending and there is a fully

85

pinned Fermi energy level, the difference in the breakdown potentials for the two solutions would be same as that for the OCP and also for the flatband potentials:

$$\Delta V_{br} = \Delta V_{OCP} = \Delta V_{fb} \qquad (4.1)$$

From Figure 4-10, ΔV_{br} (~440 mV) and ΔV_{OCP} (~400 mV) are very close, but not the same, confirming the partial pinning of the Fermi energy level for GaAs by the solution.

B. *p*-GaAs

The anodic polarization curves for *p*-GaAs are much different from those for *n*-GaAs. The main reason is that holes, the oxidant, are the majority charge carriers in the semiconductor. From Mott-Schottky measurements, the flatband potential for *p*-GaAs in 0.5 M H_2SO_4 is ~400 mV. Therefore, although the contact formed between *p*-GaAs and the solution at equilibrium is still a depletion layer, the band bending is much smaller than that in *n*-GaAs and the hole concentration at the surface is much higher. This causes a faster corrosion rate for *p*-GaAs because the corrosion process is via the VB. The surface became rough after one test, observable by eye. In contrast, the surface after one test of *n*-GaAs was still mirror-like and light-reflective[8].

As stated above, the majority charge carriers for *p*-GaAs are holes and the anodic process is via the VB. The polarization curves in dark and light conditions only differ in terms of the OCP. These curves can be looked up in the literature [1] or previous work in our group [3] and are not shown in this work. The following curves for *p*-GaAs were obtained in daylight conditions.

Polarization curves for the two solutions (0.5 M H_2SO_4 and 2.7 M NH_4OH) in daylight conditions are quite similar except for the shift in the potential axis, due to the different pH values (Figure 4-11). Slopes obtained from the curve are in the range of 110

---

[8] The surface being mirror-like does not mean the surface is exactly the same as the surface before test. As will be shown in microscopy work, the surface was already roughened for *n*-GaAs. However, this roughened surface cannot be distinguished by the naked eye.

86

mV to 130 mV, different from the 60 mV result in literature [4, 5]. This value clearly suggests that the rate determining step is a one-charge transfer step as the electrochemical symmetry factor is around 0.5. It also indicates that the corrosion process is not limited by the surface hole concentration, but by the electrochemical process, because the former would result in a slope of 60 mV. In Figure 4-11, it can be seen that when the applied potential is anodically large enough, the corrosion rate decreases, or, in another words, the surface is "passivated". In the passivation region, both the hole concentration and electrochemical process are not the slowest steps. The corrosion may be limited by a mass transport process, which is independent of the potential, $e.g.$, chemical dissolution of the covered surface layer or the transport of the ions through the surface layer.

In order to compare the behavior of minority charge carriers in GaAs, cathodic polarization of p-GaAs was performed. In the acidic solution, the reduction process for p-GaAs is the reduction of oxygen dissolved in the solution, as already pointed out in the discussion of the equilibrium at OCP. When the reduction rate exceeds the diffusion rate of oxygen from the solution to the surface, the current obtained is from the reduction of the protons to hydrogen.

Figure 4-12 shows the cathodic polarization curves for p-GaAs (1×10^{18} cm^{-3}) in 0.5 M H_2SO_4 solution under dark and daylight conditions. In contrast to the anodic corrosion curves for n-GaAs in Figure 4-8, the limiting current density plateau appears in both plots under daylight conditions. A breakdown turning point was also observed at ~-0.5 V. No Tafel region was found for the dark cathodic curve for p-GaAs. This may be due to the reduction rate being limited by the diffusion of oxygen, not by the surface electron concentration. However, it is obvious that the reduction process for p-GaAs is via the CB as illumination significantly enhances the current.

C. Doping level dependence

The corrosion rate of GaAs not only depends on the applied potential, but also on the surface concentration of holes. As such, the doping level is expected to influence the corrosion behavior. If thermal equilibrium is established between the surface and the bulk

87

in GaAs, using the simplified Boltzmann distribution, the hole concentration at the surface would be proportional to the hole concentration in the bulk and also exponentially proportional to the band bending:

$$p_S = p_0 \exp\left(\frac{e\varphi_{SC}}{k_B T}\right) \tag{4.2}$$

Here p_s and p_0 represent the hole concentration at the surface and in the bulk respectively, e is the electron charge, T is the absolute temperature and k_B is the Boltzmann constant. φ_{SC} is the band bending in the space charge region. For depletion, φ_{SC} is positive for n-type and negative for p-type. When the applied potential becomes more positive, the band bending changes and p_s increases.

Polarization curves for the different doping levels of n-GaAs in 0.5 M H_2SO_4 solution under daylight conditions are shown in Figure 4-13. The current plateaus almost overlap because of fixed daylight intensity. However, breakdown potentials are different. A lower doping level corresponds to a higher breakdown potential. For example, a doping level of 1×10^{17} cm^{-3} requires $\sim$ 1V to reach breakdown, but for a doping level of 5×10^{18} cm^{-3} breakdown occurs at only $\sim$ 0.5 V. Breakdown potentials for doping levels of 1.3×10^{18} cm^{-3} and 2×10^{18} cm^{-3} are almost the same.

4.1.2.3 Polarization curves summary

Based on the above polarization results, these conclusions can be made:

(1) The anodic corrosion process is via the VB, *i.e.*, GaAs is oxidized by holes. On the other hand, the cathodic reduction process is via the CB.

(2) A Tafel region is found for n-GaAs corrosion under dark conditions, while a current plateau appears for daylight conditions. The slope is about 350-400 mV, which is much larger than expected. For p-GaAs, anodic corrosion is almost light insensitive and the Tafel slope obtained is about 110-130 mV,

indicating that the corrosion rate is limited by a one-charge transfer electrochemically controlled process.

(3) Breakdown potentials were found to depend on the doping level. A lower doping level requires a more positive potential to reach breakdown.

4.1.3   Mott-Schottky plots

Because band bending is one of the most important parameters in characterizing semiconductor corrosion behavior, it is essential to find the band bending at the potential of interest. One method is through the flatband potential. This approach is based on the assumption that the applied potential is entirely occupied by the space charge region. Under this hypothesis, the band bending can be obtained directly by the difference between the applied potential and the flatband potential:

$$\varphi_{SC} = V_{applied} - V_{fb} \tag{4.3}$$

4.1.3.1   Experimental Results

Mott-Schottky plots for n- and p-GaAs (both at a doping level of 1×10^{18} cm^{-3}) in 0.5 M H$_2$SO$_4$ and 2.7 M NH$_4$OH, with an ac perturbation at 1000 Hz, are shown in Figures 4-14 to 4-17. The valid potential region for the Mott-Schottky relationship for n-type GaAs was determined to be from about the OCP to the breakdown potential, while that for p-type GaAs was where no anodic decomposition occurred (below the OCP). The potential region below the OCP is not valid for n-type GaAs, because of the reduction of oxygen at the surface and because the current is not negligible compared with the anodic saturation current.

The flatband potential from the Mott-Schottky plot for n-type GaAs (1×10^{18} cm^{-3}) in H$_2$SO$_4$ solution was -1.0±0.1 V vs. SCE, and that for p-type GaAs was +0.4±0.1 V for the same doping density. The difference between the flatband potentials for the different

doping types is close to the band gap, 1.42 eV. This is reasonable because the doping levels are relatively high so that the Fermi levels are close to the band edges. For example, the Fermi energy level for n-GaAs at a doping level of 1×10^{18} cm^{-3} is 0.03 eV below the conduction band edge. The flatband potentials for n-GaAs and p-GaAs (1×10^{18} cm^{-3}) in NH$_4$OH were about -1.76 V and -0.25 V, respectively. The difference in this case is 1.51 V which is a bit larger than the band gap.

The differing flatband potentials in the two solutions can be explained in a similar manner to the OCP in section 4.1.1. The flatband potential shifting is because of the Fermi level pinning by the solution. Both solutions have the same O$_2$, H$^+$ /H$_2$O redox couple but at different pH values the redox potential which corresponds to the Fermi energy level and OCP is different. From the linear relationship of $1/C_{sc}^2$ vs. E, it is inferred that the potential applied mainly falls in the space charge region. With a change in potential applied, the band bending should follow the change to correspond to the varying C_{sc}. This necessitates the movement of the band edge for GaAs.

Mott-Schottky measurements assume the simplest RC equivalent circuit for the studied system. If this simple equivalent circuit is enough to describe the interface, the extracted parameters should be frequency independent, i.e., no frequency dispersion should be observed. In reality, such an ideal electrochemical system is really rare. One well known example is the one electron charge transfer reaction without any adsorption: Fe(SCN)$_6^{3-}$ / Fe(SCN)$_6^{4-}$. In order to test whether the Mott-Schottky measurements are sufficient to find the flatband potential and to determine the band bending, the frequency dependence of the Mott-Schottky plots was examined and is shown in Figure 4-18 and Figure 4-19. Figure 4-18 shows the Mott-Schottky curves for n-GaAs (1×10^{18} cm^{-3}) / H$_2$SO$_4$ at different frequencies from 100 Hz to 7500 Hz. Although a good linear relationship was obtained over a certain potential region for all the frequencies tested, the flatband potential and doping level calculated from the plots change with the frequency. From 100 Hz to 1000 Hz, only a slight difference in the curves is found. A higher applied frequency results in a higher doping level calculated from the slope and a more negative flatband potential is produced from the intercept. All these results imply that the RC

90

circuit is not adequate for describing the studied interface. A search for a good equivalent circuit was performed using the impedance approach. Further discussion on the validity of using Mott-Schottky measurement to determine the flatband potential is presented in Chapter 5.

4.1.3.2 Summary

Based on the results presented on the direct Mott-Schottky measurements, these conclusions can be made:

(1) Valid Mott-Schottky regions are found for both n- and p-GaAs in both solutions. The difference in flatband potentials for n- and p-GaAs, extracted from the plots, is very close to the band gap value, indicating the validity pf using direct Mott-Schottky measurements to determine the flatband potentials. Another inference is that the capacitance measured from Mott-Schottky plots is mainly from the space charge region.

(2) The Mott-Schottky plots depend on the frequency utilized, indicating the inherent RC equivalent circuit in direct Mott-Schottky measurement is not sufficient to describe the GaAs / aqueous electrolyte interface of interest. Impedance spectroscopy may be a better technique to uncover the real equivalent circuit and find the real capacitance of the depletion region.

4.1.4 Electrochemical impedance spectra (EIS)

Information from the polarization curves, OCP tests and Mott-Schottky measurements, as given above include the thermodynamic stability, corrosion rate and flatband potentials. However, how the corrosion occurs and what is the dependence of the corrosion rate on the reaction steps are still not clear. Furthermore, the equivalent circuit across the interface appears not to be as simple as the equivalent circuit of a resistance

91

and capacitance in series. Therefore, EIS was performed to explore more details on the corrosion of GaAs.

4.1.4.1 n-Type

A. Experimental data

A series of impedance spectra was recorded for n-GaAs (1×10^{18} cm^{-3}) electrodes in 0.5 M H$_2$SO$_4$ solution under dark conditions, in the potential range from OCP to breakdown (Figure 4-20 to Figure 4-22). Generally, the frequency used varied from 100 kHz to 0.01 Hz. Under dark conditions, the processes occurring at the interface are relatively simple. No surface recombination is expected as no external charge carriers are injected. Figure 4-20 is the spectrum at 50 mV and Figure 4-21 is the one at 500 mV. The spectra only consist of a semicircle (loop) at potentials before breakdown (~900 mV). At potentials after breakdown, e.g., 1150 mV, a pair of capacitive and inductive loops appears at low frequencies, joining the already existing capacitive loop at high frequencies (Figure 4-22). Empirically, the impedance spectra in Figure 4-20 and Figure 4-21 before breakdown, with just one loop, can be fit to an equivalent circuit $R_s(R_{ct1}C_{SC})$ (Randles circuit) (Figure 4-25a). The reason why a capacitor is assigned to the space charge region is described below. The data after breakdown shows two capacitive loops and one inductive loop and can be fit to the equivalent circuit in Figure 4-25b. When the sample breaks down, the charge carrier concentration at the surface is quite high, comparable to the charge concentration in solution. At this time, the potential drop in the double layer cannot be neglected and reactions occurring in the double layer should also be considered, resulting in a ($R_{ct2}C_{dl}$) circuit. After breakdown, the rate-determining step of the corrosion reaction may not be the one at mild potentials. A Faradaic adsorption process being the slowest oxidation step will lead to an inductive loop, which will be discussed in Chapter 5. The inductive loop has an equivalent circuit of R_L and L in series. The terms used in the equivalent circuits above are explained in the spectra fitting section.

The impedance spectra for n-GaAs (1×10^{18} cm^{-3}) electrodes in 2.7 M NH$_4$OH under dark conditions, in a potential range from OCP to breakdown, were also obtained. Two typical curves are shown in Figure 4-23 and Figure 4-24. Similar to the curves in the

92

0.5 M H_2SO_4 solution, the spectra can be fit using the equivalent circuit of Figure 4-25a before breakdown and using the one in Figure 4-25b for those after breakdown.

The impedance data series for n-GaAs (1×10^{18} cm^{-3}) in 0.5 M H_2SO_4 solution obtained under daylight conditions, are shown in Figure 4-26 to Figure 4-28. At potentials close to the open circuit potential (-0.23 V), the spectrum shows two capacitive loops (Figure 4-26). For progressively increasing potentials, the second capacitive loop at low frequency diminishes. After the potential reaches breakdown, a capacitive and inductive loop pair was observed, similar to that under dark conditions. Since the second capacitive loop does not appear in the data collected under dark conditions and disappears at higher potentials under illumination conditions, it is likely related to the recombination process. From the work by Vanmaekelbergh and Cardon [6], the model for impedance associated with surface recombination at an illuminated semiconductor / electrolyte interface is a $R_{r,1}(R_{r,2}C_R)$ equivalent circuit (Figure 4-25c) with element values:

$$1/R_{r,1} = (e^2/k_BT)\beta_n n_S[\text{ess}] \qquad (4.4)$$

$$1/R_{r,2} = (e^2/k_BT)\beta_p p_S[\text{ess}] \qquad (4.5)$$

$$C_R = (e^2/k_BT)[\text{ess}] \qquad (4.6)$$

where [ess] is the surface concentration of empty surface states, n_s and p_s are the surface concentrations of electrons and holes, respectively, and β_n and β_p are the kinetic rate constants for the recombination process and hole capturing process respectively. The simplicity of equations (0.4)-(0.6) is based on the assumption that the hole concentration in the valence band is stationary. Taking a typical value of 10^{12} cm^{-2} for the surface states density [7], gives C_R equal to 6.4 μFcm^{-2}, which can only be detected in the low frequency region because the capacitance of depletion layer is on the hundreds of nFcm^{-2} scale. With more positive potentials applied, C_R decreases and the recombination capacitive loop will incorporate into the loop of the depletion region and the recombination impedance will disappear. This trend is the same as observed here. Hence, the second capacitive loop at low frequency region is identified as the recombination impedance.

93

B. Impedance spectra fitting

In EIS analysis a common problem encountered is the physical significance of the elements in the equivalent circuit used for fitting. As mentioned above, the equivalent circuits shown in Figure 4-25 were used in this thesis to fit the impedance spectra obtained. Figure 4-25a is a general expression of Randles circuit. The elements in the circuit used in this thesis have a similar physical significance to that in metal electrodes system.

R_s is the combined resistance of the solution and the bulk semiconductor. This is because metal electrodes have a very small resistance, compared with that of the solution ($\sim$50 Ωcm^{-2}). However, the resistivity of GaAs is higher than that of a concentrated ionic solution. The value of R_s from fitting (intercept at horizontal axis at high frequency) is several kΩcm^2. For metal electrodes R_s is independent of the varying applied potential. For GaAs electrodes, this serial resistance can change slightly with the potential, because the width of space charge region depends on the potential.

R_{ct1} is the resistance characterizing the charge transfer across the interface. It indicates how the potential can influence the electrochemical reaction. As ac impedance is a steady-state technique, the value of R_{ct1} can be compared to the slopes of a steady-state current-voltage curve. From definition,

$$R_{ct1} = \left(\frac{dE}{dj} \right)_{ss} \tag{4.7}$$

where the subscript "ss" represents steady-state conditions. For a steady-state current-voltage curve with a Tafel relationship

$$E = a + b \log j \tag{4.8}$$

The Tafel slope b is defined as

$$b = \left(\frac{dE}{d \log j} \right)_{ss} \tag{4.9}$$

94

R_{ctl} is a resistance at a fixed potential and the Tafel slope b is used for the potential region with a Tafel relationship. To compare them, assuming at a potential E_1 with corresponding steady-state dc current j_1, Eq. (4.9) can be rewritten as

$$b = \left(\frac{dE}{d \log j} \right)_{ss} = 2.303 j_1 \left(\frac{dE}{dj} \right)_{ss} = 2.303 j_1 R_{ctl} \qquad (4.10)$$

From the intercept of the Nyquist plot in Figure 4-21, R_{ctl} has a value of 1.3 $M\Omega cm^2$ at 0.5 V, which is very close to the slope calculated from the polarization curve (Figure 4-8) (~ 1 $M\Omega cm^2$) if surface roughness is considered, indicating that R_{ctl} is the polarization resistance.

The capacitance of the loop can be calculated from the frequency of the semicircle apex through this relationship

$$\omega_{apex} = 2 \pi f_{apex} = \frac{1}{R_{ctl} C_{sc}} \qquad (4.11)$$

or

$$C_{sc} = \frac{1}{2 \pi f_{apex} R_{ctl}} \qquad (4.12)$$

An example is given in the following. From Figure 4-21, for n-GaAs (1×10^{18} cm^{-3}) in 0.5 M H_2SO_4 solution under dark conditions at 500 mV, $f_{apex} = 0.5$ Hz and $R_{ctl} = 1.35$ $M\Omega$. From Eq. (4.12), $C_{SC} = 0.24$ μFcm^{-2}, a typical value for depletion region capacitance. Repeating the calculation, the capacitance in the impedance semicircle for n-GaAs (1×10^{18} cm^{-3}) in 0.5 M H_2SO_4 solution under dark conditions is in the range of ~ 0.2 $- 0.4$ μFcm^{-2} (Table 4-2). The double layer capacitance is generally ~ 20 μFcm^{-2} for metal / electrolyte interfaces and could be smaller e.g., 5 μFcm^{-2}, for semiconductor / electrolyte interfaces. The typical depletion layer value of the capacitance from the impedance semicircle suggests that the capacitance is mainly from the depletion region. Referring to the potential distribution concept, it is suggested that the applied potential mainly falls in the smaller capacitor, that is, the space charge layer, instead of the double

layer. Therefore, this capacitance is dominated by the space charge capacitance (subscribed with "sc") and it is reasonable to use it for flatband potential determination from the Mott-Schottky relationship.

A plot of $1/C_{sc}^2$ using the fit values from Table 4-2 is shown in Figure 4-29. Firstly, the linear relationship confirms that the capacitance extracted from the impedance data is that of the space charge region, and compares well with the Mott-Schottky plot in Figure 4-14. The linear fitting gives a flatband potential -0.71 V vs. SCE and a doping density of 1.25×10^{18} cm^{-3}. This flatband potential is more positive than that in Figure 4-14. Discussion of this discrepancy will be presented in Chapter 5. The shape of the plot in Figure 4-29 is also quite similar to that of Figure 4-14, with a linear region and then a turning point, which is related to the breakdown of GaAs.

The logarithmic plot of R_{ct1} vs. applied potentials from Table 4-2 is shown in Figure 4-30. This curve has a linear region of potential from 0.1 to 0.8 V, which suggests that this resistance is exponentially proportional to the potential, corresponding to the Tafel region in the polarization curve (Figure 4-8). R_{ct1} can be attributed to the resistance of the Schottky barrier between the semiconductor and the electrolyte. The charge transfer resistor R_{ct1} and the capacitor from the space charge region are in parallel, which means that the electrochemical reaction occurs mainly in the space charge region, not in the double layer. The sudden decrease of $\ln(R_{ct1})$ in Figure 4-30 corresponds to the turning point in the Mott-Schottky plot in Figure 4-29. This is understandable as breakdown would result in a large amount of charge carriers at the surface, accelerating the corrosion rates.

The above fitting procedures were also applied to the impedance data obtained from n-GaAs (1×10^{18} cm^{-3}) in 0.5 M H_2SO_4 solution under illumination conditions. The fit to the data obtained is given in Table 4-3. In relative terms, the values of C_{sc} are larger than those under dark conditions, which can be explained by the light effect. The external injection of charge carriers under illumination narrows the depletion layer width.

96

According to definition, $C_{sc} = \dfrac{\varepsilon}{W}$, where ε is dielectric constant and W is the depletion layer width. With illumination, the depletion layer gets thinner, i.e., W decreases, resulting in an increase in C_{sc}. A linear dependence within a certain potential region (from OCP to ~0.8 V) of $1/C_{sc}^{2}$ vs. E from the fitted data (Figure 4-31) indicates the capacitance is from depletion layer and agrees with the Mott-Schottky relationship. The flatband potential from Figure 4-31 is ~ -0.85 V and the doping level is ~1.20×10^{18} cm^{-3}. The flatband potential is more negative than that obtained under dark conditions with the same fitting procedures. The more negative the flatband potential, the more easily the n-GaAs sample can be oxidized, which is consistent with the OCP results in Section 4.1.1. The Mott-Schottky plot also has a turning point, similar to the direct Mott-Schottky measurements.

The R_{ct1} values in Table 4-3 are smaller than those in Table 4-2 at corresponding potentials. A smaller R_{ct1} means that the corrosion is faster, which agrees with the situation for illumination conditions, compared with the dark condition. From Figure 4-30, a Tafel relationship is shown for the R_{ct1} under dark conditions. However, for R_{ct1} under illumination conditions, the dependence on the applied potential is quite different. There is a relatively constant region of R_{ct1}, as shown in the curve of R_{ct1} vs. E in Figure 4-32. Comparison with the polarization curve shape in Figure 4-8, under illumination conditions, indicates that a current plateau was present. The potential region of the current plateau matches the R_{ct1} plateau, which is evidence that R_{ct1} from impedance is the polarization resistance under illumination conditions. When the potential approaches breakdown, R_{ct1} decreases rapidly, indicating that accelerated corrosion occurs.

Fitting the spectra at potentials after breakdown is not valuable because the electrode system is not at steady-state, due to the large current flowing and rapidly changing surface conditions, and is not presented in this thesis.

97

4.1.4.2 p-Type

Impedance spectra for p-GaAs are a little more difficult to measure. As mentioned above, impedance spectroscopy is a steady-state technique, which also requires that during the measurement, the electrode conditions remain unchanged. For the corrosion of p-GaAs, due to the high concentration of holes at the surface, the corrosion rate is much faster than that for n-GaAs. The time needed for one impedance spectrum acquisition is ~10 minutes. Shown below is a simple calculation on how much GaAs will be dissolved in this time interval. From the polarization curves in Figure 4-11, choosing the typical corrosion current density as 1 μAcm^{-2}, the number of GaAs molecules dissolved in 10 minutes can be calculated, assuming the electrode area is ~0.5 cm^{-2}.

$$\frac{j \times A \times t}{nF} = \frac{10^{-6} \times 0.5 \times 10 \times 60}{6 \times 96500} \approx 5 \times 10^{-10} \text{ mol}$$

For an uniform dissolution of the surface (layer by layer),

$$\frac{5 \times 10^{-10} \text{mol} \times 144.64 \text{gmol}^{-1}}{5.32 \text{gcm}^{-3} \times 0.5 \text{cm}^2} = 0.27 \text{nm}$$

which means that about half of one unit cell has been dissolved (lattice constant of GaAs unit cell is 0.565 nm). If corrosion rate is at 10 μAcm^{-2}, then ~2.7 nm will decompose in 10 minutes, heavily influencing the surface conditions. Even if the corrosion rate is at 1 μAcm^{-2}, after a series of impedance measurements, the surface has changed (e.g., surface area, surface roughness, concentration of surface states, etc.) and the impedance spectra are not suitable for comparison purposes. This was confirmed from the unstable impedance spectra obtained for p-GaAs.

Some of the impedance spectra for p-GaAs corroded in both 0.5 M H_2SO_4 and 2.7 M NH_4OH solutions at different potentials are shown in Figures 4-33 to 4-37. The spectra have almost the same shape as those for n-GaAs. At small overpotentials, only one semicircle appears in the Nyquist plot, and at highly polarized conditions, a capacitive and inductive loop pair emerges. This implies that the corrosion mechanism for p-GaAs might be the same as that for n-GaAs, which will be discussed further in Chapter 5.

98

4.2 Surface characterization

4.2.1 Microscopy

4.2.1.1 Optical Microscopy

Optical microscopy is useful to examine the GaAs single crystal surface after every chemical or electrochemical treatment. Because of its relatively low resolution, compared to electron microscopy, p-type GaAs was chosen as an example to investigate how each pretreatment and corrosion change the surface, because corrosion and etching are expected to occur faster.

A series of optical images are given in Figure 4-38. These images were obtained at the same position in the sample for better comparison after a sequential chemical or electrochemical treatment. For reference purposes, "etching" and "cleaning" below refer to the processes of etching in the $H_2SO_4/H_2O_2/H_2O$ mixture solution and cleaning in NH_4OH solution as stated in the experimental section. Figure 4-38a shows an image of an as-received sample, with a smooth surface, and it is almost free of defects. The sample was then etched in the $H_2SO_4/H_2O_2/H_2O$ mixture solution as stated in the experimental section and the image is shown in Figure 4-38b. Somewhat irregular regions on the surface can be seen. After cleaning in 2.7 M NH_4OH, more irregularities were revealed, as shown in Figure 4-38c. The sample from Figure 4-38c was then polarized from -0.2 to 0.5 V vs. SCE, resulting in the adhesion (adsorption) of corrosion products (Figure 4-38d). The sample in Figure 4-38d was subsequently immersed into NH_4OH solution and the resultant surface image is shown in Figure 4-38e. Corrosion products were produced after electrochemical etching (Figure 4-38d) and evidently, they have been removed by the 2.7 M NH_4OH solution, exposing a relatively smooth surface. From these sequential treatments, it can be seen that the $H_2SO_4/H_2O_2/H_2O$ mixture can etch the GaAs surface; however, the etched products are left at the surface. These etched products are probably the same as the corrosion products in Figure 4-38d, which are dissolvable in 2.7

M NH$_4$OH solution. It can be concluded that using 2.7 M NH$_4$OH solution to clean the GaAs surface after etching is necessary.

Another series of optical images were acquired for *n*-GaAs samples at different doping levels after relatively long term polarization (two cycles from -0.75V to 1.5V, at 1.5V which is above the breakdown potential for all GaAs samples) in 0.5 M H$_2$SO$_4$ solution. The doping levels examined were 1×10^{17}, 1.3×10^{18}, 2×10^{18} and 5×10^{18} cm^{-3}. The images are given in Figure 4-39. The images of the surfaces of these different doping levels are quite different. In this case, the higher the doping level, the more heavily corroded is the sample. However, this is not in conflict with the results obtained from OCP in Section 4.1.1. The corroded surface for the sample doped at 1×10^{17} cm^{-3} (Figure 4-39a) only has a small number of dots or pits and the corroded surface for the 5×10^{18} cm^{-3} doped sample (Figure 4-39d) is fully covered by a compact layer, most likely being oxides. It is interesting that the corroded surface for a doping level of 1.3×10^{18} cm^{-3} is scattered with cross marks and at a doping level of 2×10^{18} cm^{-3}, it is distributed with square marks. This may be due to orientation selection during corrosion (most likely (111) plane). The trend to heavier corrosion for higher doping levels can be explained by the different breakdown potentials for different doping levels. In Section 4.1.2.2, it was shown that for *n*-GaAs, higher doping levels result in easier breakdown. Therefore, the sample with a doping level of 5×10^{18} cm^{-3} was polarized with the most anodic charges, leaving much more corrosion products at the surface. The doping level of 1×10^{17} cm^{-3} has the fewest anodic charges.

4.2.1.2 Scanning electron microscopy

Scanning electron microscopy (SEM) was used to confirm the GaAs surface cleaning procedures. All the surface images shown are secondary electron (SE) images. The results for *n*-GaAs (1×10^{18} cm^{-3}), after a sequential etching and cleaning, are shown in Figure 4-40a-c. The as-received sample again shows the smoothest surface (Figure 4-40a) and a groove can be seen in Figure 4-40b after the etching procedure. More

100

grooves are exposed after the cleaning in 2.7 M NH_4OH solution (Figure 4-40c), indicating that etching products remained at the surface. This again verifies that etching alone is not adequate to produce a fresh surface.

The electrochemically corroded surfaces of n-GaAs (1×10^{18} cm^{-3}) in the two solutions were also examined by the SEM (Figure 4-40d-f). Corrosion in H_2SO_4 solution using two potential sweeping polarizations from OCP to 1.2 V at a scan rate of 5 mVs^{-1} leaves many bumps and clusters on the surface (Figure 4-40d). Cleaning of the sample from Figure 4-40d in NH_4OH solution using similar polarization conditions (from OCP to 1.2 V in two sweeps at a scan rate of 5 mVs^{-1}) reveals the attacked surface underneath (Figure 4-40e), characteristic of pitting. Unlike the H_2SO_4 solution, the corroded surface in NH_4OH solution is almost totally smooth (Figure 4-40f), $i.e.$, no pitting occurred.

Another interesting result obtained from SEM is the orientated dissolution of GaAs. The SEM SE image of corroded surface of n-GaAs (5×10^{18} cm^{-3}), after one polarization sweep in 0.5 M H_2SO_4 solution under daylight conditions from OCP to 1.0 V, is shown in Figure 4-41. Figure 4-41a is the surface image just after corrosion with "dumb bell" marks shown. These marks remained on the surface (Figure 4-41b) after cleaning in NH_4OH solution, although the overall surface was smoothed, compared with Figure 4-41a.

Three types of surface patterns after the etching during the sample preparation stage have been found: squares cross marks and dumb bells. These were likely formed due to oriented etching (anisotropic etching). Referring to the literature on similar phenomena for Si [8] and III-V semiconductors [9], these patterns can be explained in terms of the fast etching rates for {110} planes illustrated schematically in Figure 4-42a. The direction <111> is preferred because it consists of a pair of Ga and As atoms. The dissolution of GaAs along the <111> directions will leave the surface cross marks or square marks which are shown as <110> directions on plane (001) which is atop view plane by microscopes, as shown in the optical images of Figure 4-39b and c, also

101

illustrated in Figure 4-42b and c. The dumb bell pattern may be a combination of <111> and <110> directions (Figure 4-42d).

4.2.2 X-ray photoelectron spectroscopy

X-ray photoelectron spectroscopy (XPS) was used to investigate the surface chemical states of GaAs after certain treatments for two purposes. One was to confirm the validity of the sample preparation procedures, as stated in the Chapter 3. The other was to understand how the surface composition changes after corrosion and to obtain information about corrosion products. Selective etching was found in previous work in our group from energy dispersive X-ray spectroscopy (EDX) results [3].

4.2.2.1 Cleaning procedure investigation

As-received GaAs wafers are not clean and not ready for experiments, since GaAs is reactive to oxygen in the air. Therefore, a regulated cleaning procedure is required to produce sample surfaces free of oxide and other susceptible surface states. Information on the cleaning procedures from optical microscopy and SEM is presented in Section 4.2.1.1 and 4.2.1.2. The microscopic results implicated that the 2.7 M NH_4OH solution is necessary to clean the corrosion products left after etching with the $H_2SO_4/H_2O_2/H_2O$ mixture. More detailed information was obtained from XPS.

A typical XPS spectrum of an as-received n-GaAs sample (1×10^{18} cm^{-3}) is given in Figure 4-43. It can be seen that the sample surfaces are very clean, as no XPS peaks other than Ga, As, C and O were found (C and O are inevitable during transferring the sample from testing solution to vacuum chamber). The C1s peak at 285.0 eV was always used for calibration. As suggested from an XPS handbook and the literature [10-13], the Ga2p (1120 eV), As3d (45 eV) are used for chemical state analysis because they are the strongest peaks for Ga and As respectively.

102

XPS spectra from the as-received, etched and etched + cleaned n-GaAs samples (1×10^{18} cm^{-3}) are shown in Figure 4-44. Chemical composition analysis results from Figure 4-44 are given in Table 4-4. The ratio of As/Ga changed from 1.6 to 3.1 and then 2.2 from the as-received sample to the etched and then to the etched + cleaned one. The high ratio (3.1) of As/Ga after etching might suggest that (1) Ga dissolves faster than As in the etchant; and / or (2) etched products of As leave the surface more slowly than those of Ga. The ratio of 2.2 after cleaning indicates that the dissolution of etching products of As or if the etching products from both Ga and As stay at the surface, the dissolution of the etching products of As is faster than that of Ga. In addition, the O/As ratio drops steadily (1.6 to 1.05 and then 0.67) from the as-received to the etched and the etched + cleaned, indicating the as-received sample surface is enriched with oxides and these are removed continuously in the etching and cleaning procedures. This means that both etching and cleaning are necessary to get rid of the oxides on the as-received samples.

More details can be obtained from the high-resolution XPS spectra focused on specific peaks, as shown in Figure 4-45 to Figure 4-48. For the As3d peak, only the as-received sample gives two peaks at the As-O position. From the literature [10, 12], the 44.5 eV peak is identified as As(III)-O, and the peak at 46 eV might be due to As(V)-O bonding because conversion from As(III)-O to As(V)-O is thermodynamically favorable (from the Gibbs free energy). It is interesting that the ratio of As-As to As-Ga bonds is constant despite etching and cleaning. For the Ga2p and Ga3d peaks, the ratio of Ga-O to Ga-As decreases. Combining quantification of the results above, it can be concluded that Ga oxides after etching are soluble in aqueous solution, although this process might not be extremely fast (Ga oxides also dissolve in ammonium solution).

4.2.2.2 Corrosion products identification

Chemical states after corrosion were also investigated by XPS. For n-GaAs, samples were potentiostatically polarized at 0.3 V vs. OCP for 1000 seconds and for p-GaAs samples were polarized at 0.2 V vs. OCP for the same time. Tests were performed under daylight conditions. The different polarization conditions for n- and p-GaAs were

103

chosen to make the corrosion charge comparable. Because corrosion occurs faster on p-GaAs, a smaller polarized potential region was selected relative to that applied to n-GaAs. Chemical analysis gave the composition at the surface and the atomic ratios of Ga to As were calculated and are shown in Table 4-5. The chemical composition data was analyzed from the Ga2p and As3d peaks because they are the strongest peaks for Ga and As respectively.

The Ga/As ratio after the cleaning procedure is around 0.42, lower than that of as-received sample (~0.60), indicating Ga selective chemical etching. The Ga/As ratios after corrosion under different conditions were not only less than 1, but also less than the as cleaned value. It can then be concluded that corrosion in the two solutions for the all GaAs samples is also Ga-selective. Secondly, the Ga/As ratio for n-GaAs after corrosion in NH_4OH solution (0.41) is higher than that in H_2SO_4 solution (0.34), which is also true for p-GaAs.

More details on the Ga and As distribution at the surface were obtained from the O1s peaks. From fitting, three peaks were deconvoluted. The peaks at 531.2 eV and 532.3 eV were attributed to O-Ga and O-As, respectively (Figure 4-49). According to the literature there is ~1.0 eV chemical shift between the O-Ga and O-As peaks [14]. The source of the broad peak at ~534 eV is not clear. The etched surface in H_3PO_4 reported by Kang et al [15] showed a peak at this energy value and it was identified as Ga-O-P, which is not applicable to our results. Contaminants could possibly account for the third peak. The area percentages of the O-Ga and O-As peaks are summarized in Table 4-6.

For both n-GaAs and p-GaAs, the O-Ga / O-As ratio is higher in NH_4OH solution than in H_2SO_4 solution, which is consistent with the Ga/As ratio from Table 4-5. A significantly smaller value of O-Ga / O-As (30/48) is found for p-GaAs in H_2SO_4 solution, which is the same trend as that in Table 4-4. The relatively smaller difference for n-GaAs, compared with p-GaAs is because the corrosion rate on p-GaAs is much faster and more corrosion products are expected, resulting in a more significant ratio difference.

104

4.2.3 Summary

Based on the results obtained from optical microscopy, SEM and XPS chemical composition analysis, the following can be concluded:

(1) The sample preparation procedure is necessary and valid to produce fresh GaAs surfaces. Oxides on as-received samples can be removed by the etching and cleaning.

(2) Electrochemical corrosion of GaAs may be Ga selective. The results from p-GaAs are more convincing because of faster corrosion.

105
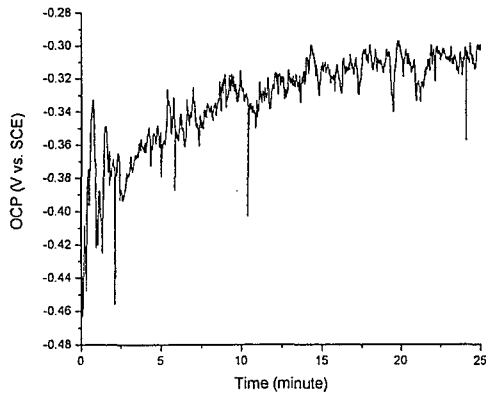
(a)
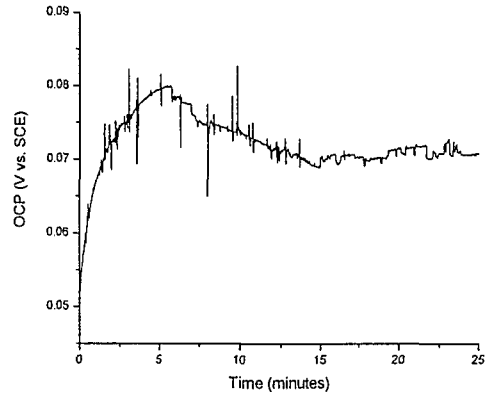
(b)
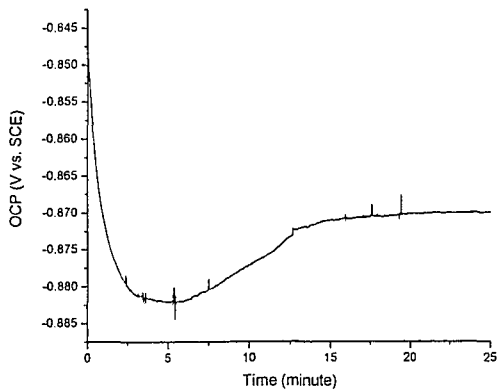
(c)
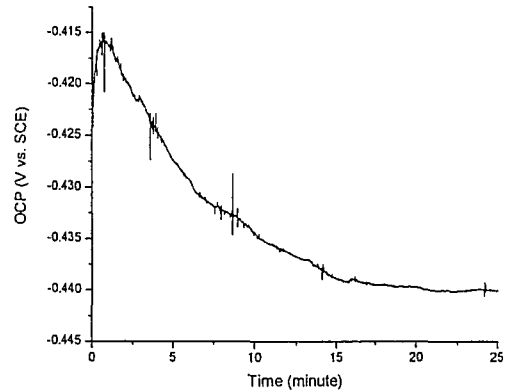
(d)

Figure 4-1 Open circuit potentials for GaAs (1×10^{18} cm^{-3}) in aqueous solutions just after immersion of the electrode into the solutions under daylight conditions. (a) and (c): n-type; (b) and (d): p-type. (a) and (b) were measured in 0.5 M H_2SO_4 and (c), (d) were measured in 2.7 M NH_4OH. Difference on OCP in the two solutions is 560 mV and 510 mV for n- and p-GaAs respectively.

106
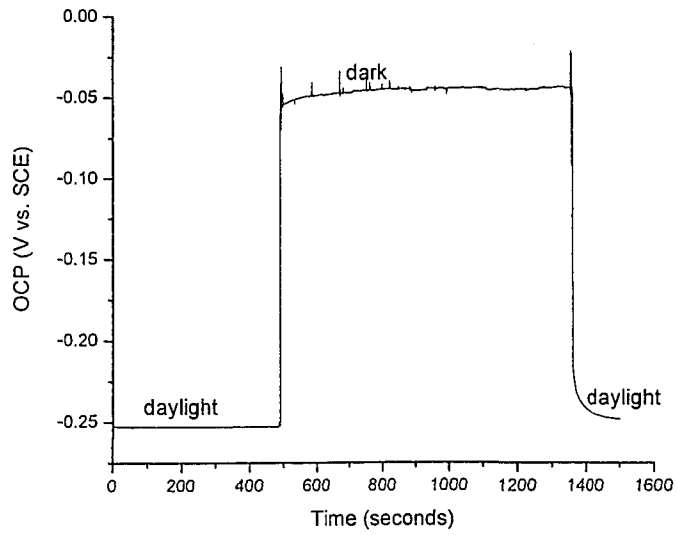
Figure 4-2 OCP changes by switching the dark and daylight conditions of n-GaAs (1×10^{18} cm^{-3}) in 0.5 M H_2SO_4 solution.
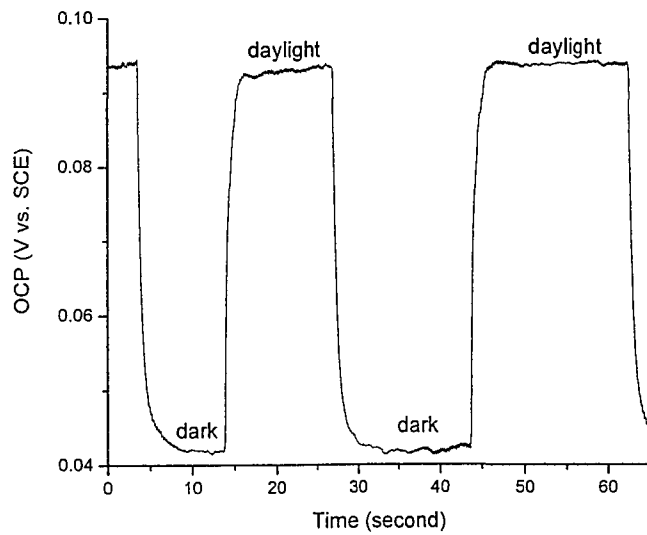
Figure 4-3 OCP changes by switching the dark and daylight conditions of p-GaAs (1×10^{18} cm^{-3}) in 0.5 M H_2SO_4 solution.

107

Table 4-1 OCPs for *n*- and *p*-GaAs at different doping levels in 0.5 M H$_2$SO$_4$ under both dark and daylight conditions.

GaAs doping levels (cm^{-3})		OCP in dark (mV)	OCP in daylight (mV)
n-type	1×10^{17}	-40	-250
	1×10^{18}	-45	-255
	2×10^{18}	-55	-272
	5×10^{18}	41	-110
p-type	1×10^{17}	83	145
	1×10^{18}	43	93
	4×10^{19}	15	57
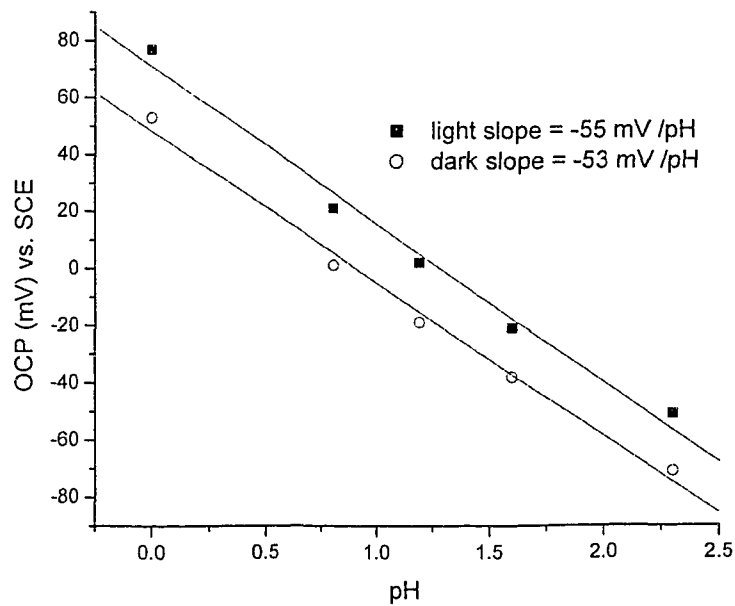
Figure 4-4 OCP tests for *p*-GaAs (1×10^{17} cm^{-3}) under different pH values of a mixture solution containing Na$_2$SO$_4$ and H$_2$SO$_4$. The ionic strength of the solutions was maintained approximately constant by changing the concentration of Na$_2$SO$_4$. Data marked with open circle were obtained from dark conditions and filled squares from daylight conditions.

108
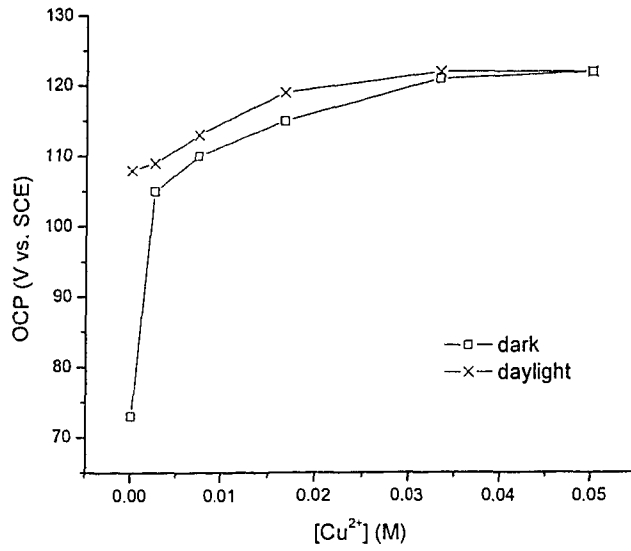
Figure 4-5 OCP change for p-GaAs (1×10^{17} cm^{-3}) as a function of Cu^{2+} concentration of in 0.5 M H$_2$SO$_4$. cross: daylight condition; square: dark condition.
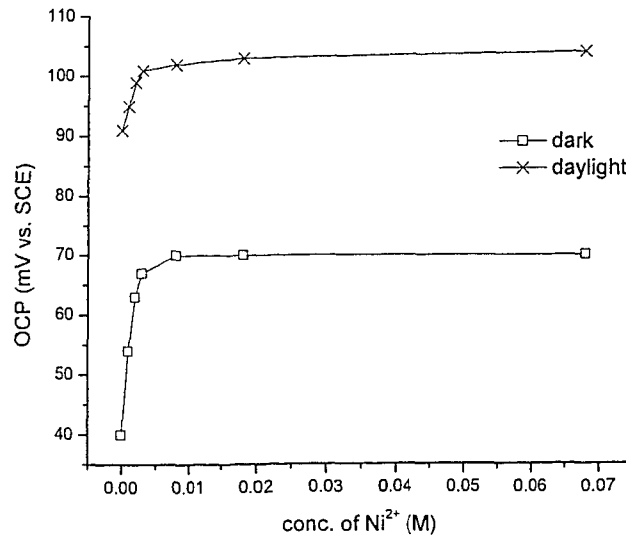
Figure 4-6 OCP change of p-GaAs (1×10^{17} cm^{-3}) by the concentration of Ni^{2+} in 0.5 M H$_2$SO$_4$. cross: daylight condition; square: dark condition.

109
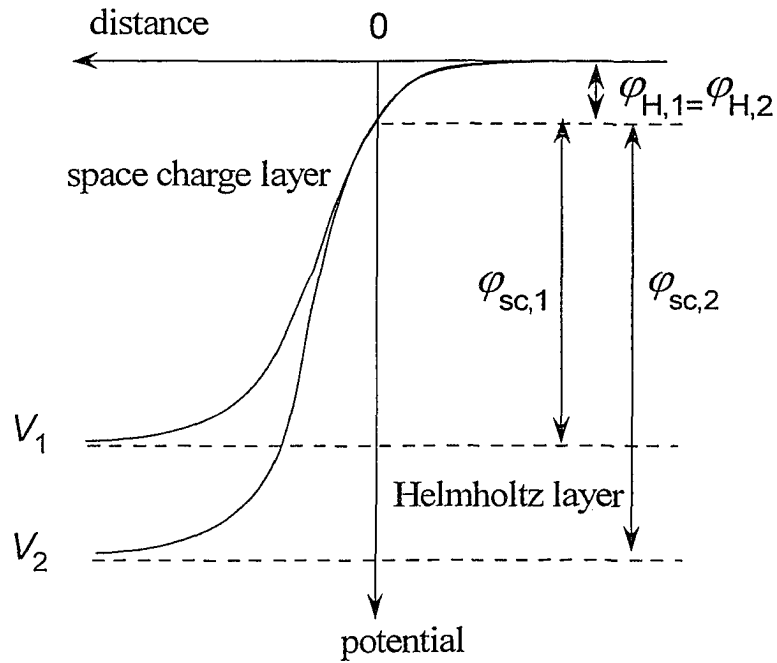
Figure 4-7 Illustration of the potential distribution of the limiting space charge layer control situation. The applied potential changes from V_1 to V_2, causing the change of potential drop in the space charge region from $\varphi_{SC,1}$ to $\varphi_{SC,2}$, and the potential drop in Helmholtz layer remains unchanged.
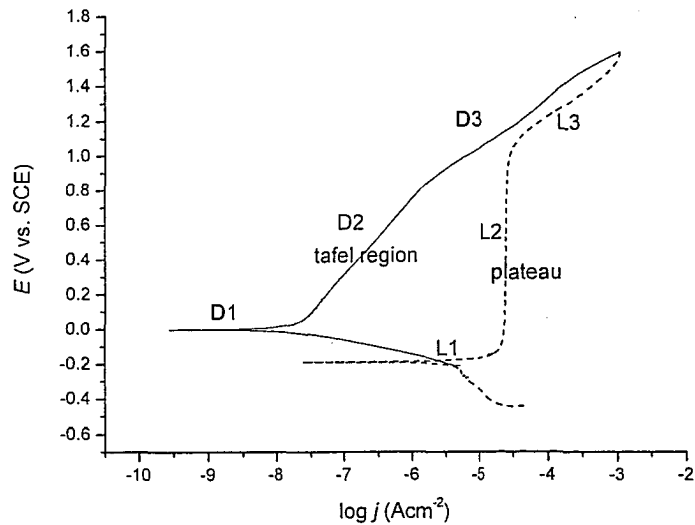
Figure 4-8 Polarization curves of n-GaAs (1×10^{18} cm^{-3}) in 0.5 M H_2SO_4 under dark (solid line) and daylight (dot line) conditions. Three regions are identified for the two curves and named as D1, D2 and D3 for dark conditions and L1, L2 and L3 for illumination conditions respectively.

110
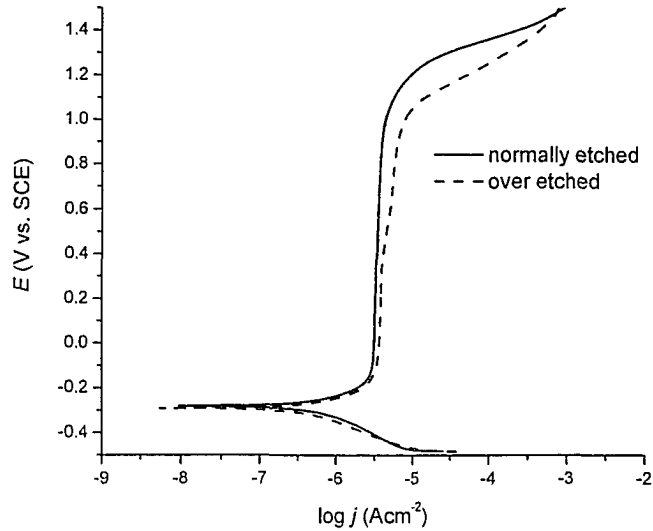
Figure 4-9 Polarization curves for n-GaAs (1×10^{18} cm^{-3}) in 0.5 M H_2SO_4 under daylight conditions, showing the influence of etching time. Dotted line is from a sample over etched (~ 1 min etching) and solid time is from a sample normally etched.
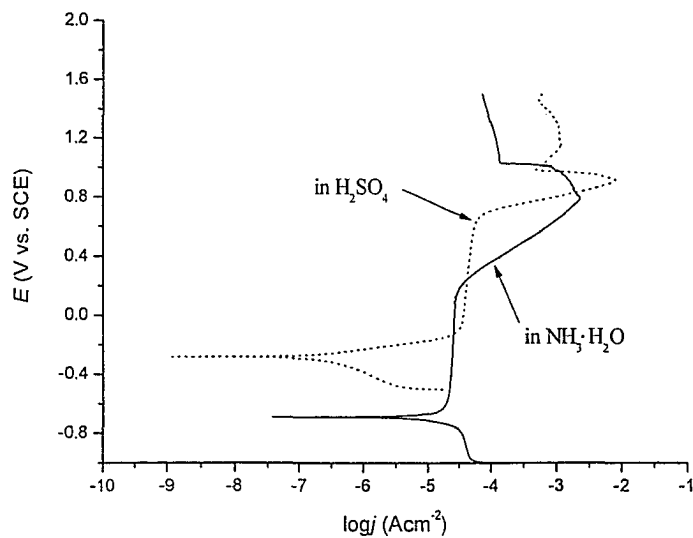
Figure 4-10 Polarization curves for n-GaAs (2×10^{18} cm^{-3}) in the two solutions (0.5 M H_2SO_4 and 2.7 M NH_4OH) in daylight conditions. Difference in OCP: ~400 mV (-290+690 mV) and difference in breakdown potential: ~440 mV (680-140 mV).

111
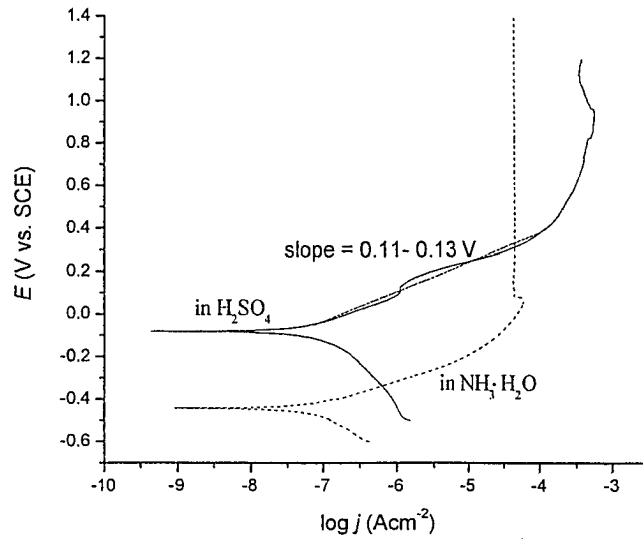
Figure 4-11 Anodic polarization curves for p-GaAs (1×10^{18} cm^{-3}) in the two solutions (0.5 M H$_2$SO$_4$, solid line) and 2.7 M NH$_4$OH, dashed line) in daylight conditions.
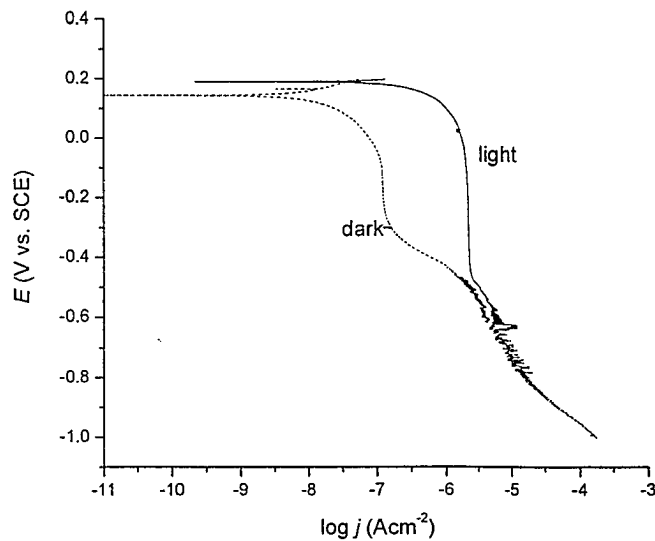
Figure 4-12 Cathodic polarization curves for p-GaAs (1×10^{18} cm^{-3}) in 0.5 M H$_2$SO$_4$ solution under dark (dashed line) and daylight (solid line) conditions.

112
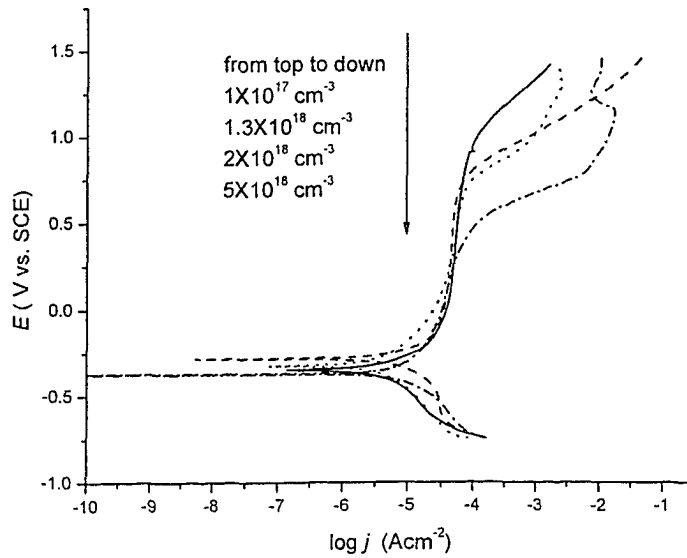
Figure 4-13 Polarization curves dependence on the doping levels. Doping levels 1×10^{17}, 1.3×10^{18}, 2×10^{18} and 5×10^{18} cm^{-3}are for the curves from top to bottom.
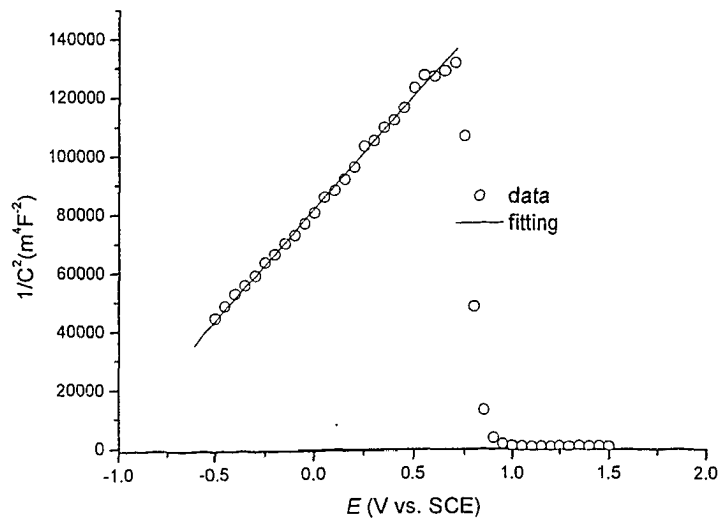
Figure 4-14 Mott-Schottky plots for n-GaAs (1×10^{18} cm^{-3}) in 0.5 M H$_2$SO$_4$ under dark conditions. V_{fb} = -1.05V.

113
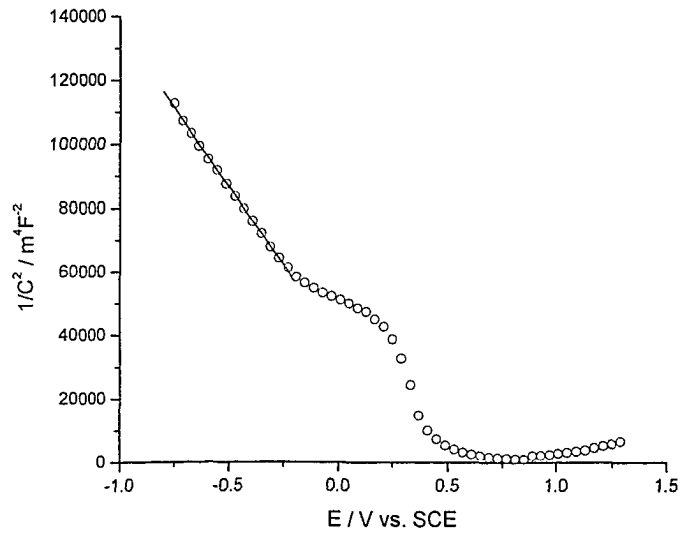
Figure 4-15 Mott-Schottky plots for p-GaAs (1×10^{18} cm^{-3}) in 0.5 M H_2SO_4 under dark conditions. V_{fb} = 0.38V.
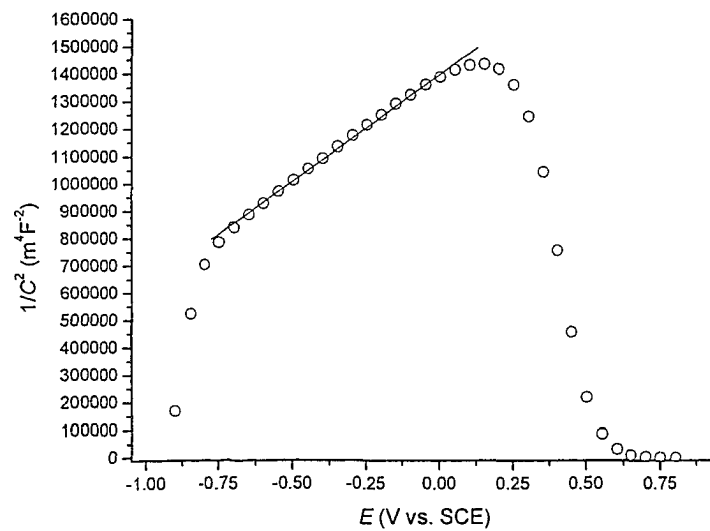
Figure 4-16 Mott-Schottky plots for n-GaAs (1×10^{18} cm^{-3}) in 2.7 M NH_4OH under dark conditions. V_{fb} = -1.76 V.

114
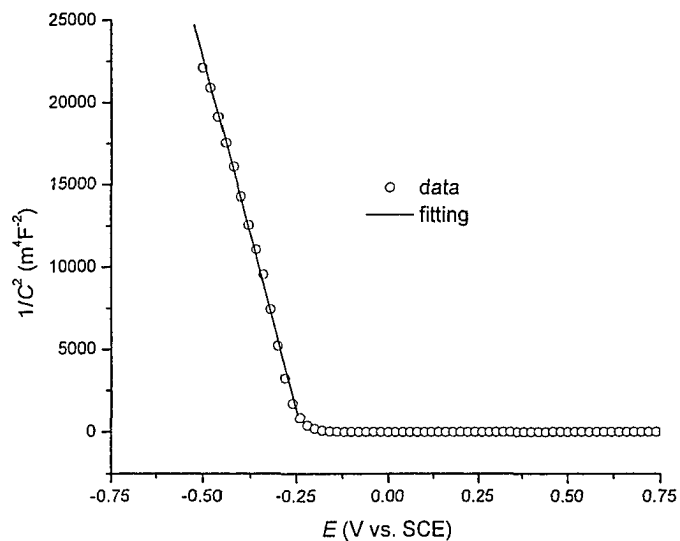
Figure 4-17 Mott-Schottky plots for p-GaAs (1×10^{18} cm^{-3}) in 2.7 M NH$_4$OH under dark conditions. $V_{fb} = -0.25$ V.
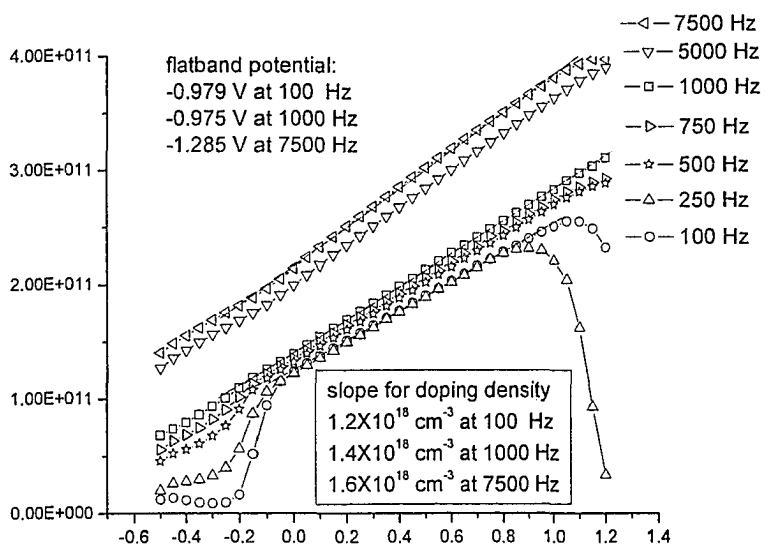
Figure 4-18 Mott-Schottky plots for n-GaAs (1×10^{18} cm^{-3}) in 0.5 M H$_2$SO$_4$ solution at different frequencies under dark conditions. Obtained flatband potentials and doping level from the slopes are shown.

115
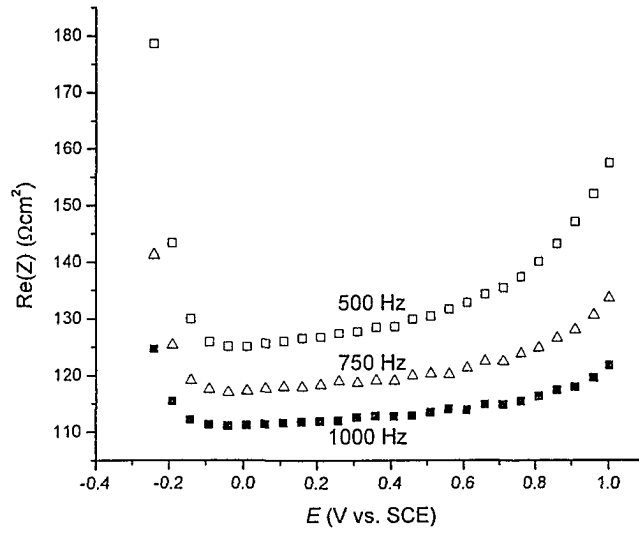
Figure 4-19 Real part of Mott-Schottky measurements for n-GaAs (1×10^{18} cm^{-3}) in 0.5 M H$_2$SO$_4$ solution at different frequencies under dark conditions.
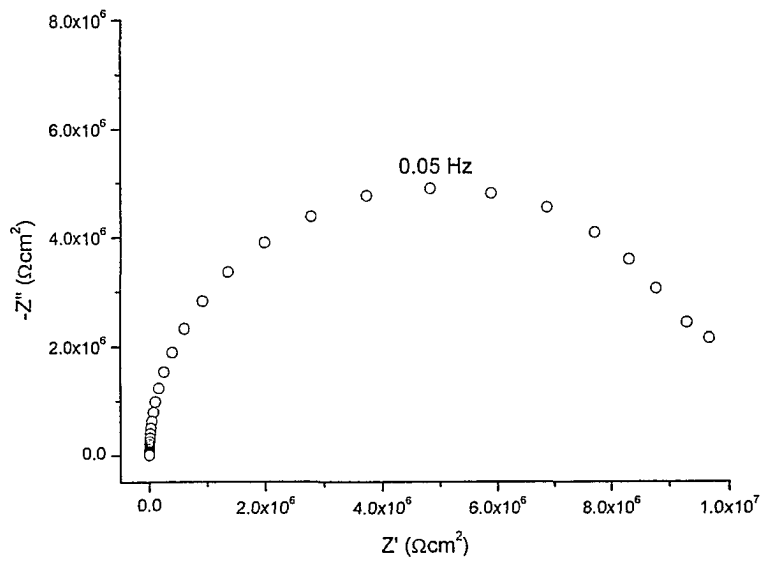
Figure 4-20 Impedance spectra for n-GaAs in 0.5 M H$_2$SO$_4$ (1×10^{18} cm^{-3}) under dark conditions at 50 mV.

116
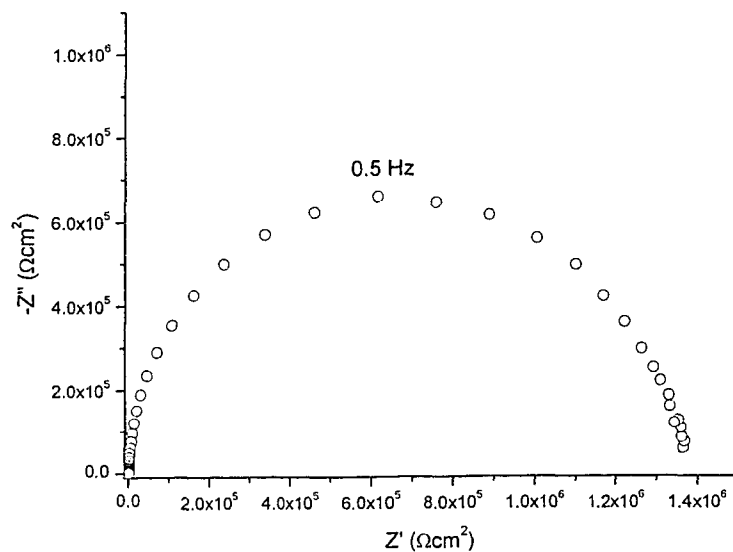
Figure 4-21 Impedance spectra for *n*-GaAs (1×10^{18} cm^{-3}) in 0.5 M H$_2$SO$_4$ under dark conditions at 500 mV.
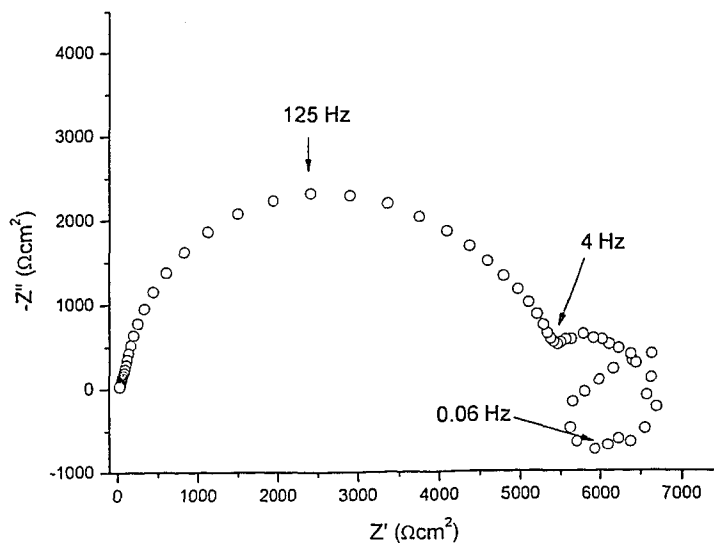
Figure 4-22 Impedance spectra for *n*-GaAs in 0.5 M H$_2$SO$_4$ (1×10^{18} cm^{-3}) under dark conditions at 1150 mV.

117
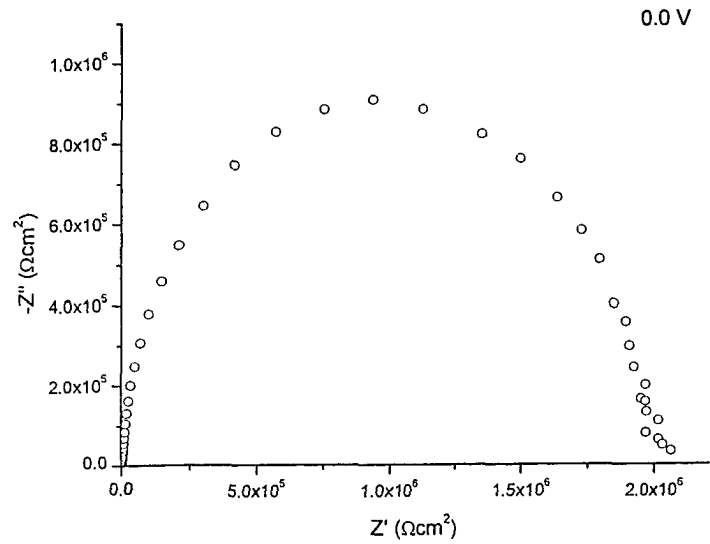
Figure 4-23 Impedance data for n-GaAs (1×10^{18} cm^{-3}) in 2.7 M NH$_4$OH under dark conditions at 0 mV.
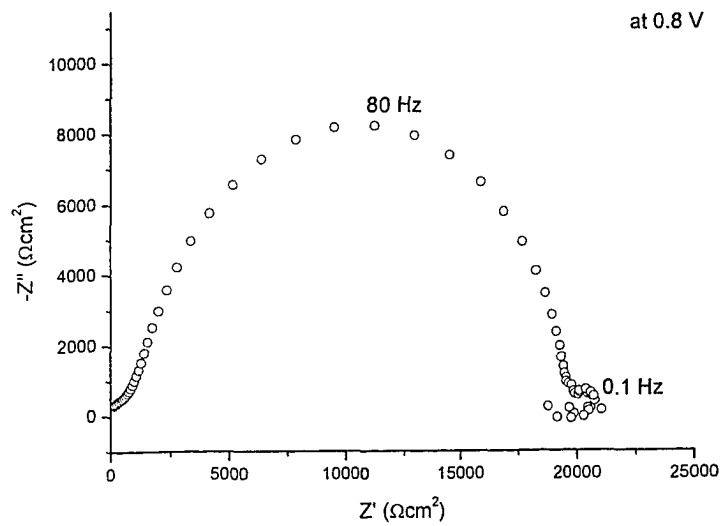
Figure 4-24 Impedance data for n-GaAs (1×10^{18} cm^{-3}) in 2.7 M NH$_4$OH under dark conditions at 800 mV.

118
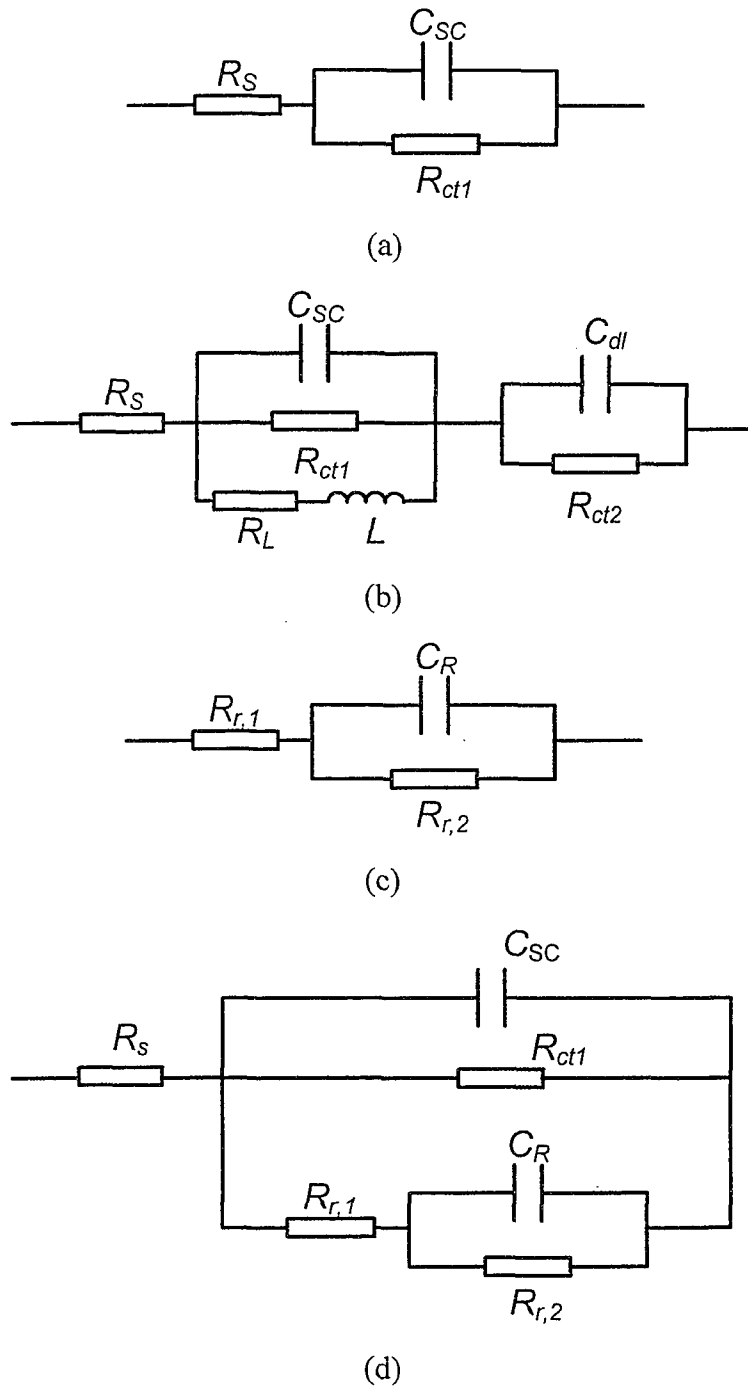
Figure 4-25 Equivalent circuits to fit the impedance spectra. (a) The potential region before breakdown; (b) after breakdown; (c) model proposed in literature [7] to describe the recombination process [6]; (d) the L1 region with recombination.

119
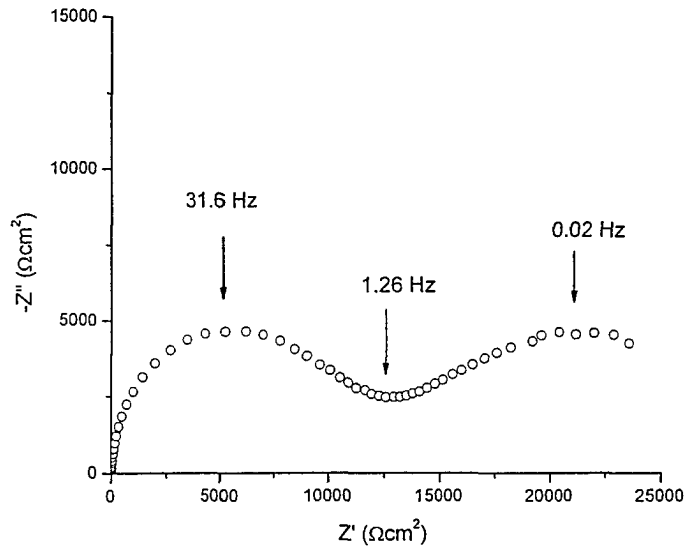
Figure 4-26 Impedance spectra of *n*-GaAs in 0.5 M H_2SO_4 (1×10^{18} cm^{-3}) under daylight conditions at - 200 mV.
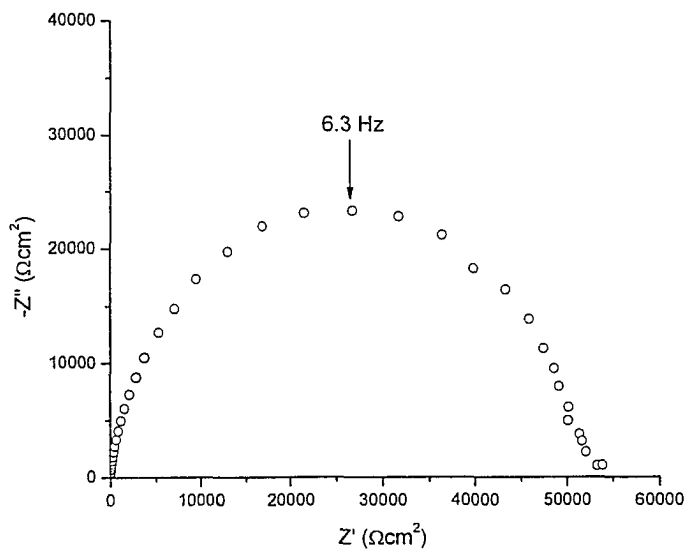
Figure 4-27 Impedance spectra of *n*-GaAs in 0.5 M H_2SO_4 (1×10^{18} cm^{-3}) under daylight conditions at 300 mV.

120
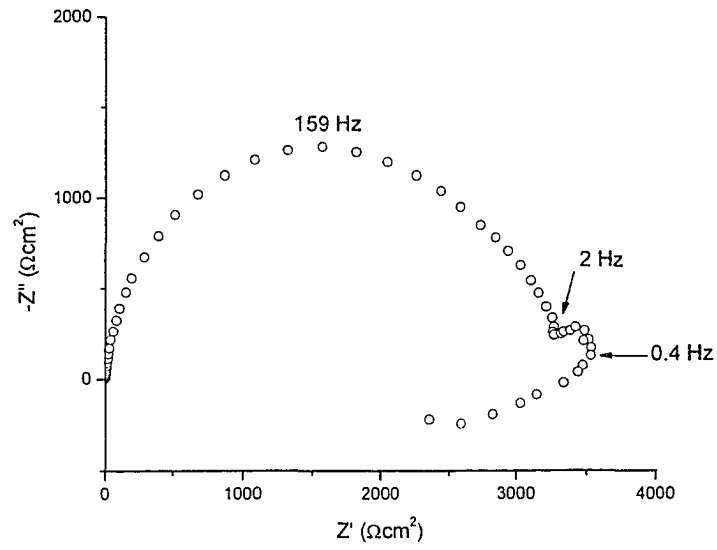
Figure 4-28 Impedance spectra of n-GaAs in 0.5 M H_2SO_4 (1×10^{18} cm^{-3}) under daylight conditions at 1000 mV.

Table 4-2 Data fit using $R_s(R_{ct1}C_{sc})$ to the experimental impedance data for n-GaAs in 0.5 M H_2SO_4 (1×10^{18} cm^{-3}) under dark conditions in Figure 4-20 and Figure 4-22.

E (V vs. SCE)	R_{ct1} (Ωcm^2)	C_{sc} (Fcm^{-2})	$1/C_{sc}^2$ (μF^{-2}cm^4)
-0.05	9.76E5	3.41E-7	8.58
-0.0351	1.48E6	3.43E-7	8.50
0	4.01E6	3.33E-7	9.01
0.05	9.94E6	3.29E-7	9.22
0.1	1.13E7	3.25E-7	9.47
0.15	8.10E6	3.08E-7	10.52
0.2	5.52E6	2.99E-7	11.20
0.25	4.57E6	2.90E-7	11.93
0.3	3.72E6	2.84E-7	12.39
0.35	2.96E6	2.77E-7	13.03
0.4	2.29E6	2.72E-7	13.57
0.45	1.75E6	2.66E-7	14.14
0.5	1.36E6	2.56E-7	15.25
0.55	1.06E6	2.54E-7	15.43
0.6	8.20E5	2.52E-7	15.69
0.65	6.48E5	2.48E-7	16.21
0.7	5.30E5	2.38E-7	17.56
0.75	4.29E5	2.34E-7	18.21
0.85	2.73E5	2.29E-7	19.00
0.95	1.36E5	2.33E-7	18.48

122
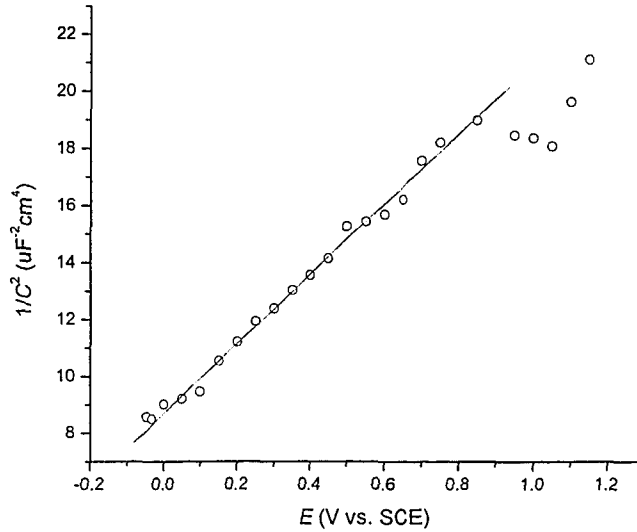
Figure 4-29 Plot of $1/C_{sc}^2$ vs. applied potential using the data from fit results for the equivalent circuit of Figure 4-25a to the series in Figure 4-20 and Figure 4-22. This plot gives a flatband potential of – 0.71 V vs. SCE and a doping density of 1.25×10^{18} cm^{-3}.
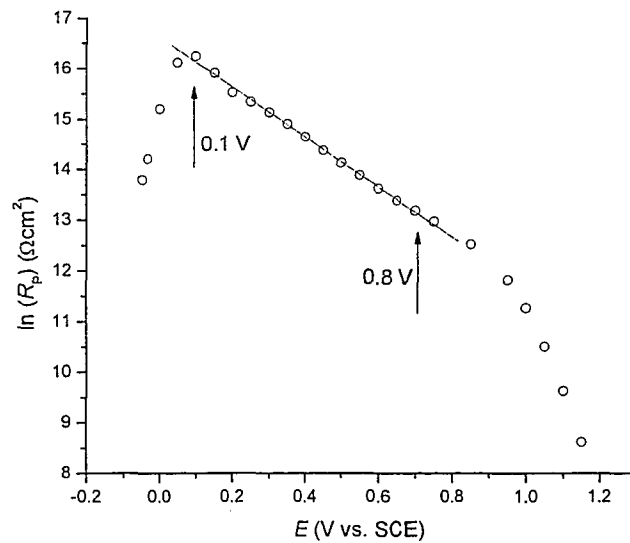
Figure 4-30 plot of $\ln(R_{ct})$ vs. applied potential using the data from fit results for the equivalent circuit of Figure 4-25a to the series in Figure 4-20 and Figure 4-22. Between potentials of 0.1 to 0.8 V, it has a linear shape.

123

Table 4-3 Fit to the data using $R_s(R_{ct1}C_{sc})$ for the experimental impedance data for n-GaAs in 0.5 M H_2SO_4 (1×10^{18} cm^{-3}) under dark conditions in Figure 4-27 and Figure 4-28.

E (V vs. SCE)	R_{ct1} (Ωcm^2)	C_{sc} (Fcm^{-2})	$1/C_{sc}^2$ (μF^{-2}cm^4)
-0.2	6.10E3	7.61E-7	1.73
-0.15	1.74E4	7.30E-7	1.88
-0.1	4.96E4	7.15E-7	1.96
-0.05	1.69E5	6.88E-7	2.11
0.0	4.701E5	6.66E-7	2.26
0.05	6.88E5	6.49E-7	2.37
0.10	7.15E5	6.31E-7	2.51
0.15	6.94E5	6.12E-7	2.67
0.20	6.21E5	5.97E-7	2.81
0.25	6.32E5	5.83E-7	2.94
0.30	6.32E5	5.67E-7	3.11
0.35	6.71E5	5.58E-7	3.21
0.40	6.77E5	5.46E-7	3.35
0.50	6.45E5	5.27E-7	3.60
0.60	6.12E5	5.08E-7	3.88
0.70	4.93E5	4.93E-7	4.12
0.80	3.11E5	4.78E-7	4.37
0.90	1.52E5	4.68E-7	4.58
1.0	7.01E4	4.59E-7	4.74
1.10	2.87E4	4.60E-7	4.72
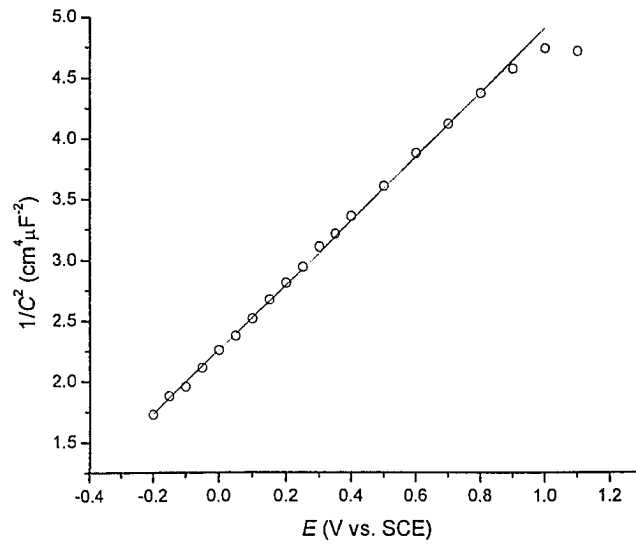
124

Figure 4-31 Plot if $1/C_{sc}^2$ vs. applied potential using the data from fit results with the equivalent circuit in Figure 4-25a to the series in Figure 4-27 and Figure 4-28. This plot gives a flatband potential of –0.85 V vs. SCE.
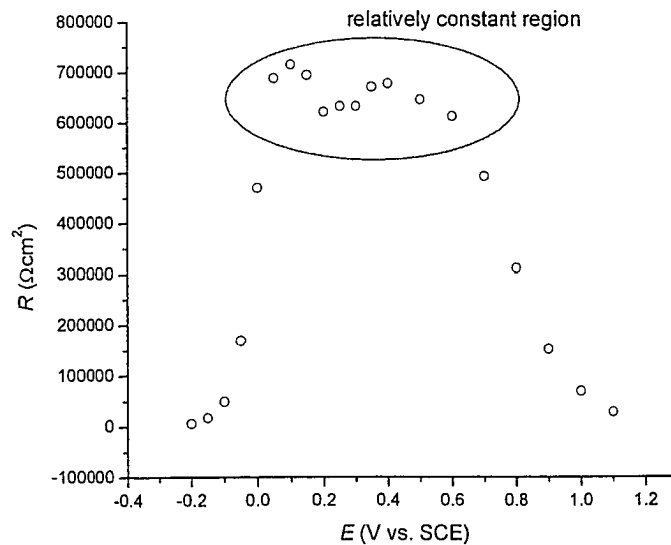
Figure 4-32 Plot of R_{ct1} vs. applied potential using the data from fit results with the equivalent circuit in Figure 4-25a to the series in Figure 4-27 and Figure 4-28. Between potential of 0.1 to 0.7 V, R_{ct1} is relative constant.
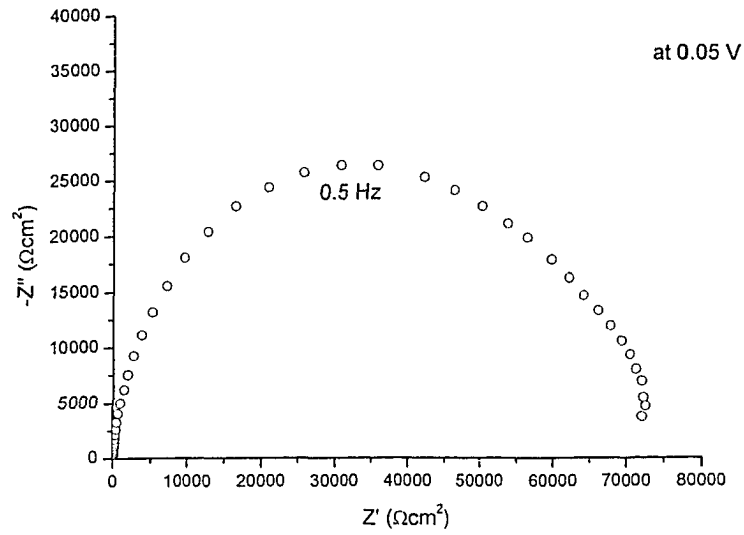
Figure 4-33 Impedance data for p-GaAs (1×10^{18} cm^{-3}) in 0.5 M H$_2$SO$_4$ solution under daylight conditions at 0 mV.
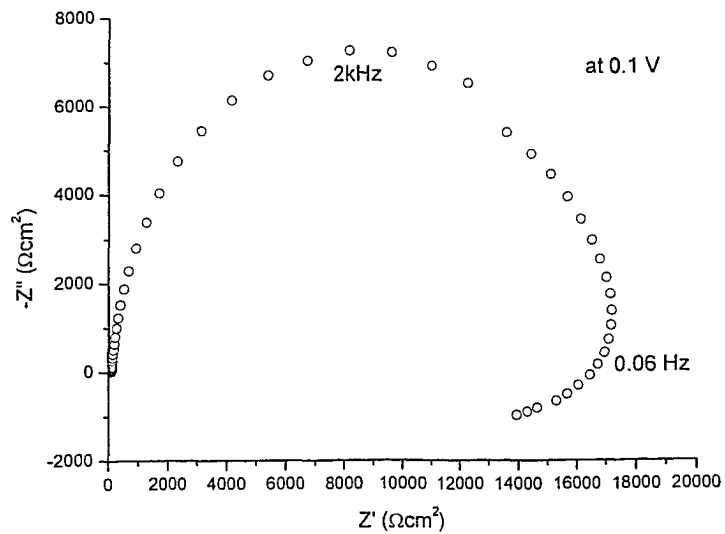
Figure 4-34 Impedance data for p-GaAs (1×10^{18} cm^{-3}) in 0.5 M H$_2$SO$_4$ solution under daylight conditions at 100 mV.

126
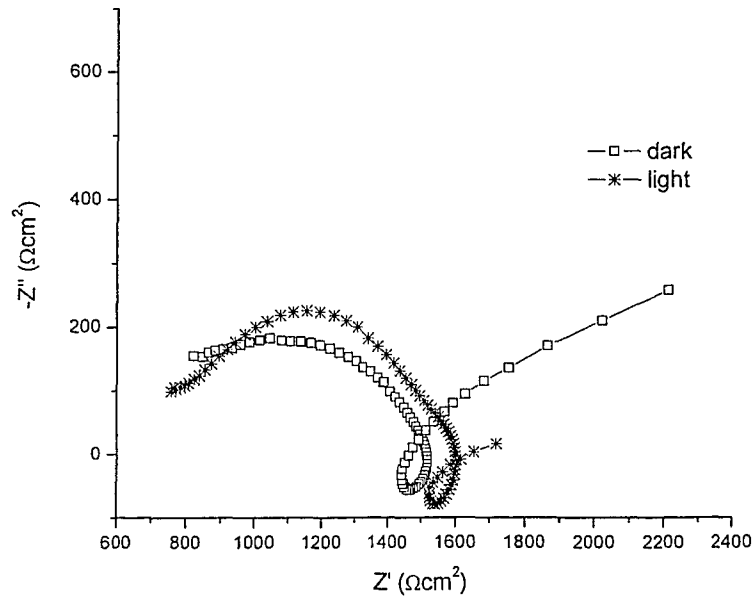
Figure 4-35 Impedance data for *p*-GaAs (1×10^{18} cm^{-3}) in 0.5 M H$_2$SO$_4$ solution under dark and daylight conditions at 200 mV vs. OCP. Δ: under illumination conditions; □: under dark conditions.
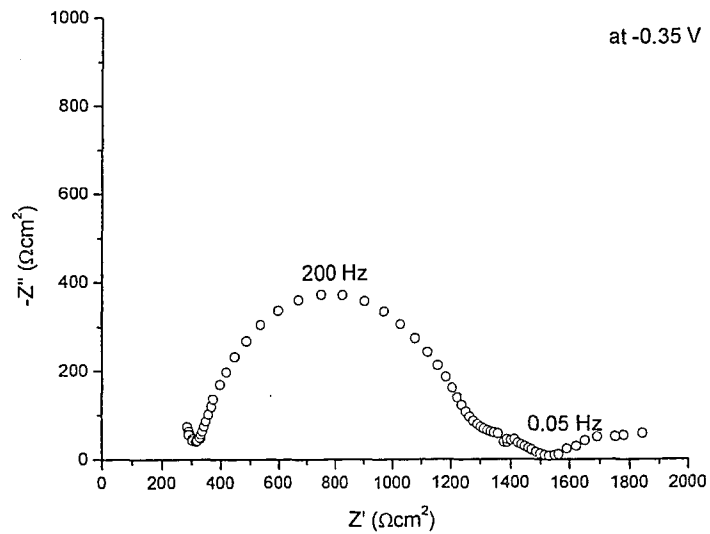
Figure 4-36 Impedance data for *p*-GaAs (1×10^{18} cm^{-3}) in 2.7 M NH$_4$OH solution under daylight conditions at -350 mV.

127
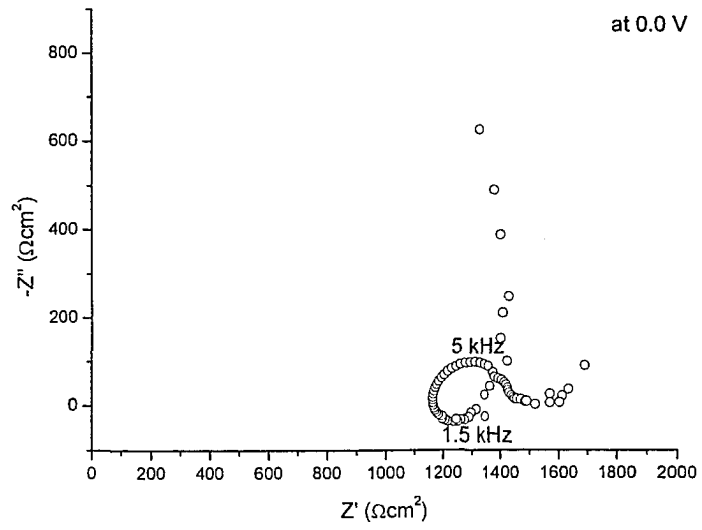
Figure 4-37 Impedance data for p-GaAs (1×10^{18} cm^{-3}) in 2.7 M NH$_4$OH solution under daylight conditions at 0 mV.

(a)

(b)

129

(c)

(d)

130
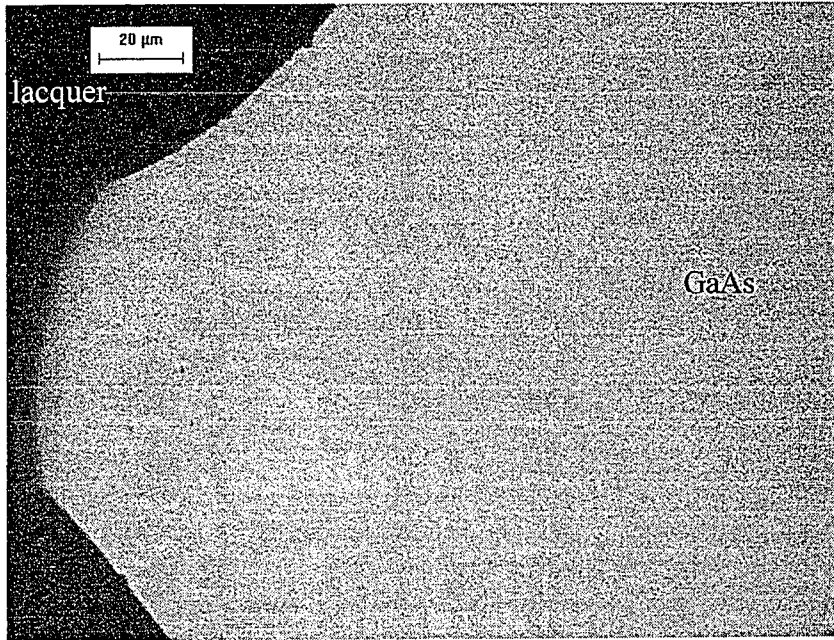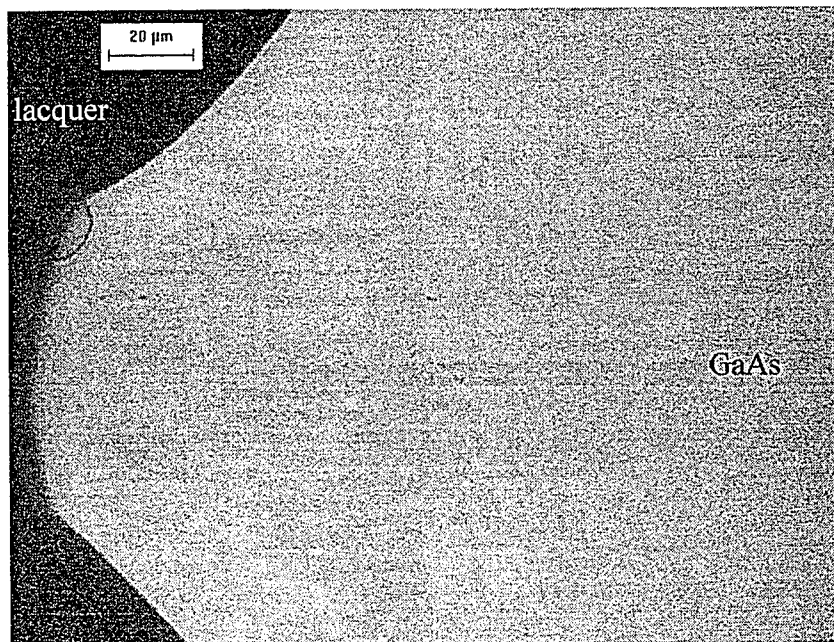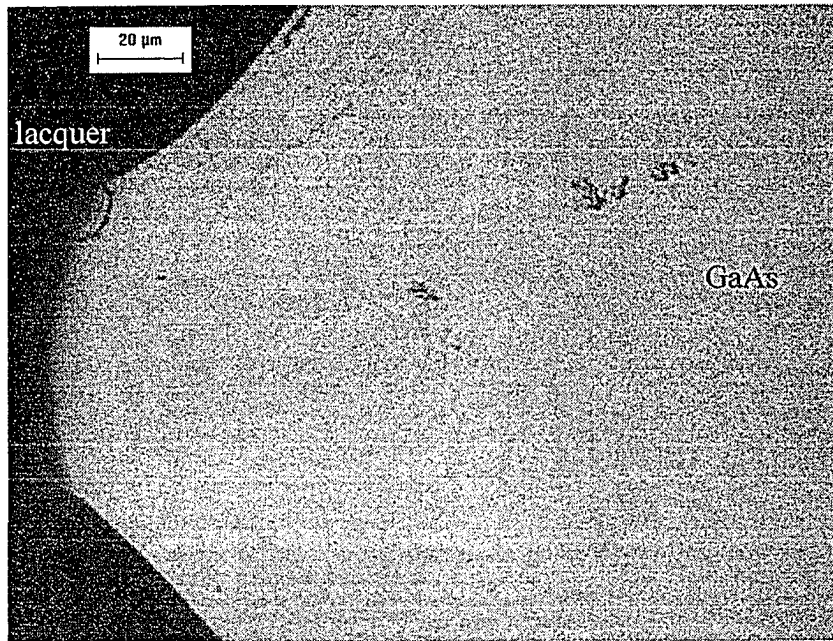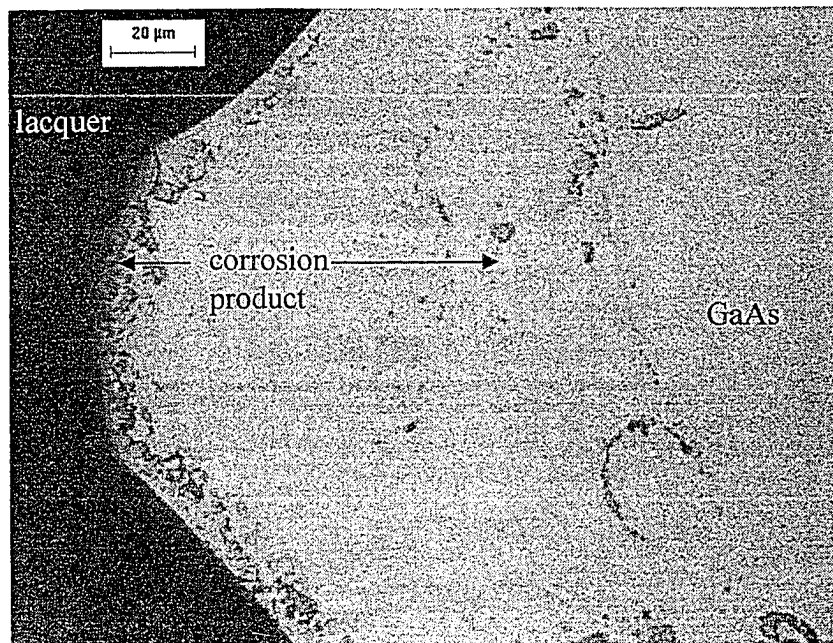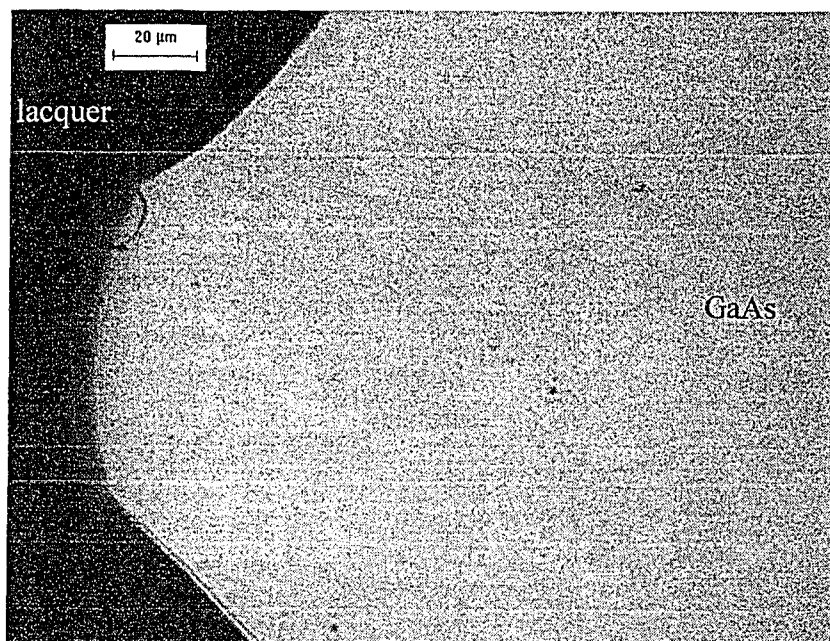
(e)

Figure 4-38 Optical microscope images for p-GaAs (1×10^{18} cm^{-3}) with the following sequential treatments. These images were taken at same position of one sample for best comparison after a sequential chemical and electrochemical treatments. a) as-received; b) after chemically etching in $H_2SO_4/H_2O_2/H_2O$ mixture for 20 seconds; c) after cleaning in NH_4OH solution for 30 seconds; d) after potential sweeping corrosion in H_2SO_4 from -0.2 V to 0.5 V at a scan rate of 5 mV/s; e) after immersion in 2.7 M NH_4OH solution for 30 seconds.

131

(a)

(b)

(c)

(d)
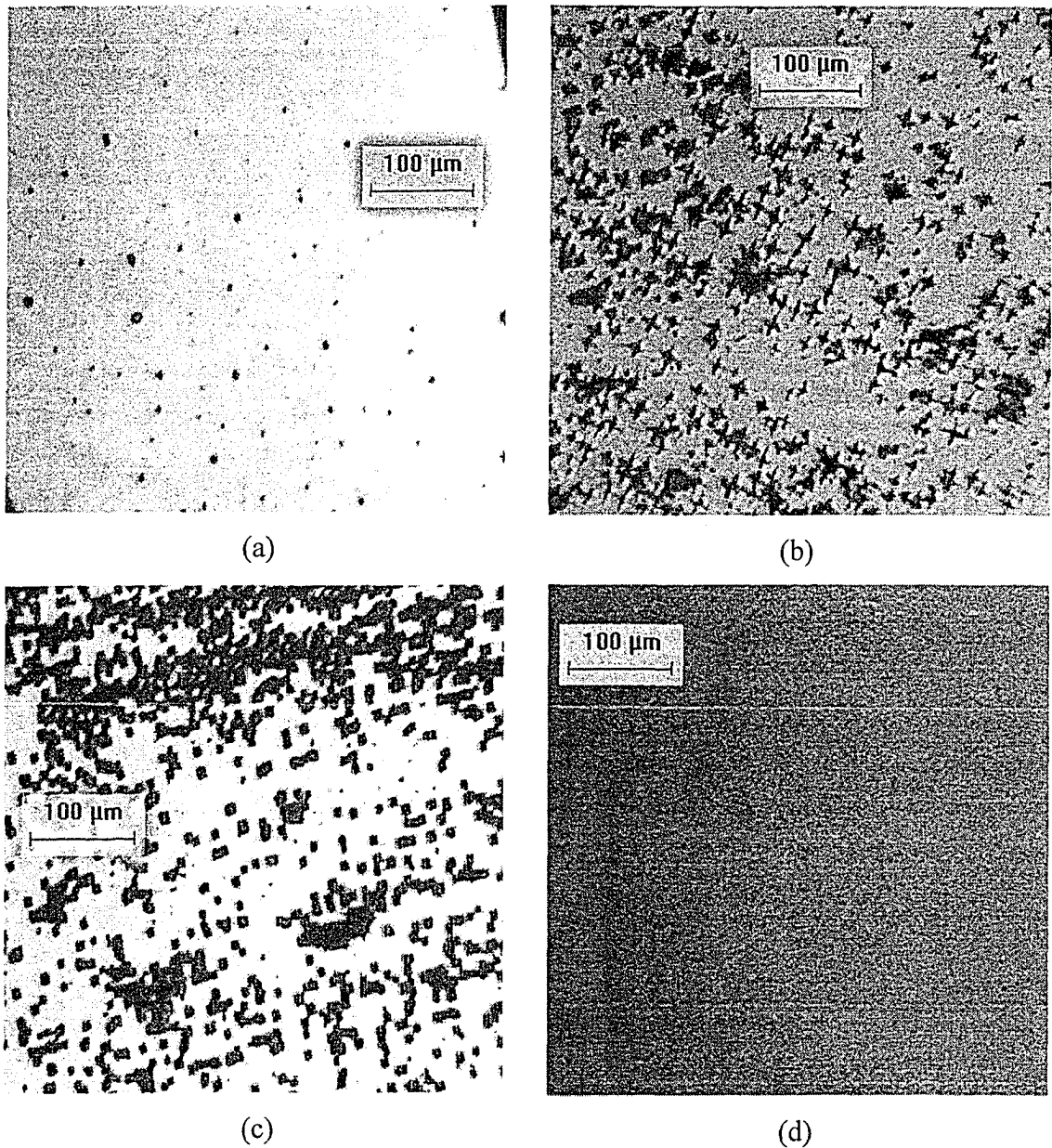
Figure 4-39 Optical images of n-GaAs at different doping levels for the same polarization conditions (2 cycles from -0.75 V to 1.5 V) in 0.5 M H_2SO_4 solution. Doping levels for these images are (a) 1×10^{17} cm^{-3}, (b) 1.3×10^{18} cm^{-3}, (c) 2×10^{18} cm^{-3} and (d) 5×10^{18} cm^{-3}.

132

(a)

(b)

(c)

(d)

(e)

(f)
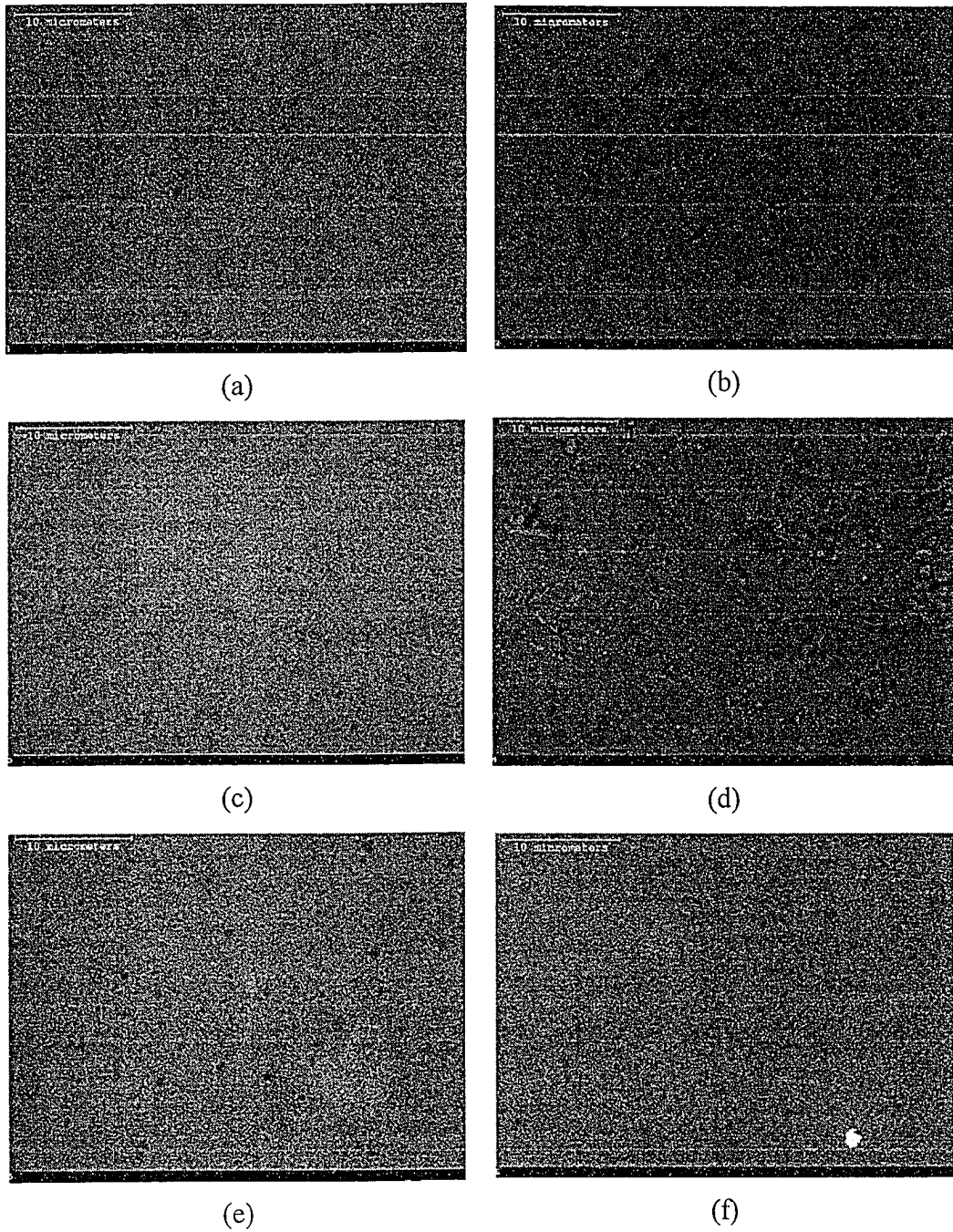
Figure 4-40 SEM SE images for n-GaAs (1×10^{18} cm^{-3}). Images from (a)-(d) were acquired from sequential treatments on one sample. (a) As-received sample; (b) after the etching procedure; (c) after the cleaning procedure; (d) after corrosion in H_2SO_4 by two potential sweeping polarizations from OCP to 1.2 V under light conditions, e) after immersion in 2.7 M NH_4OH solution for 5 minutes. Image (f) is from another sample after the normal etching and cleaning procedures and then corrosion in 2.7 M NH_4OH solution by two potential sweeping polarizations from OCP to 1.0 V .

133
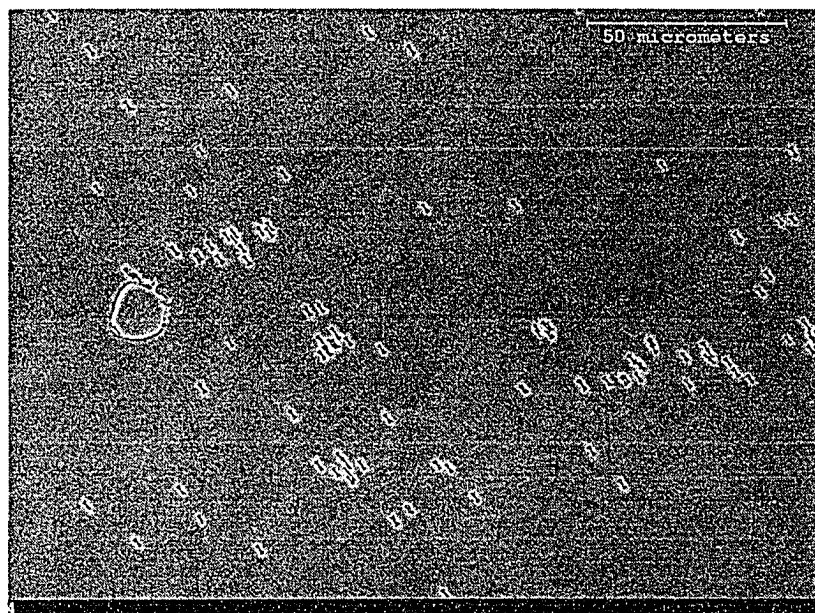
(a)
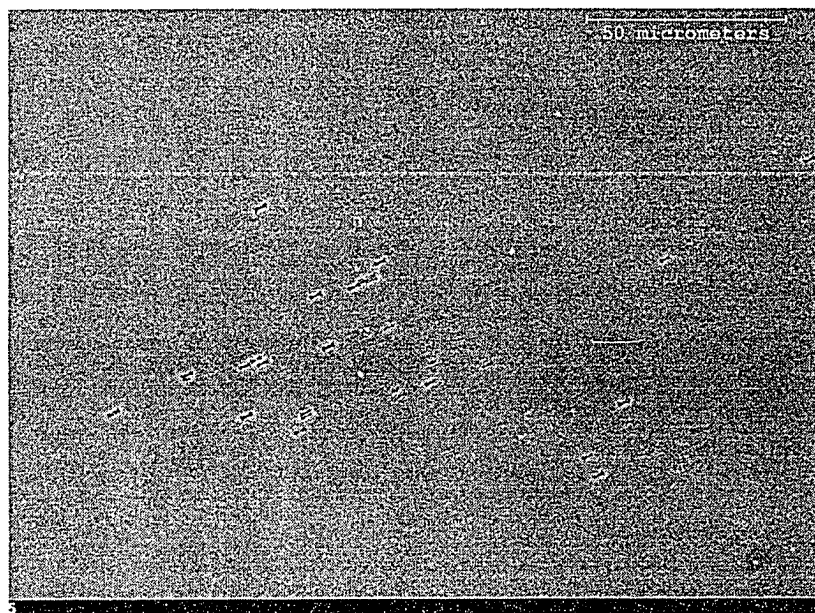
(b)

Figure 4-41 SEM SE images for n-GaAs (5×10^{18} cm^{-3}) after potential sweeping corrosion from OCP to 1.0 V in 0.5 M H_2SO_4 solution under daylight conditions. (a) Just after the corrosion; (b) after sample in (a) was immersed in 2.7 M NH_4OH solution for 5 minutes.

134

(a) schematic directions

(b) square

(c) cross mark

(d) dumb bell
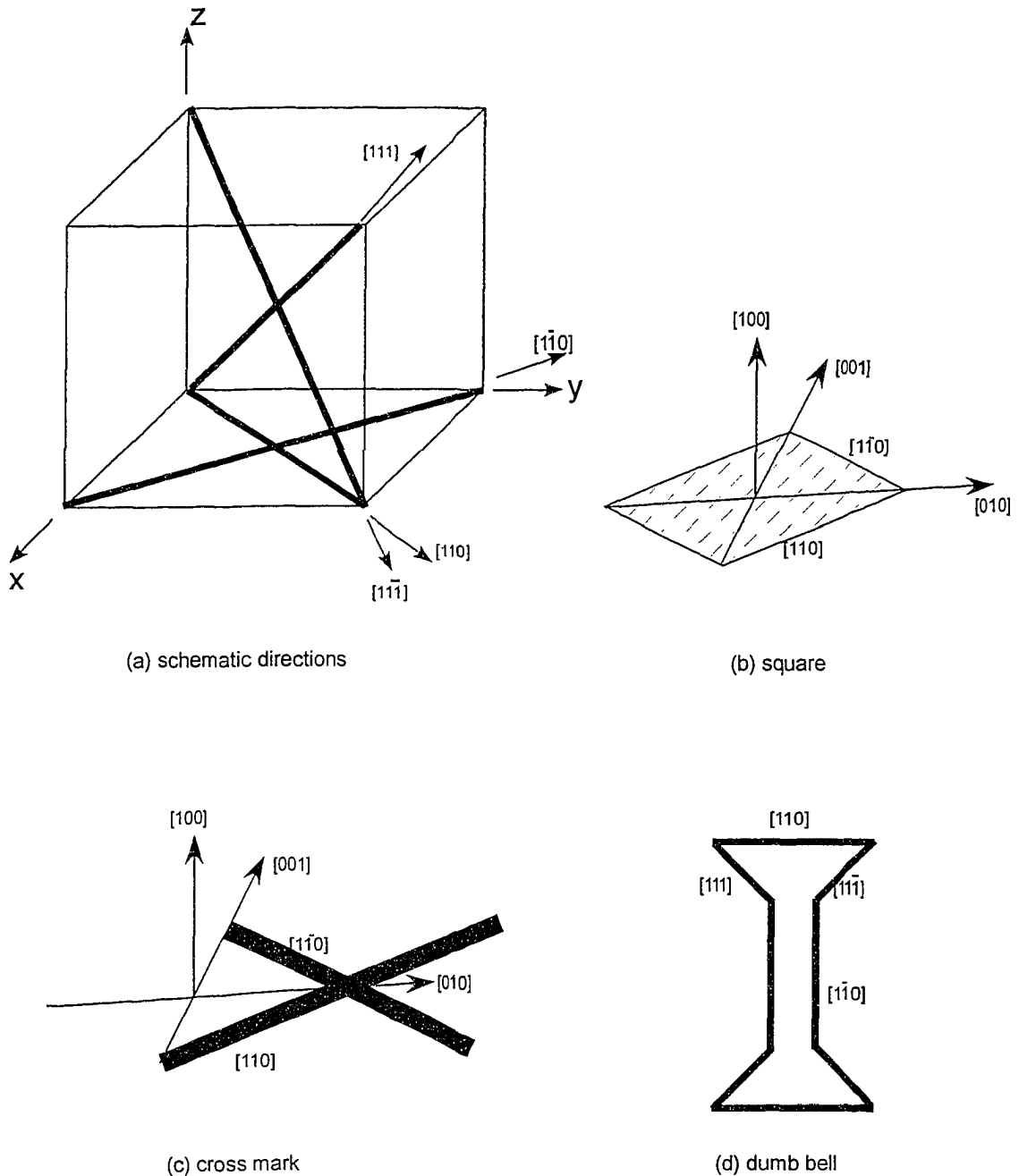
Figure 4-42 Illustration for the anisotropic etching of GaAs. In (a), the projected relationship between the <111> and <110> directions on plane (001) are shown. Because the top view in the SEM or optical microscope is the direction of [001], the etched directions viewed are the corresponding projected directions on plane (001). From the zinc-blende structure as shown in Figure 2-1, the direction <111> consists of a pair of Ga and As atoms, which is the preferred decomposition direction. These will result in a square pattern (b) or a cross pattern (c) after etching, as shown in Figure 4-39b and c. The dumb bell pattern is the combination of the <111> directions and the <110> directions (d). More detail is given in the text.

135
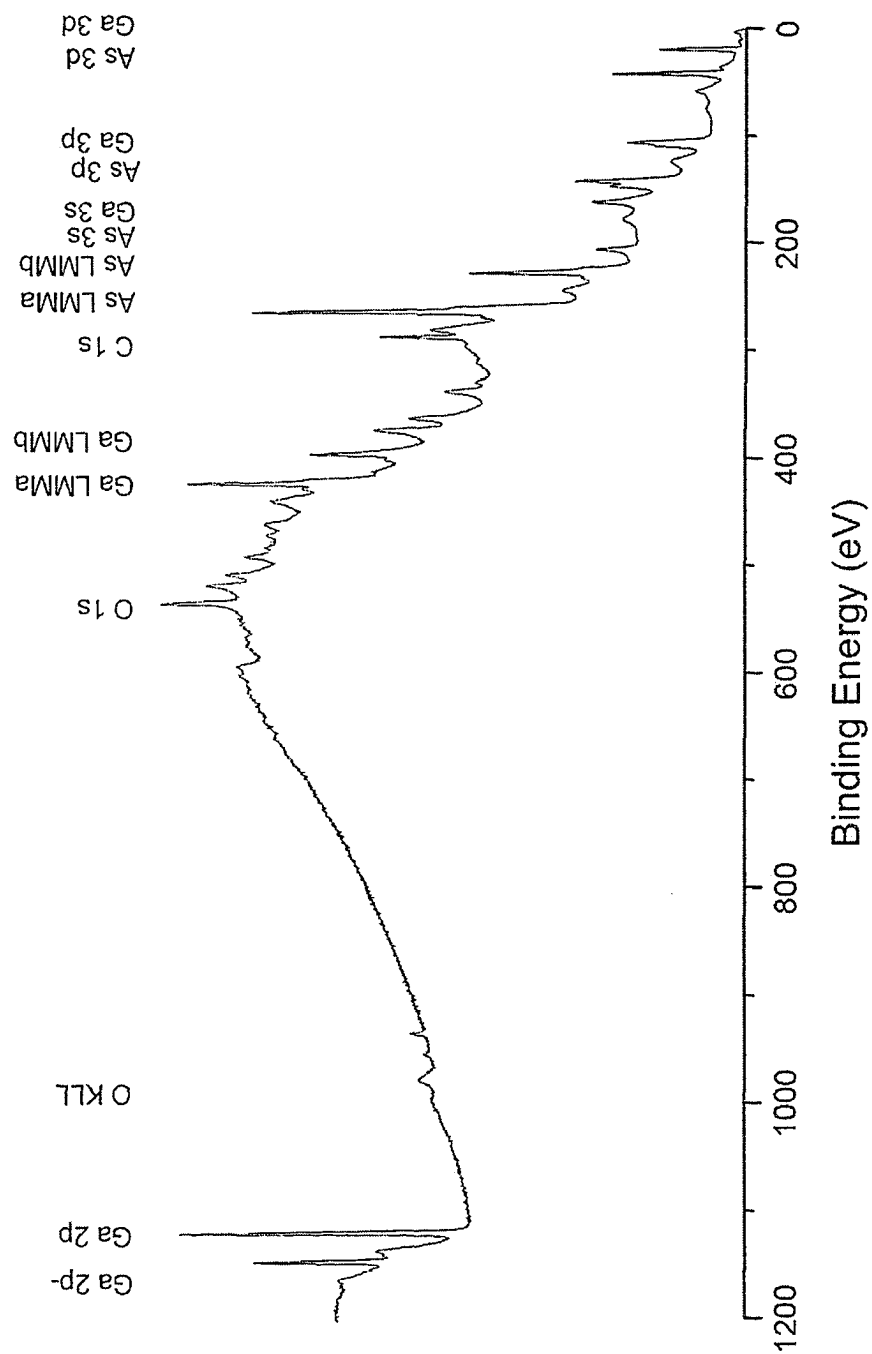
Figure 4-43 A typical XPS survey spectrum for GaAs (*n*-type, 1×10^{18} cm^{-3}, as-received sample). Peaks from Ga, As, C and O are identified.

136
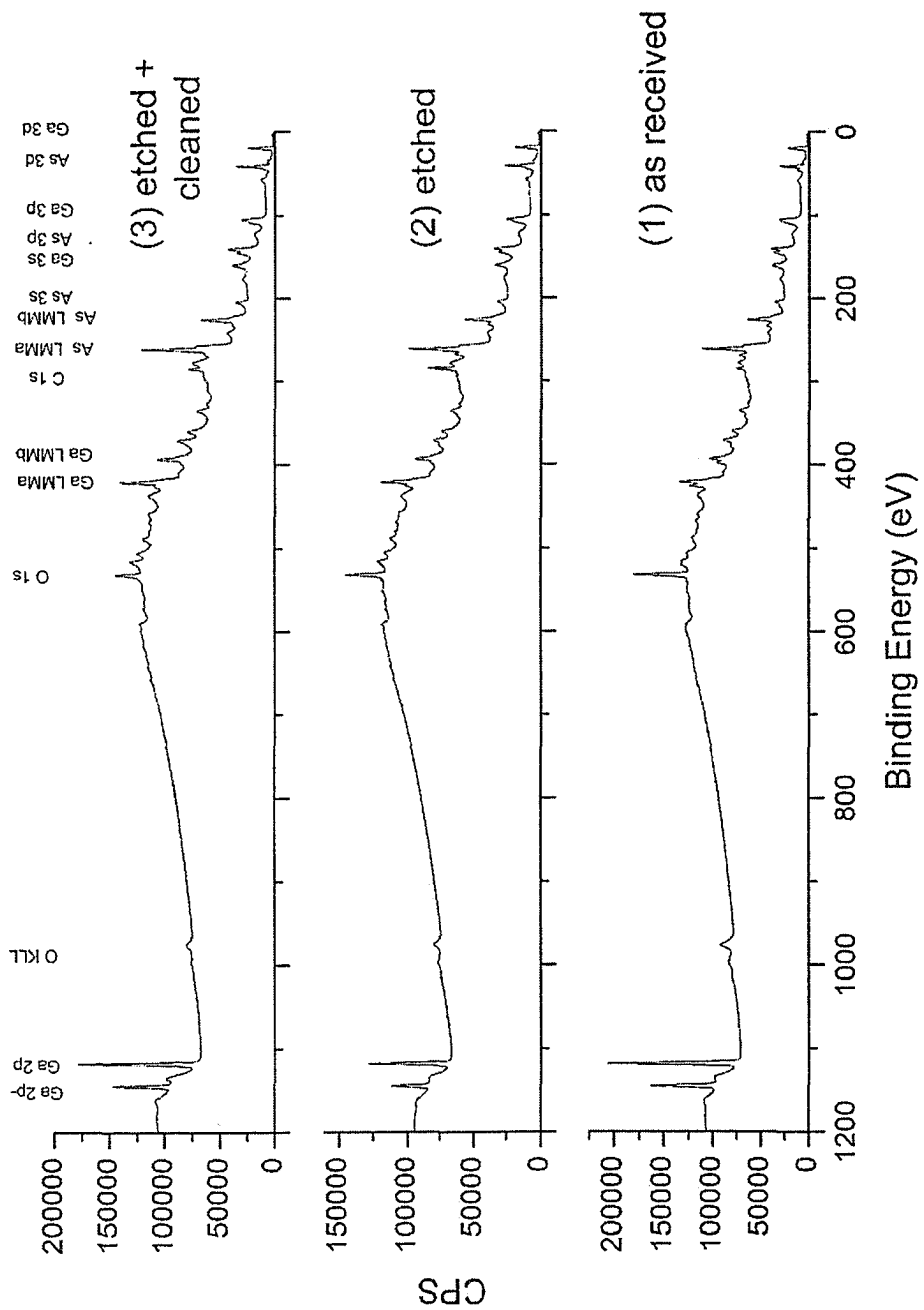
Figure 4-44 XPS spectra for examination of the cleaning procedures. (1) as-received sample; (2) the sample after etched in $H_2SO_4/H_2O_2/H_2O$ mixture; (3) after cleaning in 2.7 M NH_4OH of the sample in (2).

137

Table 4-4 XPS chemical composition analysis of the as-received, etched, etched + cleaned samples for n-GaAs (1×10^{18} cm^{-3}) from Figure 4-43.

Peak	Atomic concentration%		
	As-received	Etched	Etched + Cleaned
Ga 2p	15.9	7.5	15.1
O 1s	41.7	24.4	22.5
C 1s	17.1	44.4	28.9
As 3d	25.3	23.7	33.4

Table 4-5 Chemical composition analysis results (Ga/As ratio) from XPS after different treatments. Both n- and p-GaAs have doping levels of 1×10^{18} cm^{-3}.

Samples	Ga / As ratio
n(p)-GaAs as-received	0.60-0.62
n(p)-GaAs after etching	0.32-0.35
n(p)-GaAs after cleaning	0.42-0.45
n-GaAs corrosion in H$_2$SO$_4$	0.34
n-GaAs corrosion in NH$_4$OH	0.41
p-GaAs corrosion in H$_2$SO$_4$	0.21
p-GaAs corrosion in NH$_4$OH	0.37

138
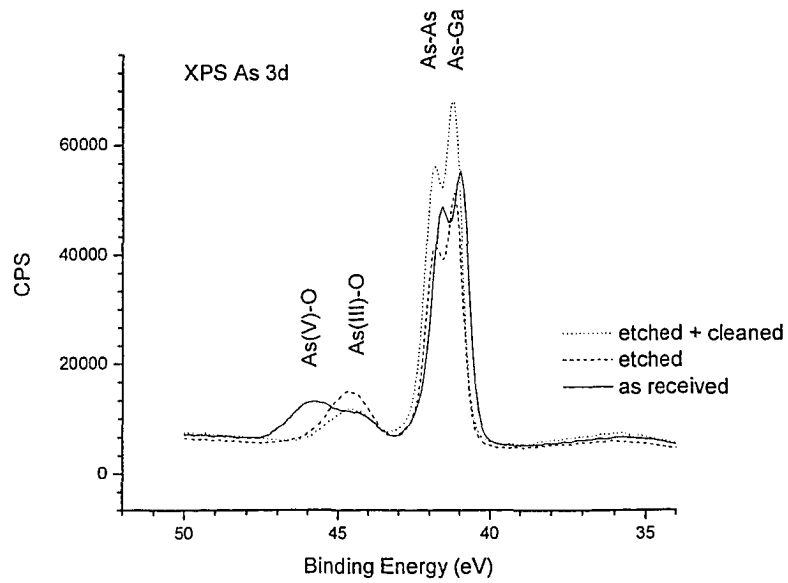
Figure 4-45 High resolution XPS spectra of As3d peaks for the as-received, etched and etched+cleaned n-GaAs (1×10^{18} cm^{-3}).
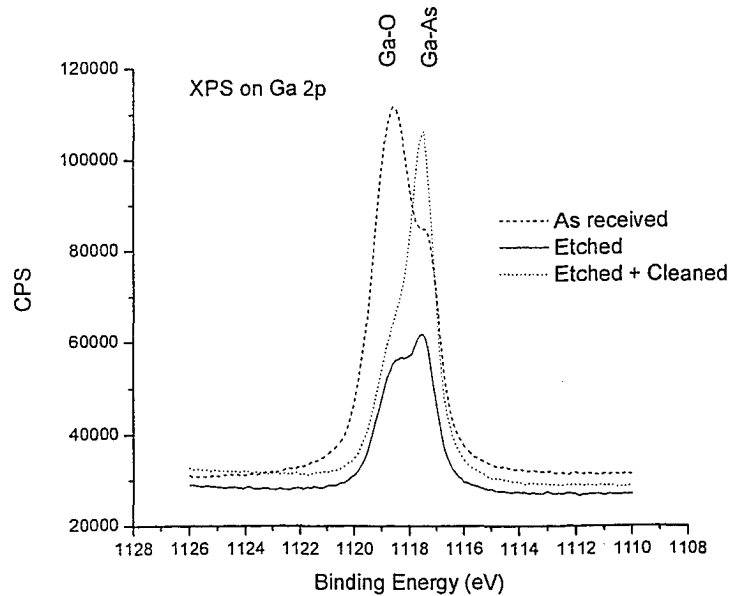
Figure 4-46 High resolution XPS spectra of Ga2p peaks for the as-received, etched and etched+cleaned n-GaAs (1×10^{18} cm^{-3}).
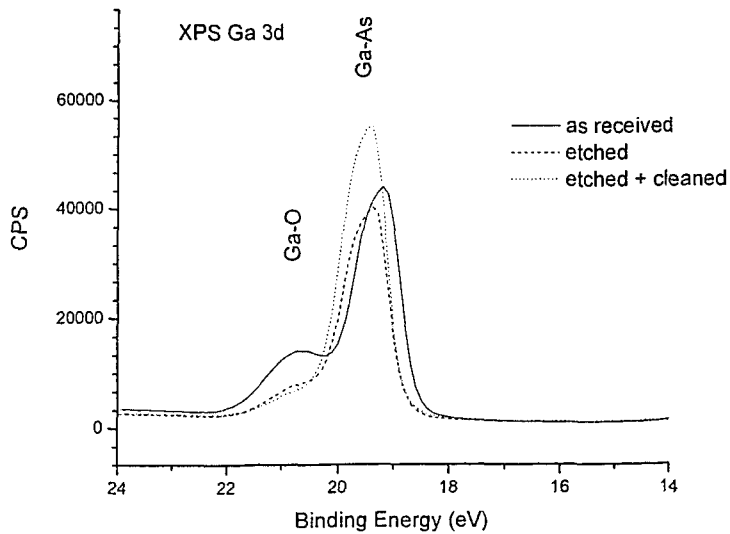
Figure 4-47 High resolution XPS spectra of Ga3d peaks for the as-received, etched and etched+cleaned n-GaAs (1×10^{18} cm^{-3}).
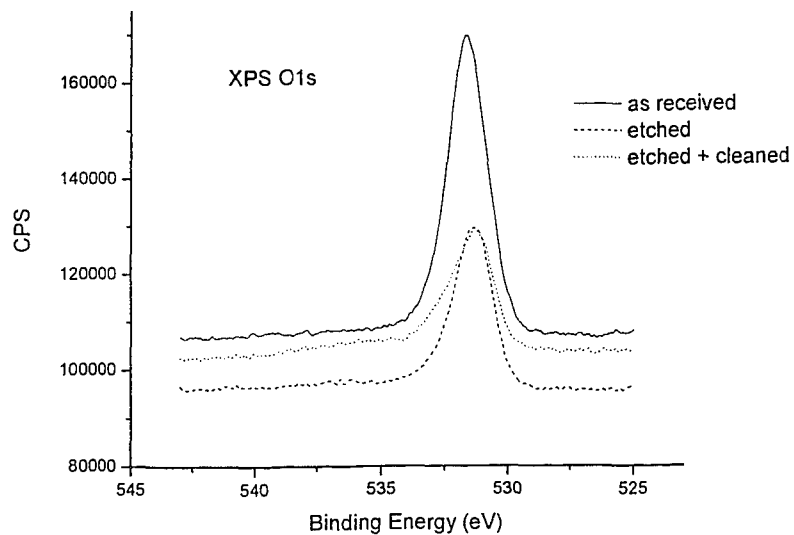
Figure 4-48 High resolution XPS spectra of O1s peaks for the as-received, etched and etched+cleaned n-GaAs (1×10^{18} cm^{-3}).

140

Table 4-6 Chemical composition analysis results from XPS O1s peaks.

Samples	O-Ga area %	O-As area %
n-GaAs corrosion in H_2SO_4	30	36
n-GaAs corrosion in NH_4OH	36	33
p-GaAs corrosion in H_2SO_4	30	48
p-GaAs corrosion in NH_4OH	26	37
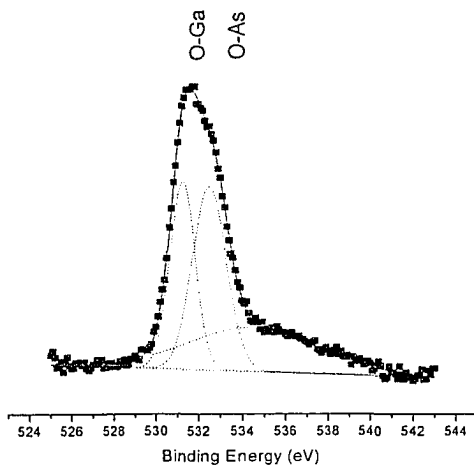
(a) *n*-type, after corrosion in H₂SO₄ solution
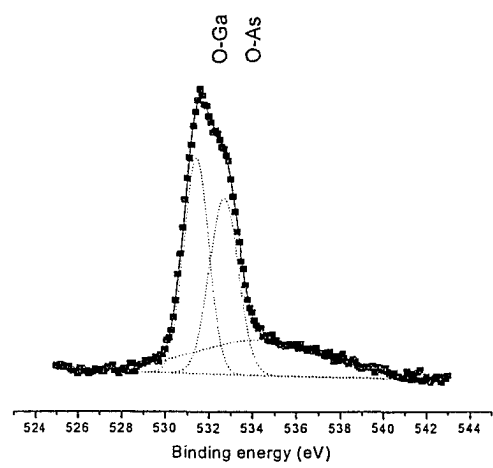
(b) *n*-type, after corrosion in NH₄OH solution
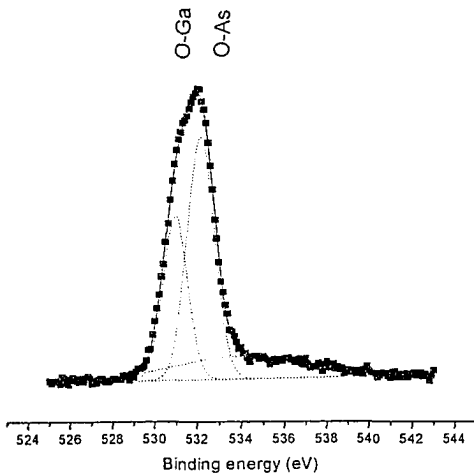
(c) *p*-type, after corrosion in H₂SO₄ solution
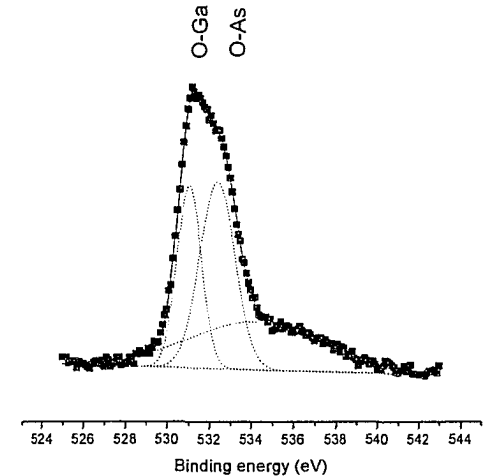
(d) *p*-type, after corrosion in NH₄OH solution

Figure 4-49 XPS O 1s spectra for *n*-GaAs and *p*-GaAs (1×10^{18} cm^{-3}) corroded in H₂SO₄ and NH₄OH in daylight conditions. (a) *n*-type in H₂SO₄; (b) *n*-type in NH₄OH; (c) *p*-type in H₂SO₄; d) *p*-type in NH₄OH.

142

References:

[1]   Notten, P. H. L., Meerakker, J. E. A. M. v. d. and Kelly, J. J. *Etching of III-V Semiconductors: an Electrochemical Approach*; Elsevier Advanced Technology: 1991.

[2]   Gomes, W. P. and Goossens, H. H. In *Advances in Electrochemical Science and Engineering*; Gerischer, H. and Tobias, C. W., Ed.; Vol.; VCH: Weinheim, 1994.

[3]   Gengsheng, W., *Corrosion Behavior of GaAs*, in *Department of Chemical & Materials Engineering*. 2002, University of Alberta: Edmonton.

[4]   Allongue, P. and Blonkowski, S., *J. Electroanal. Chem.* **1991**, 317, 57.

[5]   Allongue, P. and Blonkowski, S., *J. Electroanal. Chem.* **1991**, 317, 78.

[6]   Vanmaekelbergh, D. and Cardon, F., *J. Phys. D: Appl. Phys.* **1986**, 19, 643.

[7]   Batchelor, R. A. and Hamnett, A. In *Modern Aspects of Electrochemistry*; Bockris, J. O. M., et al., Ed.; Vol. 22; Plenum Press: 1992.

[8]   Edwin Oosterbroek, R. et al., *Journal of Microelectromechanics Systems* **2000**, 9, 390.

[9]   Hays, D., *Selective Etching of Compound Semiconductors*, Master Thesis, University of Floria, 1999.

[10]   Gerard, I., Debiemme-Chouvy, C., Vigneron, J., Bellenger, F., Kostelitz, S. and Etchberry, A., *Surf. Sci.* **1999**, 433-435, 131.

[11]   Beerbom, M., Henrion, O., Klein, A., Mayer, T. and Jaegermann, W., *Electrochim. Acta* **2000**, 45, 4663.

[12]   Solomun, T., McIntyre, R., Richtering, W. and Gerischer, H., *Surf. Sci.* **1986**, 169, 414.

[13]   Deng, Z. W., Kwok, R. W. M., Lau, W. M. and Cao, L. L., *Appl. Surf. Sci.* **2000**, 158, 58.

[14]   Lu, Z. H., Lagarde, C., Sacher, E., Currie, J. F. and Yelon, A., *J. Vac. Sci. Technol., A* **1989**, 7, 646.

[15]   Kang, M.-G., Sa, S.-H., Park, H.-H., Suh, K.-S. and Oh, K.-H., *Thin Solid Films* **1997**, 308-309, 634.

Chapter 5   Discussion

In this part, an overall discussion of GaAs corrosion is presented. The essential knowledge required to understand the GaAs corrosion process includes information on when corrosion happens, how corrosion occurs, how to determine the corrosion rate and finally how to control the corrosion. Thermodynamic data (standard potentials and mixed OCPs with the environment) control the stability of GaAs electrodes (see the Literature Review in Chapter 2 and the OCP part in Chapter 4 and the references therein). Band bending, and/or flatband potential are relevant to the surface charge concentration, affecting how fast corrosion can take place. The mechanism is the key part that determines how the corrosion is happening. Based on this, the following parts are discussed in this section: flatband potential, band bending, recombination processes, Tafel slopes in the polarization curves, breakdown mechanism and breakdown potential and the mechanism involved.

5.1 Flatband potential

5.1.1 Validity of direct Mott-Schottky measurements

There is no doubt that the direct Mott-Schottky measurement to determine the flatband potential and therefore the band bending is the most convenient approach. From the experimental point of view, a Mott-Schottky measurement is an ac voltammetric test. A small fixed frequency, sinusoidal signal is superimposed on a potential scan. Therefore, the data is obtained versus the scanned potential. In contrast, ac impedance measurement focuses on one fixed potential, with a frequency scan. The underlying equivalent circuit used in the Mott-Schottky measurement is a resistor in series with a capacitor, called a

144

simple RC circuit, as shown in Figure 5-1a. From now on, the subscript "MS" is applied to indicate that the elements are used in Mott-Schottky measurements. In physical terms, the two elements R_{MS} and C_{MS} are the serial resistance and the capacitance from the space charge region. Strictly speaking, any other chemical / electrochemical reactions or processes should not exist in order to use this $R_{MS}C_{MS}$ circuit to describe an electrochemical interface. In other words, these conditions must be met [1]:

(1) There should be no other reactions (electrochemical or non-electrochemical) which might introduce a resistor or other component into the equivalent circuit;

(2) The process should not be diffusion limited, which would result in a Warburg impedance;

(3) There should be no surface states, which in most cases result in a parallel circuit of resistor and capacitor;

(4) The surface must be clean (no films or adsorption layers) and perfectly flat (no fractal impedance).

The first two conditions should be met to guarantee no other electrical elements are in parallel with the space charge capacitor. The remaining conditions are to keep the assumption that nearly all the potential drop across the interface is in the space charge region – potential drop on the solution side is negligible.

From the results presented in Chapter 4, it is known that the above four conditions are not satisfied for the GaAs / aqueous solution interface (the acidic solution is the focus of the following discussion). The system is not expected to be as simple as the $R_{MS}C_{MS}$ equivalent circuit because of:

(1) GaAs instability.

GaAs is thermodynamically unstable in acidic solutions. Its decomposition potential is in the band gap and even in the dark and in the absence of holes, corrosion of GaAs can still occur, which is verified from open circuit potential observation. The OCP requires a period of time to stabilize.

(2) The existence of surface states.

145

GaAs can react with oxygen in the solution or air to form an oxide. Furthermore, the surface may not be perfect and defects can introduce new energy levels. Corrosion products are another possible source for surface states.

(3)   The presence of surface layers.

Corrosion products for GaAs in the H_2SO_4 solution are gallium oxide and elemental arsenic. Gallium oxide can dissolve in the acidic solution, while elemental arsenic does not and a film may be formed. Also in the 2.7 M NH_4OH solution, the dissolution of the corrosion products is very slow.

Therefore, theoretically, the $R_{MS}C_{MS}$ circuit is not suitable to characterize the GaAs electrode surface and the flatband potentials obtained from direct Mott-Schottky measurements are not valid. However, in Chapter 4.3.1, it was shown that a linear Mott-Schottky relationship holds for a certain potential region (almost from OCP to the breakdown potential). This result suggests that there is some validity for direct Mott-Schottky measurements of GaAs electrodes, although a slight frequency dependence of the flatband potentials was observed.

5.1.2 Rationale for using direct Mott-Schottky measurements

As mentioned in Chapter 4, the frequency dependence of the flatband potential indicates that the $R_{MS}C_{MS}$ equivalent circuit is not sufficient to describe the real interface reactions. Nevertheless, the plots of $1/C_{MS}^2$ vs. E over a certain potential region were linear, revealing some validity for these plots. The capacitance values from direct Mott-Schottky measurements are on the order of what would be expected for depletion layer capacitance (between 0.01 to 1 μFcm^{-2}), inferring that the potential applied mainly falls in the depletion region. Based on this, it seems that the effect of surface states and the double layer can be ignored.

From the polarization curves presented in Chapter 4, especially the curve for n-GaAs under illumination conditions, it can be concluded that the surface area is not

146

affected by the formed layer because a current plateau was observed, which is due to the constant hole injection rate by light. For p-GaAs, the valid Mott-Schottky region starts from some cathodic potential and continues to the OCP. In this potential region, the surface is "protected" and it is believed that the surface is clean. Diffusion problems have not been detected in voltammetric and impedance studies at potentials before breakdown for n-GaAs and "passivation" for p-GaAs.

After eliminating the effects of surface states and surface layers, the main factor that can invalidate the use of an $R_{MS}C_{MS}$ circuit to obtain the flatband potential is the reactions occurring during the measurements. For n-GaAs, the reaction is the oxidation of the electrode itself; for p-GaAs, the reaction is the reduction of oxygen in the solution by electrons. Because the potential applied almost entirely falls within the space charge region, the reactions occurring are definitely in parallel with the space charge region, rather than the double layer. Under this situation, the real equivalent circuit would be a typical Randles circuit, as shown in Figure 5-1b. The resistance $R_{Randles,1}$ in series is the same as the R_{MS}, the combined resistance of the solution and bulk GaAs. $R_{Randles,1}$, in parallel with the capacitance $C_{Randles}$, is the resistance due to charge transfer. $C_{Randles}$ is the real capacitance of the space charge region.

The relationship for the elements in Figure 5-1a and b can be calculated based on their respective impedance analysis. The circuit in Figure 5-1a has an impedance

$$Z_{MS} = R_{MS} + \frac{1}{i\omega C_{MS}} = R_{MS} - i\frac{1}{\omega C_{MS}}$$

(5.1)

The impedance of the circuit in Figure 5-1b is

$$Z_{Randles} = R_{Randles,1} + \frac{1}{\dfrac{1}{R_{Randles,2}} + i\omega C_{Randles}}$$

$$= R_{Randles,1} + \frac{R_{Randles,2}}{1 + \left(\omega R_{Randles,2} C_{Randles}\right)^2} - \frac{i\omega C_{Randles} R_{Randles,2}^2}{1 + \left(\omega R_{Randles,2} C_{Randles}\right)^2}$$

(5.2)

Comparing equations (5.1) and (5.2), the following relationships can be obtained:

147

$$R_{MS} = R_{Randles,1} + \frac{R_{Randles,2}}{1 + (\omega R_{Randles,2} C_{Randles})^2}$$ (5.3)

and

$$\frac{1}{\omega C_{MS}} = \frac{\omega C_{Randles} R_{Randles,2}^2}{1 + (\omega R_{Randles,2} C_{Randles})^2}$$ (5.4)

or

$$C_{MS} = \frac{1}{\omega^2 R_{Randles,2}^2 C_{Randles}} + C_{Randles}$$ (5.5)

If $C_{Randles}$ is the real capacitance of the space charge region, then equation (5.5) shows the relationship for the capacitance from direct Mott-Schottky measurement and the real capacitance of interest. It is frequency dependent. The condition required for C_{MS} to approach $C_{Randles}$ is

$$\omega R_{Randles,2} C_{Randles} \gg 1$$ (5.6)

or

$$f \gg \frac{1}{2\pi R_{Randles,2} C_{Randles}}$$ (5.7)

because

$$\omega = 2\pi f$$ (5.8)

Here, f is the frequency. Therefore, equation (5.7) is the criterion to select the frequency to probe the Mott-Schottky relationship. Taking the typical values of $R_{Randles,2}$ = 10^5 Ωcm^2 and $C_{Randles}$ = 10^{-7} Fcm^{-2}, then the frequency should be much higher than 15 Hz.

If the frequency picked is comparable to 15 Hz, then from equation (5.5) C_{MS} would be larger than $C_{Randles}$, i.e., the measured capacitance is larger than the real value. On the other hand, when the potential is anodic, the corrosion rate of GaAs, both n-type and p-type, increases, which means that the charge transfer resistance, $R_{Randles,2}$, decreases. It is implied that higher frequency should be used for more anodic potentials so that the frequency effect can be minimized. Therefore, for the same frequency used, as for direct

148

Mott-Schottky measurements, the discrepancy between C_{MS} and $C_{Randles}$ is expected to be larger at more anodic potentials. Schematic Mott-Schottky plots for the C_{MS} and $C_{Randles}$ are shown in Figure 5-2 and Figure 5-3 for n-GaAs and p-GaAs respectively. It can be directly inferred that the flatband potentials obtained from direct Mott-Schottky measurements will be more negative than those from the Randles circuit for n-GaAs. In addition, the doping level from the slope will be higher for direct Mott-Schottky measurements (Figure 5-2). This agrees with the results for the flatband potentials in Chapter 4. From direct Mott-Schottky measurements, for n-GaAs, the flatband potential is ~ -1.0 V, however, from the impedance measurements, using the Randles equivalent circuit for fitting, the flatband potential is ~ -0.71 V under dark conditions and ~-0.85 under illumination conditions. The flatband potentials from the impedance work are more credible.

The above analysis shows that direct Mott-Schottky measurements at low frequency are not accurate and the Mott-Schottky plot is not only frequency dependent, but also potential dependent. This brings up another question as to whether a higher frequency will produce better results. To answer this question is quite difficult. In the scope of this thesis work with the samples used, too high a frequency is not recommended. Most samples used in this thesis are GaAs epitaxial layers (~ 500 nm thick) at the desired doping levels on a substrate (semi-insulating or other doping levels). After the pretreatment procedure, about ~100 nm has been etched away. A higher applied frequency means that more perturbation is added to the interface. For n-type GaAs, if the flatband potential is assumed to be at -0.7 V, at OCP the band bending is already ~ 0.7 eV. This band bending corresponds to a depletion layer with a width of ~100 nm. At more anodic potentials, the depletion layer would be wider. At high frequency, the coupling from the interface in the bulk GaAs between the different doping layers will be a problem. This phenomenon is also observed in the impedance spectra. Figure 5-4 shows a typical Bode plot of the phase angle vs. frequency for n-GaAs in 0.5 M H_2SO_4 solution at 0.45 V. At the highest frequency, 100 kHz, the phase angle obtained is ~50°, i.e., still not zero. This indicates at least one capacitive circuit element is still active at such high frequencies. It also indicates that this capacitive element is very small, and is likely not

149

related to the space charge region and the double layer. The probable source of the element is the interface between the different doping level layers. The existence of such an element implies that high frequency is also not good for investigating the depletion layer using the RC equivalent circuit. However, for a sample with completely uniform doping through the thickness, high frequency is recommended to reduce the errors from direct Mott-Schottky measurements[9].

5.1.3 Summary

From the above analysis, on the frequency effect during the measuring of flatband potentials, it was shown that the frequency chosen is very important. In most cases, low frequencies are not good because of interference from other elements in the equivalent circuit. Too high a frequency is also not good for the samples used in this thesis work, because of the existence of different doping layers.

The discrepancy between the direct Mott-Schottky measurement and the results from the impedance spectroscopy have been investigated. As shown, this discrepancy is not only frequency dependent, but also potential dependent, resulting in more difficulties in choosing the frequency for direct Mott-Schottky measurements. For n-GaAs, the flatband potentials obtained from direct Mott-Schottky measurement are more negative than those from Randles circuit fitting and the doping levels are smaller, in agreement with the experimental results. In conclusion, the flatband potentials from the impedance work are more credible.

---

[9] This does not mean a higher frequency is always better. At extremely high frequencies, other effects must be considered, e.g., the inductive effects in the measuring loop (http://www.consultrsr.com/resources/eis/induct1.htm).

5.2 Tafel slope and surface states

5.2.1 Tafel slope

The Tafel slope from steady-state polarization curves is the main parameter to determine how the reaction is controlled electrochemically / chemically. For a single-electron electrochemical reaction on metal electrodes, the Tafel slope is expected to 120 mV per decade [2]. However, for semiconductor electrodes, the potential applied not only falls in the double layer on the solution side, but also the space charge region in the semiconductor side. For a general picture, the potential applied in the semiconductor / electrolyte system is divided into potential drops in two regions: the space charge layer and the Helmholtz layer:

$$V = \varphi_{SC} + \varphi_H \tag{5.9}$$

The relative changes between these two potential drops can be expressed as

$$\frac{d\varphi_H}{d\varphi_{SC}} = \frac{C_{SC} + C_{SS}}{C_H} \tag{5.10}$$

where C_H, C_{SC} and C_{SS} represent the capacitance of the Helmholtz layer, the space charge layer and the surface states respectively. Normally the capacitance for surface states is in parallel with the space charge region (Figure 5-5a). For n-GaAs under dark conditions, without external hole injection, the hole concentration at the surface is exponentially proportional to its bulk concentration, if fast thermionic emission of holes is assumed:

$$p_s = p_B \exp\left(\frac{e\varphi_{SC}}{kT}\right) \tag{5.11}$$

For the simplest case, assuming the current density is proportional to p_s, it is easy to determine the Tafel slope:

$$\frac{dV}{d\log j} = \frac{2.3kT}{e}\left(1 + \frac{C_{SC} + C_{SS}}{C_H}\right) \tag{5.12}$$

151

For relatively low anodic potentials, from OCP to breakdown (called the mild potential region hereafter), a depletion layer is formed in n-GaAs and C_{SC} would be much smaller than C_H, which is the basis for the Mott-Schottky relationship. A Tafel slope of 300–450 mV per decade for n-GaAs in dark conditions, obtained in Chapter 4, would suggest that C_{SS} is about 4-6 times that of C_H. Moreover, the linear shape also implies that the value of C_{SS}/C_H is independent of the potential applied before breakdown.

Fitting results for the impedance spectra suggest that the capacitive loop in the high frequency area, observed in all potential regions, is dominated by the space charge region because the values are typical of the capacitance from a semiconductor depletion region. Furthermore, the Mott-Schottky plots using the capacitance values from the fitting results gave reasonable doping levels, compared with the as-marked values. No phenomena related to the surface states have been found. The existence of surface states is in doubt. Also from the charge transfer resistance, fitting of the impedance spectra suggests that the charge transfer resistance is in parallel with the space charge region, rather than the double layer. This means the corrosion is mainly occurring on the GaAs side, not on the solution side. The large current density difference, between the dark conditions and illumination conditions for n-GaAs, implies that the hole concentration limits the corrosion that takes place. Therefore it is inferred for n-GaAs, in the mild potential region, that corrosion is determined by the hole concentration at the surface. Under illumination conditions, the constant hole injection rate by the light results in a current plateau. It can then be argued that the Tafel slope of 0.35 – 0.40 V per decade corresponds to the rate of hole generation.

The possibility of an abnormal situation where C_{SC} is in series with C_{SS} can also be eliminated (Figure 5-5b). This situation can appear when the surface states are a relatively compact layer (surface coverage is high) and the surface is flat. This is not readily possible for n-GaAs in the mild potential region. Moreover, if 5/6 of the potential applied falls in the surface states capacitor, C_{SS} should be 1/5 of C_{SC}. At this time, C_{SS} would be detected in both direct Mott-Schottky measurements and impedance spectra. A linear Mott-Schottky plot is not possible for this situation. In addition, if the surface states

152

take over most of the potential applied, the current – voltage behavior of *n*-GaAs under illumination conditions would not correspond to the experimental results. No plateau should be observed because the reaction rate will not be limited by the hole concentration at the surface.

It can be derived from the above analysis that the potential applied mainly falls in the space charge region. However, the potential drop in the depletion region does not produce holes as expected theoretically. The reason is unknown at this time. A similar phenomenon was also observed for the *p*-Ge electrode [3]. The observed Tafel slope was much larger than would be expected for the proposed mechanism.

The discrepancy between calculation and experimental data leads one to question whether the thermal generation rate of the holes is fast enough to follow the Fermi-Dirac distribution in the space charge region. First of all, the reverse bias of a *p-n* junction has a saturation current density on the nAcm^{-2} scale, from the diffusion of minority charge carriers driven by the concentration gradient, which is much smaller than current density in the experiment results. Secondly, the current from thermal generation of hole and electron pairs in GaAs is larger than the saturation current; however, the thermal charge carrier generation rate is proportional to the width of the space charge region, which does not have a logarithmic dependence on the band bending.

$$v_{TH} \propto W \propto \phi_b^{1/2} \tag{5.13}$$

where v_{TH} represents the thermal generation rate of the charge carriers. Therefore, it is believed that the thermal generation rate of the holes is sufficiently fast and thermal equilibrium is established on the semiconductor side during the experiments.

For *p*-GaAs, from the experimental results, the Tafel slope was found to be ~120 mV per decade. This is understandable since the hole concentration for *p*-GaAs is high at the potential region close to flatband potential and the hole generation rate is not the slowest step in the reactions. The corrosion rate is limited by the electrochemical

153

consumption of the holes by GaAs. Again, the electrochemical symmetry factor calculated from 120 mV per decade Tafel slope is ~0.5, which is reasonable.

5.2.2 Existence of surface states

Whether surface states exist at the surface of GaAs is a difficult topic to investigate. Although many experiments have been performed by various techniques that provide some evidence for the presence of surface states (see Chapter 2), there is still no direct evidence yet. In this thesis work, from the several approaches applied, the presence of surface states is doubtful.

(1) Polarization curves: For n-GaAs under dark conditions, the Tafel slope is unexpectedly small, suggesting that the potential has a small effect on the current density. If surface states are involved in the charge transfer process, an increase in the current density would be observed.

(2) Direct Mott-Schottky measurements: A valid linear region for the curves was obtained, indicating that the capacitances detected are mainly from the space charge region. This was also confirmed from the values of the capacitances. No evidence for surface states was found.

(3) Impedance spectra: In the mild potential region for n-GaAs, the impedance spectra only contain one capacitive loop, with the capacitance value equal to that for a typical depletion layer.

(4) Breakdown studies: For n-GaAs, in the presence of surface states, breakdown would be expected to be much more difficult than shown here, because the applied potential would be mainly taken by the surface states.

154

5.3 Breakdown Potential Discussion

Breakdown is observed for all *n*-GaAs samples at sufficiently high anodic potential. Breakdown refers to a sudden current density increase relative to the behavior in the mild potential region. Breakdown is more easily to study under illumination conditions because a turning point for the breakdown can be easily determined. Under dark conditions, the slope of the polarization curves after breakdown is much smaller than the Tafel slope. After breakdown, the behavior of *n*-GaAs is almost the same for both the dark conditions and illumination conditions, suggesting that breakdown is a feature of *n*-GaAs itself, not related to external hole injection. The following discussion is based on the breakdown potential obtained from *n*-GaAs under illumination conditions.

In the published literature, breakdown was simply studied and, by comparing the breakdown potentials with those in Schottky diodes at the same doping level, it was concluded that breakdown occurred much earlier (lower potentials) than expected. This was explained by the presence of surface defects, resulting in local breakdown [4].

Three possible reasons can result in breakdown: the formation of an inversion layer from the original depletion layer, avalanche breakdown and tunneling breakdown. The following will analyze the breakdown mechanism and identify the factors that lead to breakdown.

In order to perform quantitative calculation, accurate parameters for *n*-GaAs are required, e.g., position of Fermi energy levels and effective doping densities. Since the doping density level used in this study is above 1×10^{17}, the corresponding Fermi energy level cannot be calculated simply from the Maxwell-Boltzmann approximation to the Fermi-Dirac distribution. The Nilsson approximation is used here instead. This approximation method is believed to have an error less than 1%. The methods for the Nilsson approximation can be referred to in Appendix A.

155

The Fermi energy levels and effective doping densities for a series of n-GaAs samples are given in Table 5-1. The positions of the Fermi energy levels are shown by the relative difference from E_C, the conduction band edge. From the Fermi energy level calculation, it can be seen that all the $|E_F\text{-}E_C|$ values are less than $3k_BT$, indicating that GaAs at these doping levels is degenerate. This can be shown further by the calculated effective doping densities. It is found that 70% of dopants are ionized at 1.0×10^{17} cm^{-3} doping level and only 13% of dopants are ionized at 5.0×10^{18} cm^{-3} doping level. The experimental breakdown potentials for different doping levels are summarized in Table 5-2.

5.3.1 Inversion layer formation

One possible reason for the breakdown behavior is the formation of an inversion layer, since from the experiments the flat band potential of the n-GaAs is around -0.85 V vs. SCE. At a potential more positive than 0.6 V, an inversion layer may form because the band gap of GaAs at 300 K is 1.424 eV. One criterion to define the formation of inversion layer is that the concentration of the minority charge carriers at the surface is equal to the concentration of the majority charge carrier in bulk. For n-GaAs, then, the inversion layer forms at the potential where the hole concentration at the surface is equal to the concentration of electrons in the bulk. Thus, when the inversion layer forms, the band bending has this relationship with the Fermi energy level and the intrinsic energy level:

$$\phi_b = 2(E_F - E_i) \tag{5.14}$$

Here, it is reasonable to assume that the flat band potentials of these different n-GaAs doping densities are the same (the flat band potential should refer to the Fermi energy level of the semiconductor in vacuum) because from the calculation in Table 5-1, the difference between the Fermi level and the conduction band edge is small ($<$ 0.07 eV). It can be inferred that at the formation of the inversion layer,

$$e(V_{inv} - V_{fb}) = 2(E_F - E_i) \tag{5.15}$$

156

where V_{inv} refers to the potential at which the inversion layer forms.

From equation (5.15), the higher the doping density, the larger the value of E_F-E_i and thus the more positive the value of V_{inv}. This is in conflict with the experimental results if breakdown of the semiconductor is due to the formation of an inversion layer (Table 5-2). In Table 5-2, the breakdown potential decreases with increasing doping level. Therefore, it can be concluded that the breakdown of the semiconductor is not due to inversion layer formation even though there may be other criteria to define the potential where the inversion layer forms.

5.3.2 Tunneling breakdown

The second possibility for breakdown is the increasing tunneling probability as the depletion layer width decreases and the electric field inside the depletion layer increases. As is commonly known, the breakdown of Si or GaAs is due to tunneling if the breakdown potential (indeed this should be the band bending at breakdown) is less than $4E_g$ and due to avalanche mechanism if the breakdown potential is higher than $6E_g$. This is because avalanche breakdown requires higher electrical fields to dissociate electrons from the compound and then accelerate them to a enough high energy to bombard the valence bonds to gain more electrons. Tunneling breakdown can only occur for high doping level semiconductors, since tunneling probability through a thick barrier is very low. Breakdown potentials from the experimental results are all smaller than $4E_g$ (5.68 eV) and so it can be assumed that the breakdown occurs by tunneling through the interface.

A schematic illustration of how the tunneling occurs is shown in Figure 5-6. At large band bending, with a relatively small depletion layer width due to the high doping level, electrons in the solution can tunnel through the energy barrier into GaAs. Because the energy barrier is not rectangular, in a general approximation, it can be replaced by a half triangular barrier, with the width W shown in Figure 5-6. The tunneling probability

157

can then be calculated by solving the Schrodinger equation using the Wentzel-Kramers-Brillioun (WKB) approximation [5, 6].

$$P = \exp\left(-\frac{16\pi}{3}\sqrt{\frac{m^* \varepsilon_{SC} \varepsilon_0}{n_{eff}}}\frac{\phi_b}{h}\right)$$

(5.16)

Here P is the tunneling probability, m^* is the electron effective mass, h is the Plank constant and n_{eff} is the effective doping density. The tunneling breakdown probability trend is in agreement with the experimental results. From equation (5.16) it can be seen, for the same band bending ϕ_b, that higher doping level samples have higher effective doping densities, n, which result in a higher probability P.

From the general features of Zener diodes on Si and Ge, it was suggested that for tunneling to happen, the electric field inside the depletion layer must be high, $\sim 10^5$ Vcm^{-1}, and the depletion layer width should be ~ 0.1 nm. For GaAs, the required electric field may be smaller and the depletion layer width can be larger because of relative lighter charger carriers in GaAs. However, in general, tunneling is not possible through a barrier width larger than 50 nm. From Table 5-2, it can be seen that at the breakdown potentials obtained from the experiments, the width of the space charge region is much larger than ~ 0.1 nm. For example, for the highest doping sample investigated, the width of space charge region is around 50 nm. For those lower doping levels, the width is even larger. Tunneling probability across such a wide energy barrier is extremely low and the tunneling mechanism is not suitable for the explanation of breakdown.

5.3.3 Avalanche breakdown

The last possible explanation for the breakdown potential is the breakdown electric field (avalanche breakdown). The breakdown electric field for GaAs is $\sim 4 \times 10^5$ Vcm^{-1}. For a Schottky barrier, these equations were utilized:

$$W = \sqrt{\frac{2\varepsilon}{qN}(V_o + V_{app})}$$

(5.17)

158

and

$$E_{br} = \sqrt{\frac{2q}{\varepsilon} N (V_o + V_{br})}$$ (5.18)

where V_o is the internal Schottky barrier height, ε is the dielectric constant of the semiconductor, W is the width of the depletion region, E_{br} is the breakdown electric field and V_{app} is the applied potential. Indeed, $e(V_o + V_{app})$ is the band bending value at the applied potential V_{app} and $e(V_o + V_{br})$ is the band bending at breakdown potential. Note, that if a certain critical breakdown electric field is present, an increase in doping would give a decrease in breakdown potential, which agrees with the experimental results. Therefore, using the data in Table 5-1 and equations (5.17) and (5.18), the theoretical values of the breakdown potential (band bending here) and corresponding depletion region width can be calculated, which are listed in Table 5-3.

Comparing the data in Table 5-2 and Table 5-3 (referring to the flatband potential ~-0.85 V), it can be concluded that for a doping density of 1.0×10^{17} cm^{-3} the experimental value is much lower than the theoretical result. For doping densities from 1.0×10^{18} cm^{-3} to 2×10^{18} cm^{-3}, the experimental values are close to the theoretical results. The calculated breakdown band bending for a doping density of 5×10^{18} cm^{-3} is smaller than the experiment result, which may be due to the strong recombination effect in this degenerate sample. From surface morphology studies, it was inferred that the corrosion in 0.5 M H_2SO_4 solution may be via a pitting mechanism. Therefore it is possible to examine whether the lower breakdown potential is due to surface irregularities. In Figure 5-7, an n-type GaAs sample (1.0×10^{17} cm^{-3}) was polarized under three conditions: (1) a fresh surface after etching and cleaning; (2) sample (1) after a further cleaning; and (3) sample (2) after additional cleaning. The breakdown potential decreases with the second measurement and further still with the third measurement, indicating that the surface roughening has a major impact on the breakdown potential. The rougher the surface, the easier it is for breakdown.

159

5.3.4 Recombination Impedance

According to the decomposition mechanism for many III-V semiconductors, the first reaction step of capturing a hole by a surface bond can be written as [7]:

$$X_0 + h^+ \rightarrow X_1 \tag{5.19}$$

Recombination impedance was found from the impedance spectra, in the potential region slightly higher than the open circuit potential, and may overlap with the space charge capacitive loop for n-GaAs under illumination conditions. The decomposition of GaAs consists of several steps, as six charges and several intermediates are expected to exist during corrosion. Surface recombination can happen on such intermediates or on already existing recombination centers regardless of the electrode processes. The results of photoanodic stabilization experiments on n-GaAs and n-GaP by Vanmaekelbergh et al. [8, 9] have shown that the recombination process occurs on the intermediates produced from the dissolution process.

It is unlikely that the recombination occurs on the dissolution intermediates, since experimental results here indicate that recombination impedance was only found in the potential region L1 under illumination conditions (Figure 4-8). In this potential region, due to the small overpotential applied, the consumption of the holes by corrosion of GaAs is not high and is comparable to the recombination rate. With the increasing rate for oxidation of GaAs, the recombination rate can be neglected and holes injected by illumination are mainly consumed by the electrochemical processes. In the potential region L1, the small oxidation rate indicates that the concentration of the corrosion intermediates is low. Furthermore, the concentration of the corrosion intermediates is believed to be higher in potential regions L2 and L3. Based on this, if the recombination centers are the corrosion intermediates, the recombination impedance is more likely to be observed in potential regions L2 and L3 than potential region L1.

The above discussion can also apply to eliminate the surface states as the recombination centers. Qualitatively, when the applied potential goes more positive, the

concentration of unoccupied surface states will be higher, in contradiction to the trend of the recombination impedance. Therefore, it can be concluded that the recombination process is via the already existing active states. The disappearance of the recombination impedance at more anodic potentials is due to the increasing hole consumption rate.

Figure 5-8 shows the recombination impedance trend at and close to the OCP. When the potential becomes more positive, the first capacitive loop which is assigned to the space charge layer enlarges while the loop assigned to the recombination loop diminishes. The relatively "flat" shape of the recombination loop, an arc rather than a semicircle, indicates that there is a CPE with a small coefficient. The model of equations (4.4) to (4.6) is too simple to describe the recombination impedance. It was demonstrated by Vanmaekelbergh and Cardon [10] that even if the change in hole concentration at the surface was considered, the equivalent circuit of the recombination process is still an $R(RC)$ combination. The nature of the CPE remains unclears. Another possible reason for this distorted capacitive loop may be due to the relatively low accuracy of the impedance data at low frequency (<0.1 Hz). The much higher impedance (close to 0.5 MΩcm^2) of the semiconductor / electrolyte interface under depletion conditions is also a challenge to the input impedance of the instruments used.

5.4 Model and impedance calculation for n-GaAs in the 0.5 M H$_2$SO$_4$ system

For many years, the first two electron surface bond breaking processes for GaAs were considered to be the main processes necessary for current analysis [11]. Based on this, the simulation of the current voltage behavior was independent of the reaction scheme. Moreover, the breaking of the first bond was assumed to be the rate determining step of the overall corrosion reactions, although six charges might be involved. From impedance results presented here, the current voltage curve consists of three distinguishable regions. Especially at the breakdown potential, different circuit elements emerged in the low frequency domain, indicating changing rate determining steps. In the

161

recent work on InP by Hens and Gomes [12], the rate determining step was found to be the fourth or fifth charge transfer step before current saturation, under illumination conditions (region L1 in Figure 4-8). These results suggest that a careful re-examination of the rate determining step for the corrosion process is necessary.

Based on many recent surface characterization results, mainly XPS [13-15] and the mechanisms of III-V semiconductor electrochemical dissolution discussed in the literature [7, 11, 16-21], a new model for the GaAs decomposition in strong acidic solution is proposed below. In this model, the following statements are made and the (100) surface is utilized for illustration purposes. For simplicity, the possible groups saturating the surface bonds, e.g., -OH, are omitted [7].

1. Before corrosion takes place, the surface of GaAs after etching and cleaning, is arsenic-rich and hence the outermost exposed layer will be an As (100) plane with dangling bonds. This was confirmed by the literature [14] and also through XPS in the experimental results presented here. A schematic illustration of such a surface is shown in Figure 5-9a, written as $AsGa_s$, with the subscript "s" denoting a surface bond.

2. As generally acknowledged, the first oxidation step is a hole captured by the surface bond and one Ga-As bond is broken. This process leaves a positive charge on the Ga instead of the As, based on the lower electronegativity of Ga versus As. The resulting surface is shown in Figure 5-9b and can be written as $AsGa^+$.

3. The surface in Figure 5-9b is easily attacked by water molecules from aqueous solutions, because of the positive charge located at Ga. Two kinds of interactions might be involved. One is the general interaction between the positive charges and the dipole from the water molecules and/or the cations in the solution, i.e., non-specific adsorption. The other is the much stronger chemical reaction between water and the positive charge. AsGa-OH can be formed and H^+ is generated (Figure 5-9c). The non-specific adsorption will be related to the double layer and the latter

162

will be related to the space charge layer. In most situations, the effect of non-specific adsorption is small and can be safely omitted. Nonetheless, there are two common features of the two kinds of interactions. Firstly, both interactions rely on the solution pH values. The adsorption of water molecules will change the potential drop falling in the Helmholtz layer and the reaction with water is definitely dependent on the solution pH values. Secondly, both interactions are believed to be fast processes. The equilibrium constant is adequate to describe the reaction with water. In strong acidic solutions, $AsGa^+$ is stabilized and in strong alkaline solutions, $AsGa-OH$ will be more stable.

4. From Figure 5-9a, it is shown that each surface As atom only bonds to two Ga atoms below and, therefore, it is inferred that only two oxidation steps are required to release the surface As atom to form elemental arsenic, $As(0)$. Because of the low solubility of $As(0)$ in strong acidic solutions, an elemental arsenic layer will form at surface. However, from the polarization curves in Figure 4-8 and also the literature [14], it is known that the elemental arsenic layer has a negligible effect on the corrosion behavior since no reduction in active surface area was observed. Thus, this elemental arsenic layer should be porous which was also verified from previous work in this group [15]. Nevertheless, the elemental arsenic can be further oxidized to $As(III)$ at sufficiently anodic potentials.

5. After the elemental arsenic layer forms, the Ga (100) plane is exposed. The breaking of two Ga-As bonds leaves the Ga with two positive charges (Figure 5-9d). Similar to the statements in point (3), if the interaction between Ga and water molecules is considered, there will also be equilibrium between $=Ga^{2+}$, $-Ga^+OH$ and $-Ga(OH)_2$. Corresponding equilibrium constants can be used to characterize the proportion that each form has. The equilibrium is quite dependent on the solution pH values. In the solutions used in this work, 0.5 M H_2SO_4, it is believed the main form is $=Ga^{2+}$ and for simplicity, only $=Ga^{2+}$ will be considered in the simulation below.

163

6. The exposed Ga (100) plane is similar to the As (100) plane. Each $=Ga^{2+}$ is still bonded with two As atoms below. In point (4), it was mentioned that the two bonds require two oxidation steps to break. However, this is not applicable to the $=Ga^{2+}$ plane. This is because there are only three outer shell electrons in a Ga atom, compared to the five outer shell electrons in an As atom. From hybridization theory, both Ga and As atoms have sp^3 orbital hybridization, generating molecular orbitals to accommodate the total of eight electrons when four covalent bonds are formed for each Ga or As atom (tetragonal crystal structure). The new molecular orbitals generated by hybridization are degenerated again to form a band for a solid of crystal. The aim of both the hybridization and degeneration of atomic orbitals and molecular orbitals, respectively, is to lower the total electron energy and thus the whole substance's energy. Hence, the point is that when no electrons are involved, hybridization and degeneration will not happen because the energy is not lowered. Therefore, when another oxidation step occurs to break a Ga-As bond, all the outer shell electrons for Ga are used up. The hybridization of Ga atomic orbitals is not necessary any more and the other Ga-As bond has no basis to exist and will break at the same time, generating a Ga^{3+} ion. It should be noted that in the alkaline solutions, the surface Ga atoms are in the form of $=Ga(OH)_2$. The electrons in the Ga-O bonds cannot help in the sp^3 hybridization, because the Ga-O bond is mostly ionic, not covalent. The above statement is still valid with the product being $Ga(OH)_3$, instead of Ga^{3+} ions.

7. From the above analysis, three oxidation steps are involved to produce elemental arsenic, As(0) and Ga(III) (Ga^{3+} in this study and $Ga(OH)_3$ if in alkaline solutions). Adding the other three charge transfer steps for the oxidation of As(0) to As(III) (As_2O_3 or $HAsO_2$), a total of six oxidation steps is needed, conforming to the generally accepted reaction.

$$GaAs + 6h^+ \rightarrow Ga(III) + As(III) \tag{5.20}$$

From the impedance results at potentials before breakdown, the capacitance obtained is mainly from the depletion region, although the theoretical Tafel slope does not match the experimental results. The potential drop in the solution double

164

layer does not change significantly, providing evidence that from a thermodynamic point of view [22], before breakdown, oxidation of As(0) to As(III) is less likely in a strong acidic solution. It is not necessary to consider the further oxidation of As(0) in mild potential regions, in contrast to the decomposition of InP [12, 23]. At potentials more positive than the breakdown, GaAs is susceptible to degeneration. In such cases the applied potential mainly falls in the Helmholtz layer and the oxidation of As(0) should be considered. In the simulation below, a Faradaic polarization resistance (R_{ct2} in Figure 4-25b and d) is added in parallel with the double layer capacitor.

8. The oxidant involved can be holes, and also the reactant intermediates. Corresponding to the notation in the literature, corrosion with only holes as the oxidant is denoted as an H mechanism. Corrosion with holes as the first oxidation step and reactant intermediates as further oxidants is denoted as an X mechanism. Combined with the hydration reactions of the intermediates, the mechanisms are denoted as an H-C mechanism and X-C mechanism respectively (here "C" represents chemical reactions). In this simulation, the first intermediate is considered as the most active oxidant in order to simplify the calculations.

Based on the ideas presented above, the reactions involved in GaAs corrosion consist of these steps.

Reaction 1	$AsGa_S + h^+ \rightarrow AsGa^+$
Reaction 2	$AsGa^+ + e^- \rightarrow AsGa_S$
Reaction 3	$AsGa^+ + H_2O \rightleftharpoons AsGa\text{-}OH + H^+$
Reaction 4	$AsGa\text{-}OH + H^+ + e^- \rightarrow AsGa_S + H_2O$
Reaction 5	$AsGa^+ + h^+ \rightarrow As(0) + =Ga^{2+}$
Reaction 6	$AsGa\text{-}OH + h^+ \rightarrow As(0) + =Ga^+\text{-}OH$
Reaction 7	$AsGa^+ + AsGa^+ \rightarrow As(0) + =Ga^{2+} + AsGa_S$
Reaction 8	$AsGa\text{-}OH + AsGa^+ \rightarrow As(0) + =Ga^+\text{-}OH + AsGa_S$

Reaction 9	$=Ga^{2+} + H_2O \rightleftharpoons =Ga^+-OH + H^+$
Reaction 10	$=Ga^+-OH + H_2O \rightleftharpoons =Ga-(OH)_2 + H^+$
Reaction 11	$=Ga^{2+} + h^+ \rightarrow Ga^{3+}$
Reaction 12	$=Ga^+-OH + H^+ + h^+ \rightarrow Ga^{3+} + H_2O$
Reaction 13	$=Ga-(OH)_2 + 2H^+ + h^+ \rightarrow Ga^{3+} + 2H_2O$
Reaction 14	$=Ga^{2+} + AsGa^+ \rightarrow Ga^{3+} + AsGa_S$
Reaction 15	$=Ga^+-OH + H^+ + AsGa^+ \rightarrow Ga^{3+} + H_2O + AsGa_S$
Reaction 16	$=Ga-(OH)_2 + 2H^+ + AsGa^+ \rightarrow Ga^{3+} + 2H_2O + AsGa_S$

In these reactions, reactions 3, 9 and 10 are hydration reactions of the intermediates and they are believed to be fast, as mentioned above. Reactions 2 and 4 are recombination reactions. Recombination on the intermediates is not considered, since As(0) is unlikely to be reduced to a surface bond. The others are all oxidation steps for different intermediates or surface bonds. The intermediates can be divided into two groups: Ga(I), including $AsGa^+$ and AsGa-OH, and Ga(II), including $=Ga^{2+}$, $=Ga^+-OH$, $=Ga-(OH)_2$. Taking into account the solution pH value (~0.05), the forms without –OH groups would be the main components existing and neglecting these hydrated intermediates will not influence the simulation results. On the basis of the above analysis, the 16 reactions can be simplified into these steps.

Step 1	$AsGa_S + h^+ \xrightarrow{k_1^*} AsGa^+$
Step 1'	$AsGa^+ + e^- \xrightarrow{k_{1'}^*} AsGa_S$
Step 2	$AsGa^+ + h^+ \xrightarrow{k_2^*} As(0) + =Ga^{2+}$
Step 2'	$AsGa^+ + AsGa^+ \xrightarrow{k_{2'}^*} As(0) + =Ga^{2+} + AsGa_S$
Step 3	$=Ga^{2+} + h^+ \xrightarrow{k_3^*} Ga^{3+}$
Step 3'	$=Ga^{2+} + AsGa^+ \xrightarrow{k_{3'}^*} Ga^{3+} + AsGa_S$

166
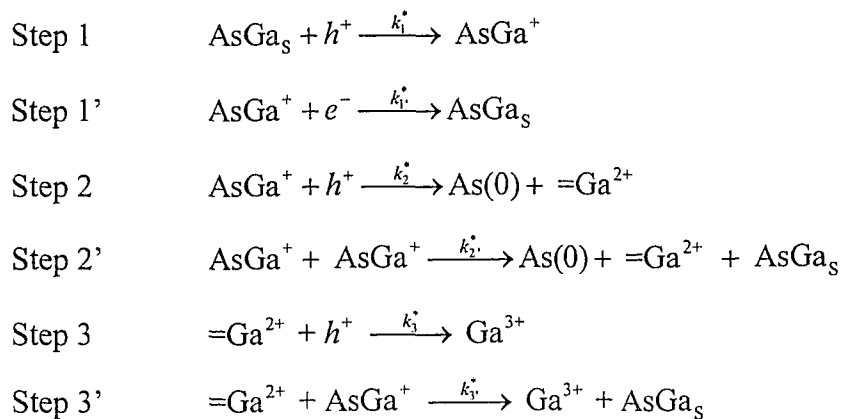
From comparison of the polarization curves under dark and daylight conditions in Figure 4-8, it is understood that the anodic decomposition of GaAs is a valence band process and GaAs is oxidized by holes. However, from the final products of As(III) and Ga(III) in several media, it is known that six charge transfers are involved. Do all these steps require holes as oxidants? The answer is yes based on the work of Allongue and Blonkowski [11, 24]. On the other hand, the work from the group of Vanmaekelbergh and Gomes suggested that in most aqueous solutions, corrosion is via the X-C mechanism. The only evidence is indirect from the current-voltage behavior of GaAs corrosion in several solutions with and without stabilizing agents [7, 25]. The main difficulty in introducing an intermediate as the oxidant is the assumption that this intermediate must be able to move freely at the surface. For the simulation below, this assumption is followed to examine whether impedance spectra can conform to the experimental results via an X-C mechanism.

AsGa$^+$ and =Ga^{2+} are treated as surface absorbates or adsorbates?. They are assumed to occupy θ_1 and θ_2 fractions of the electrode surface respectively for AsGa$^+$ and =Ga^{2+} and the surface coverage unoccupied by these intermediates (AsGa)$_s$ is $(1-\theta_1-\theta_2)$. Reactions rates, the current density and the time dependence of the surface coverage can be written as follows:

$$v_1 = (1-\theta_1-\theta_2)p_s k_1^*$$
(5.21)

$$v_{1'} = k_{1'}^* n_s \theta_1$$
(5.22)

$$v_2 = k_2^* \theta_1 p_s$$
(5.23)

$$v_{2'} = k_{2'}^* \theta_1^2$$
(5.24)

$$v_3 = k_3^* \theta_2 p_s$$
(5.25)

$$v_{3'} = k_{3'}^* \theta_1 \theta_2$$
(5.26)

$$j = F(v_1 - v_{1'} + v_2 + v_{2'} + v_3 + v_{3'})$$
(5.27)

$$\beta_a \frac{d\theta_1}{dt} = v_1 - v_{1'} - v_2 - 2v_{2'} - v_{3'}$$

(5.28)

$$\beta_a \frac{d\theta_2}{dt} = v_2 + v_{2'} - v_3 - v_{3'}$$

(5.29)

In these equations v_i is the reaction rate of the ith reaction step, β_a is a factor to convert surface fraction to concentration and F is the Faraday constant. To understand how these reaction rate constants influence the impedance spectra shape, two limiting situations are considered.

1. Depletion layer control

For n-type GaAs under anodic polarization conditions, the space charge region is depleted of majority carriers (electrons). Under ideal conditions, *i.e.*, no surface states and the double layer capacitance is large enough, the potential applied entirely falls within the depletion layer. As a result, the concentration of charge carriers is fully controlled by the applied potential through band bending according to the simple Boltzmann distribution:

$$n_s = n_0 \exp\left(\frac{-e\varphi_{SC}}{k_B T}\right)$$

(5.30)

$$p_s = p_0 \exp\left(\frac{e\varphi_{SC}}{k_B T}\right)$$

(5.31)

Unlike p-type semiconductors, an increase in the anodically applied potential on n-GaAs causes an increase in the band bending. Nevertheless, an increase in the anodically applied potential results in more holes at the surface. Since the potential drop in the solution double layer is not significantly affected by the applied potential, due to depletion layer control, the kinetic rate constants in (5.21)-(5.26) are independent of potential E.

2. Helmholtz layer control

168

Another limiting situation is where the applied potential entirely falls in the Helmholtz layer on the solution side. The band bending in the depletion layer is constant and irrelevant to the potential E and the hole concentration at the surface. The semiconductor is treated as a metal. The kinetic rate constants are exponentially dependent on the applied potential:

$$k_i^* = k_i^{*0} \exp\left(\frac{\alpha_i n_i e \varphi_H}{kT}\right) \tag{5.32}$$

where α_i and n_i are the charge-transfer coefficient and the number of charges, respectively. k_i^{*0} is the kinetic constant corresponding to the exchange current density at equilibrium. Combining the rate constants, n_s and p_s, (5.27) can be re-written as (for simplicity, the surface concentration of H^+ is assumed to remain constant):

$$j = F[(1-\theta_1-\theta_2)k_1 - \theta_1 k_{1'} + \theta_1 k_2 + \theta_1^2 k_{2'} + \theta_2 k_3 + \theta_2\theta_1 k_{3'}] \tag{5.33}$$

The dependence of these new kinetic constants is different for the two kinds of limiting control, if the format of $k_i = k_i^0 \exp(b_i E)$ is utilized.

Under dark conditions and for depletion layer control

$$b_i = \frac{e}{kT} \quad (i = 1, 2, 3) \tag{5.34}$$

$$b_i = 0 \quad (i = 2', 3') \tag{5.35}$$

$$b_i = -\frac{e}{kT} \quad (i = 1') \tag{5.36}$$

Under Helmholtz layer control

$$b_i = \frac{\alpha_i e}{kT} \quad (i = 1, 2, 2', 3, 3') \tag{5.37}$$

$$b_i = -\frac{\alpha_i e}{kT} \quad (i = 1') \tag{5.38}$$

Under illumination conditions, all b_i values would be zero for depletion layer control and would follow (5.37) and (5.38) for Helmholtz layer control. From (5.27)-(5.29), the

169

steady-state current-voltage behavior can be calculated. In the steady state, the surface coverage of the reaction intermediates is considered as unvarying, giving

$$\frac{d\theta_1}{dt} = \frac{d\theta_2}{dt} = 0 \tag{5.39}$$

Since for the impedance measured, the main semicircle / arc, is due to a capacitor on the scale of the depletion layer instead of the typical solution double layer value, the limiting situation of Helmholtz layer control will be ignored and the discussion below only applies to the case of depletion layer control.

5.4.1 Impedance calculation

To calculate the impedance, it is assumed that a small-amplitude sinusoidal modulation of potential E is applied and sinusoidal variations of the surface coverage and the current density are produced. By doing the differentiation on (5.33) and (5.28)-(5.29), the faradaic impedance Z_F is obtained. Since under dark conditions, no recombination was found, step 1' is neglected below.

$$\delta j = F[k_1 b_1 (1 - \overline{\theta_1} - \overline{\theta_2}) + k_2 b_2 \overline{\theta_1} + k_2 b_2 \overline{\theta_1}^2 + k_3 b_3 \overline{\theta_1} + k_3 b_3 \overline{\theta_1 \theta_2}]\delta E$$
$$+ F(-k_1 + k_2 + 2k_2 \overline{\theta_1} + k_3 \overline{\theta_2})\delta\theta_1 + F(-k_1 + k_3 \overline{\theta_1})\delta\theta_2 \tag{5.40}$$

$$\beta_a i\omega\delta\theta_1 = [k_1 b_1 (1 - \overline{\theta_1} - \overline{\theta_2}) - k_2 b_2 \overline{\theta_1} - 2k_2 b_2 \overline{\theta_1}^2 - k_3 b_3 \overline{\theta_1 \theta_2}]\delta E$$
$$+ (-k_1 - k_2 - 4k_2 \overline{\theta_1} - k_3 \overline{\theta_2})\delta\theta_1 + (-k_1 - k_3 \overline{\theta_1})\delta\theta_2 \tag{5.41}$$

$$\beta_a i\omega\delta\theta_1 = [k_2 b_2 \overline{\theta_1} + k_2 b_2 \overline{\theta_1}^2 - k_3 b_3 \overline{\theta_2} - k_3 b_3 \overline{\theta_1 \theta_2}]\delta E$$
$$+ (k_2 + 2k_2 \overline{\theta_1} - k_3 \overline{\theta_2})\delta\theta_1 + (-k_3 - k_3 \overline{\theta_1})\delta\theta_2 \tag{5.42}$$

$\overline{\theta_1}$ and $\overline{\theta_2}$ are the surface coverages at steady state, ω is the angular frequency $(2\pi f)$ and $i = \sqrt{-1}$. The Faradaic impedance is defined as $Z_F = \dfrac{\delta V_{app}}{\delta j}$ and the total impedance Z can be obtained by parallel combination with the space charge layer capacitance and then putting in series with the double layer impedance.

170

$$\frac{1}{Z_F} = \frac{\delta j}{\delta V_{app}} = \frac{1}{R_t} + M\frac{\delta\theta_1}{\delta V_{app}} + N\frac{\delta\theta_2}{\delta V_{app}} \qquad (5.43)$$

$$R_t = \frac{1}{F[k_1 b_1 (1-\overline{\theta_1}-\overline{\theta_2}) + k_2 b_2 \overline{\theta_1} + k_{2'} b_{2'} \overline{\theta_1}^2 + k_3 b_3 \overline{\theta_1} + k_{3'} b_{3'} \overline{\theta_1}\overline{\theta_2}]} \qquad (5.44)$$

$$M = F(-k_1 + k_2 + 2k_{2'}\overline{\theta_1} + k_{3'}\overline{\theta_2}) \qquad (5.45)$$

$$N = F(-k_1 + k_{3'}\overline{\theta_1}) \qquad (5.46)$$

$\dfrac{\delta\theta_1}{\delta V_{app}}$ and $\dfrac{\delta\theta_2}{\delta V_{app}}$ can be obtained by solving (5.41) and (5.42).

From the simulation, only when $k_{2'} \gg k_1^0, k_2^0$ is an inductive loop observed at high potential, instead of low potentials. When $k_{2'} \sim k_1^0, k_2^0$, an inductive loop can be always obtained. The former conforms to our experimental results. The calculated impedance curves are shown in Figure 5-10 by assigning appropriate values to the parameters, obtained from the literature [3, 11]. In order to match the Tafel slope observed (~300 mV/decade), the b_i values were adjusted to $\dfrac{e}{6kT}$ for (i = 1, 2, 3). It is shown in Figure 5-10that with a progressive potential increase, the Faradaic impedance is initially a capacitive loop (Figure 5-10a) at 400 mV and then converts to a pair of capacitive and inductive loops (Figure 5-10b) at 900 mV. The capacitive loop at lower potentials, as shown in Figure 5-10a, would be overlapped by the capacitive loop due to the space charge layer, which is a much smaller capacitor. At higher potentials close to breakdown, the pair of loops is separated from the space charge region capacitance giving an impedance spectrum as shown in Figure 4-22, 4-24. The other capacitive loop appearing at the low frequency part in these figures with the inductive loop is probably from the additional reaction at the breakdown potential (e.g., further oxidation of As(0) in parallel with the double layer capacitor, which is a combination of R_{ct2} and C_{dl} in Figure 4-25b and d.

171

5.4.2 H-C or X-C mechanism

From literature on the impedance studies of anodic dissolution of metals [26], reduction of oxygen [27] and the hydrogen evolution reaction (HER) [28], it is known the inductive loop can only result from a Faradaic adsorption process. The reaction intermediates are all surface adsorbents if they are immobile and all the oxidation steps, excluding the final step to corrosion products, are Faradaic adsorption processes. Theoretically, a Faradaic adsorption must meet two conditions so that an inductive loop appears: (1) the Faradaic adsorption process is slow, being the rate-determining step; (2) the concentration of the resulting adsorbate must be high in order to be detectable. The possibility of these steps being the rate-determining step is discussed below.

Step 1: The slow reaction rate of step 1 and high concentration of $AsGa^+$ are more possible in the low anodic potential region, with small overpotentials or for n-GaAs in dark conditions with a low concentration of holes at the surface. If the inductive loop can be observed at high anodic potential, it should also appear in the low potential region, in conflict with the experimental results. Therefore, step 1 is not a possible source for the inductive loop and step 1 would be fast for most of the potentials studied.

Step 2: Step 2 can be the rate-determining step if (1) the hole concentration at the surface is low or (2) a small overpotenital is applied relative to the equilibrium potential. Similar to the discussion for step 1, the former case exists for n-GaAs in dark conditions and the latter might be more possible for low applied potential. Hence, step 2 is also not likely the source for the inductive loop.

Step 2': Compared to step 1 and 2, step 2' being the rate-determining step is easy to understand. Instead of a low hole concentration, a low concentration of $AsGa^+$ or small overpotentials might lead to step 2' being the rate-determining step. The concentration of $AsGa^+$ may be high at low applied potential, because of slow consumption of $AsGa^+$, and low at high applied potential, because of the fast step 3 or 3' with large overpotentials.

172

Based on the above discussion, the X-C mechanism with step 2' being the slowest oxidation step is favored. This does not mean that step 2 cannot occur; however, step 2 is only a by-reaction with step 2'.

The simulation of the impedance is better to show which mechanism, H-C or X-C, is suitable to describe the corrosion processes. From a series of quantitative calculations, it is found that three conditions must be met to have the capacitive and inductive loops appearing only at potential regions L3 and D3 in Figure 4-8. One is that $k_{2'}$ should be much larger than k_1 and k_2 at the mild potentials applied, i.e., potential regions L1, D1, L2 and D2. The other is that at the potential where impedance spectra show an inductive loop, k_1 is comparable to $k_{2'}$, while they are both much larger than k_2. The last one is that consumption of Ga(II) is much faster than its production, *i.e.*, the combined reaction rates of step 3 and 3' must be much larger than step 2'. These suggest that there are two different rate-determining steps in the corrosion regions before and after breakdown. At potentials before breakdown, due to small k_1, compared with k_2' and k_3', step 1 is the rate-determining step and the Tafel relationship in the dark holds, while under illumination a current plateau appears. On the other hand, in region L3, inductive loop observation indicates a faradaic adsorption process as the rate-determining step. Qualitatively, this slowest oxidation step cannot be a reaction involving holes because under illumination conditions, the inductive loop only emerges at high potentials, which is the same phenomenon observed for experiments carried out in the dark. This is referred to as the X-C mechanism.

From quantitative simulation, step 2' as the rate determining step is preferred in region L3. An additional conclusion is that the intermediate AsGa$^+$ must be able to freely move at the surface for step 2' to take place.

173

R_{MS} C_{MS}

(a)

$C_{Randles}$

$R_{Randles,1}$

$R_{Randles,2}$

(b)
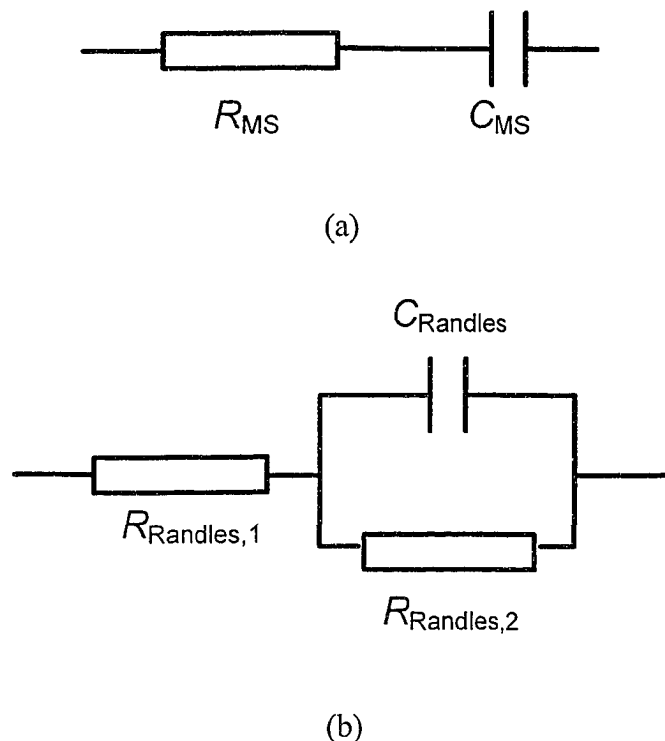
Figure 5-1 Equivalent circuits discussed in this work. (a) simple RC circuit, used in the direct Mott-Schottky measurements; (b) Randles circuit, used in the description of most electrochemical reactions.

$1/C^2$

Randle circuit

direct Mott-Schottky measurments

cathodic

E anodic

$V_{fb,MS}$ $V_{fb,Randles}$
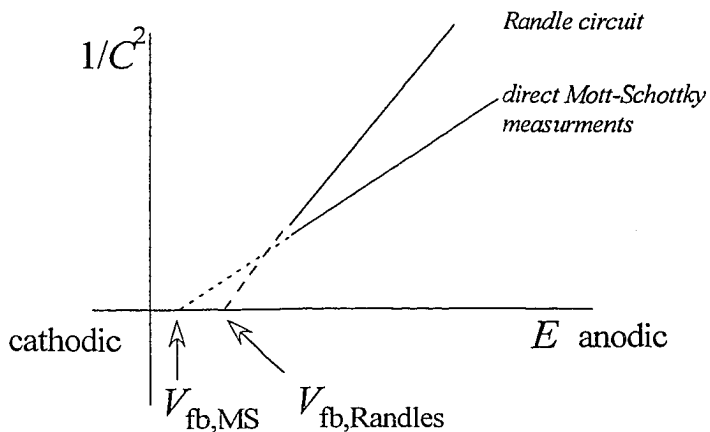
Figure 5-2 The discrepancy between the capacitance in Mott-Schottky plots from direct Mott-Schottky measurements and the capacitance from the more accurate Randles circuit for n-type GaAs. The more anodic the potential, the larger the expected discrepancy. A more negative flatband potential is obtained from direct Mott-Schottky measurements.

174
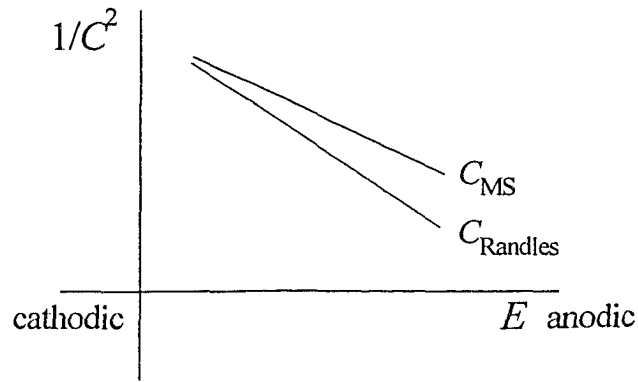
Figure 5-3 The discrepancy between the capacitance in Mott-Schottky plots from direct Mott-Schottky measurements and the capacitance from the more accurate Randles circuit for p-type GaAs. The more anodic the potential, the larger the expected discrepancy.
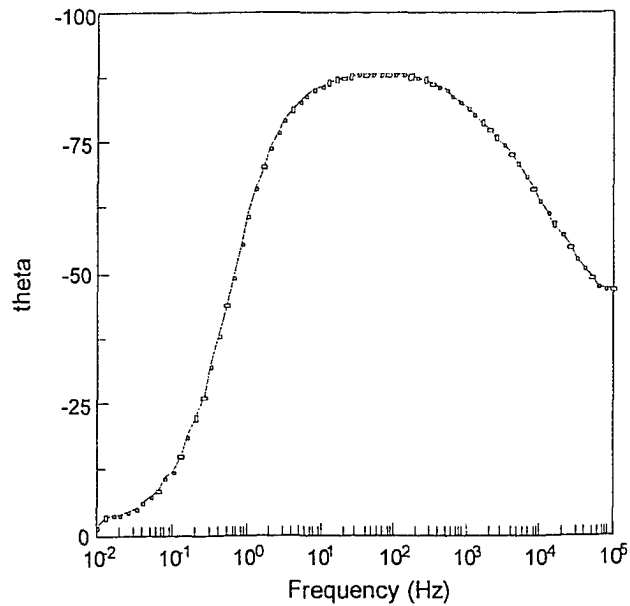
Figure 5-4 A typical Bode plot (phase angle vs. frequency) of the impedance spectrum for n-GaAs in 0.5 M H_2SO_4 solution at 0.45 V vs. SCE under illumination conditions.

175
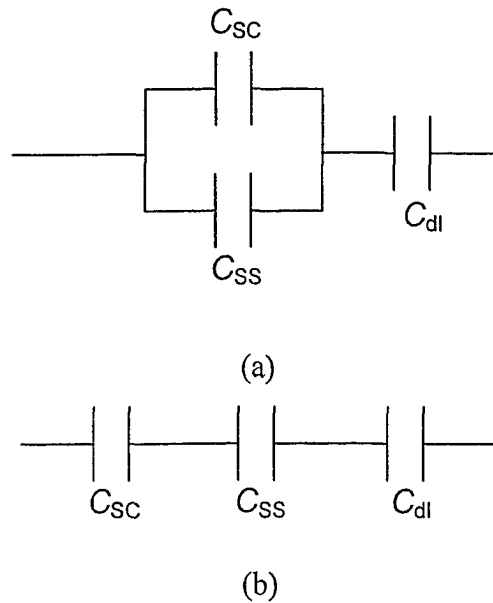
Figure 5-5 Relationship for the capacitance due to a space charge region (C_{SC}), surface states (C_{SS}) and a double layer (C_{dl}). Normally, C_{SC} is in parallel with C_{SS}, sharing the potential drop (a). Sometimes, when the source of surface states is a relatively compact layer (surface coverage is sufficiently high and the surface is flat), C_{SC} is in series with C_{SS} (b). In such a case, the potential applied falls into three parts, with the portion dependent on the relative values of these capacitors.

Table 5-1 Calculated results for the Fermi energy level and effective doping density for different doping levels in n-GaAs using the Nilsson approximation (Appendix A).

Doping Density (cm^{-3})	E_F-E_C (eV)	Effective Doping Density (cm^{-3})
1.0×10^{17}	-0.04644	7.05×10^{16}
1.0×10^{18}	-0.003183	3.10×10^{17}
1.3×10^{18}	0.001362	3.55×10^{17}
2.0×10^{18}	0.008749	4.41×10^{17}
5.0×10^{18}	0.02433	6.71×10^{17}

176

Table 5-2 Experimental breakdown potentials for different doping levels in *n*-GaAs.

doping density (cm^{-3})	breakdown potential V_{br} (V) vs. SCE	calculated depletion width using V_{fb} = -0.85 V vs. SCE(nm)
1.0×10^{17}	0.97	192
1.3×10^{18}	0.78	78
2.0×10^{18}	0.73	69
5.0×10^{18}	0.51	50

Table 5-3 Theoretical value of breakdown band bending and depletion region width.

doping density (cm^{-3})	effective doping density (cm^{-3})	breakdown band bending (eV)	depletion region width (nm)
1.0×10^{17}	7.05×10^{16}	8.25	0.412
1.0×10^{18}	3.10×10^{17}	1.88	0.0938
1.3×10^{18}	3.55×10^{17}	1.64	0.0819
2.0×10^{18}	4.41×10^{17}	1.32	0.0659
5.0×10^{18}	6.71×10^{17}	0.87	0.0433
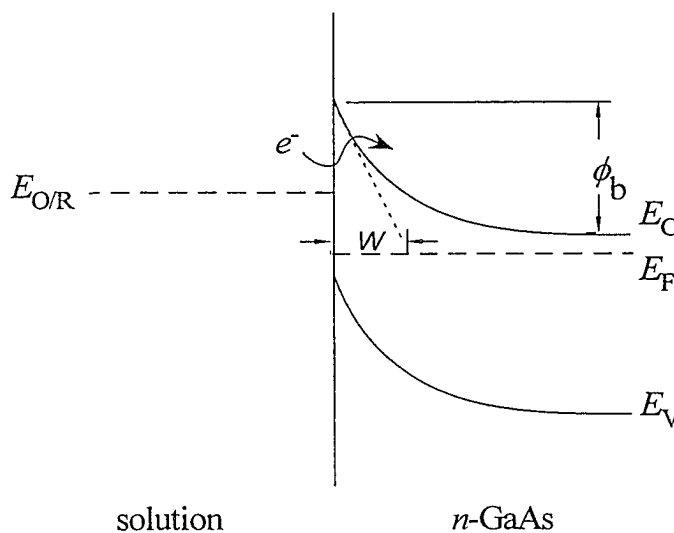
solution   *n*-GaAs

Figure 5-6 Schematic illustration of the tunneling of electrons from the solution to *n*-GaAs at a large band bending and narrow depletion region. W: depletion width; E$_{O/R}$: potential of the redox couple O/R in solution; ϕ_b: band bending.
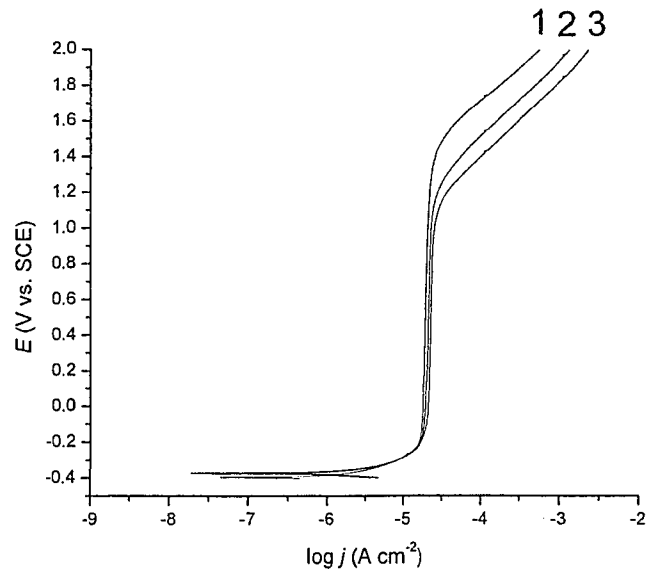
Figure 5-7 Breakdown potential for different surface conditions. The three curves were obtained from the same sample: (1) a fresh surface after etching and cleaning; (2) sample (1) after a further cleaning; and (3) sample (2) after another cleaning. Doping density: 1.0×10^{17} cm^{-3}.
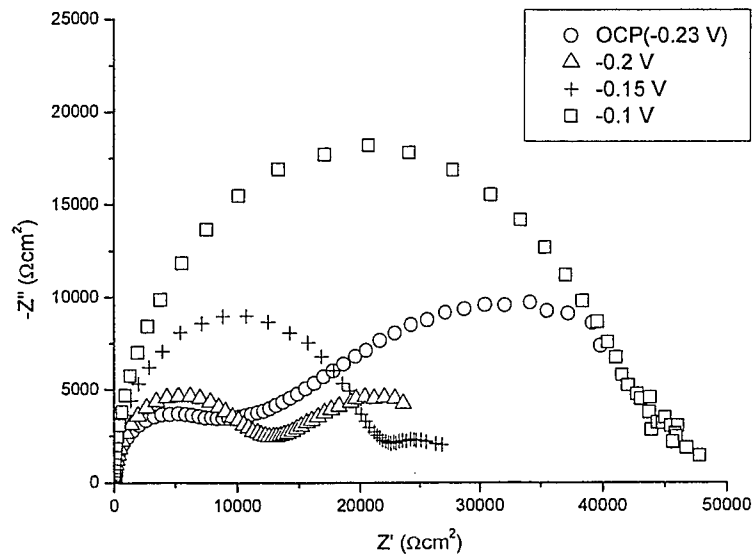
Figure 5-8 Impedance spectra for n-GaAs (1×10^{18} cm^{-3}) in 0.5 M H$_2$SO$_4$ at and close to open circuit potential under daylight conditions, illustrating recombination impedance. o: OCP; Δ: -200 mV; +: -150 mV; $\square$: -100 mV.

178
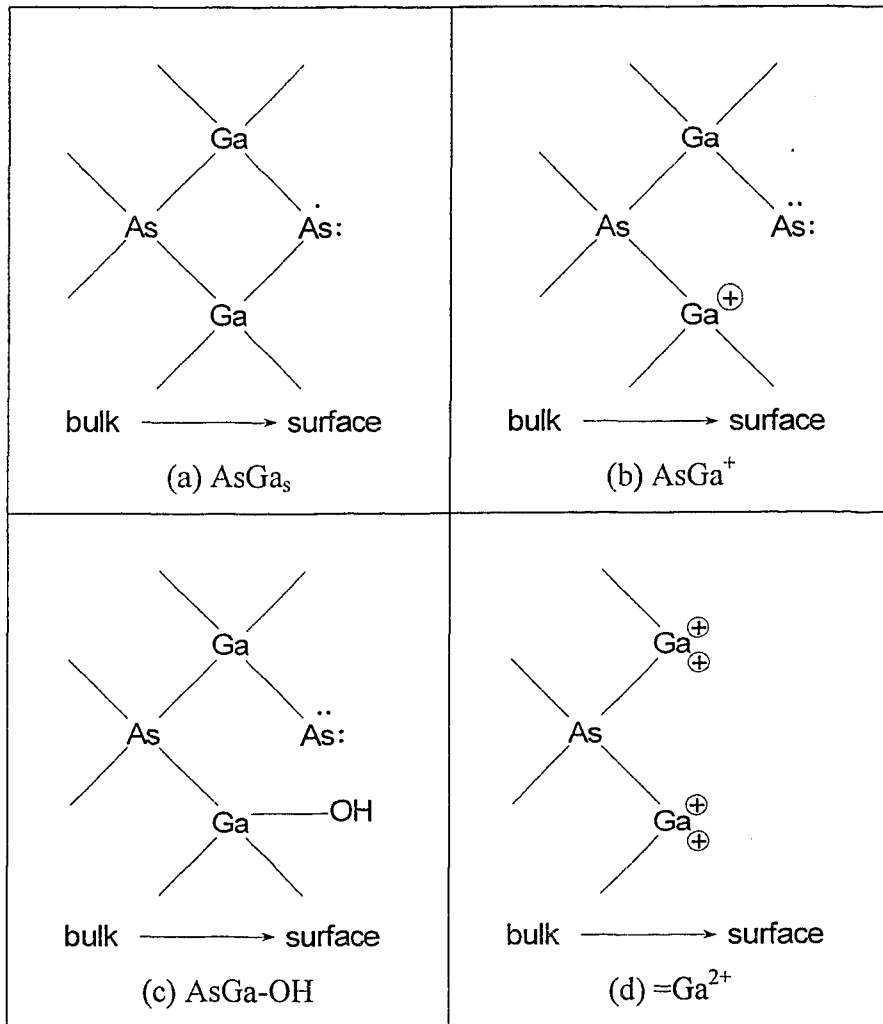
Figure 5-9 Schematic illustration for the corrosion intermediates of the GaAs (100) surface. Detailed information is presented in the text.
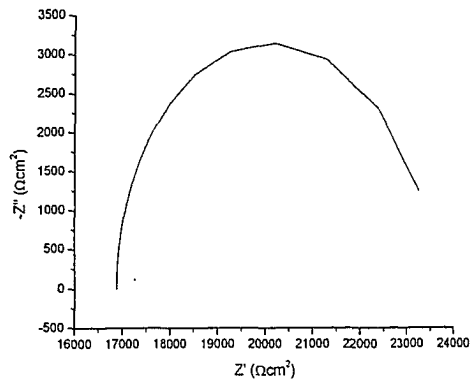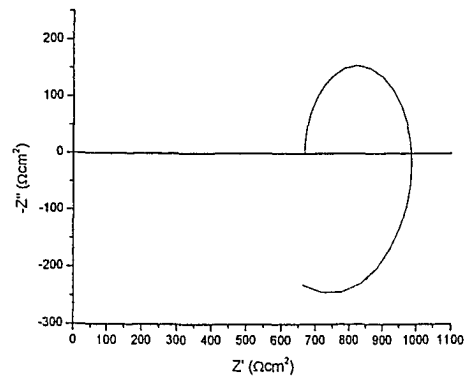
(a) at 400 mV　　　　　　　　　　　　(b) at 900 mV

Figure 5-10 Impedance spectra calculated from the model at different potentials. The impedance shown is the part only from the Faraday reactions, not including the space charge layer capacitor and the double layer. Parameters used in the simulation are: $\beta = 10^{-6}$ mol cm^{-2}, $k_1^0 = 8.0 \times 10^{-10}$ mol cm^{-2} s^{-1}, $k_{1'}^0 = 1.0 \times 10^{-12}$ mol cm^{-2} s^{-1}, $k_2^0 = 5.0 \times 10^{-12}$ mol cm^{-2} s^{-1}, $k_{2'}^0 = k_3^0 = 1.0 \times 10^{-7}$ mol cm^{-2} s^{-1}, $k_{3'}^0 = 1.0 \times 10^{-12}$ mol cm^{-2} s^{-1} [3, 11].

180

References:

[1]   Cardon, F. and Gomes, W. P., *J. Phys. D: Appl. Phys.* **1978**, 11, L63.

[2]   Bard, A. J. and Faulkner, L. R. *Electrochemical Methods: Fundamentals and Applications*; John Wiley & Son Press: 1980.

[3]   Cattarin, S. and Musiani, M., *J. Electroanal. Chem.* **2004**, in printed.

[4]   Batchelor, R. A. and Hamnett, A. In *Modern Aspects of Electrochemistry*; Bockris, J. O. M., et al., Ed.; Vol. 22; Plenum Press: 1992.

[5]   Singh, J. *Semiconductor Devices: Basic Principles*; John Wiley & Sons, Inc.: 2001.

[6]   Zeghbroeck, B. V. *Principles of Semiconductor Devices*; http://ece-www.colorado.edu/~bart/book/: 2004.

[7]   Gomes, W. P. and Goossens, H. H. In *Advances in Electrochemical Science and Engineering*; Gerischer, H. and Tobias, C. W., Ed.; Vol.; VCH: Weinheim, 1994.

[8]   Vanmaekelbergh, D., Rigole, W., Gomes, W. P. and Cardon, F., *J. Chem. Soc., Faraday Trans.* **1983**, 79, 2813.

[9]   Vanmaekelbergh, D., Gomes, W. P. and Cardon, F., *J. Electrochem. Soc.* **1982**, 129, 546.

[10]   Vanmaekelbergh, D. and Cardon, F., *J. Phys. D: Appl. Phys.* **1986**, 19, 643.

[11]   Allongue, P. and Blonkowski, S., *J. Electroanal. Chem.* **1991**, 317, 78.

[12]   Hens, Z. and Gomes, W. P., *J. Phys. Chem.* **2000**, B 104, 7725.

[13]   Solomun, T., McIntyre, R., Richtering, W. and Gerischer, H., *Surf. Sci.* **1986**, 169, 414.

[14]   Lingier, S. and Gomes, W. P., *Ber. Bunsenges. Phys. Chem.* **1991**, 95, 170.

[15]   Steer, C. A., Weng, G. S., Luo, J. L. and Ivey, D. G., *Electrochemistry Communications* **2000**, 292, 754.

[16]   Gerischer, H., *Faraday Discussion* **1981**, 70, 137.

[17]   Allongue, P. and Cachet, H., *J. Electrochem. Soc.* **1984**, 131, 2861.

[18]   Erne, B. H., Ozanam, F. and Chazalviel, J.-N., *J. Phys. Chem.* **1999**, B 103, 2948.

181

[19] Erne, B. H., Stchakovsky, M., Ozanam, F. and Chazalviel, J.-N., *J. Electrochem. Soc.* **1998**, 145, 447.

[20] Chazalviel, J.-N., Erne, B. H., Maroun, F. and Ozanam, F., *J. Electroanal. Chem.* **2001**, 509, 108.

[21] Chazalviel, J.-N., Belaidi, A., Safi, M., Maroun, F., Erne, B. H. and Ozanam, F., *Electrochim. Acta* **2000**, 45, 3205.

[22] Li, J. and Peter, L. M., *J. Electroanal. Chem.* **1986**, 199, 1.

[23] Erne, B. H., Vanmaekelbergh, D. and Vermeir, I. E., *Electrochim. Acta* **1993**, 38, 2559.

[24] Allongue, P. and Blonkowski, S., *J. Electroanal. Chem.* **1991**, 317, 57.

[25] Vanmaekelbergh, D. and Gomes, W. P., *J. Phys. Chem.* **1990**, 94, 1571.

[26] Ma, H., Cheng, X., Chen, S., Wang, C., Zhang, J. and Yang, H., *J. Electroanal. Chem.* **1998**, 451, 11.

[27] Itagaki, M., Hasegawa, H., Watanabe, K. and Hachiya, T., *J. Electroanal. Chem.* **2003**, 557, 59.

[28] Harrington, D. A. and van den Driessche, P., *J. Electroanal. Chem.* **2001**, 501, 222.

Chapter 6   Conclusions and future work

Based on the studies and discussion presented in the last chapters, the following conclusions are made and possible future work is discussed.

6.1 Conclusions

1. OCP: Systematic investigation has been performed on the response of the OCP of GaAs under various conditions, including the semiconductor itself and solution contents. It was found that the GaAs surface is very sensitive to aqueous solutions. Generally ~20 minutes is required to reach stabilization equilibrium between GaAs and the solution. As the charge carrier concentration at surface is changed with the doping level and illumination conditions, the influence of doping level was found to be more prominent for p-GaAs than n-type. The effect of light is more prominent for n-GaAs. The dependence of OCP on the solution pH values was obtained as ~54 mV per pH unit, slightly smaller than the 59 mV per pH unit, suggested from the Nernst equation. In addition, the effect of two metal ions, Cu^{2+} and Ni^{2+}, was studied. Sufficient addition of Cu^{2+} (higher than 0.033 M) can fully pin the OCP, while Ni^{2+} is less effective.

In comparison with the theory, it is then concluded that the OCP of GaAs is not ideal. The OCP is not simply determined either by GaAs, the case for an inert semiconductor electrode, or by the solution, the case for an inert metal electrode. The quantitative results show that the solution side may have a larger impact on the OCP than the GaAs side. This may be due to the relatively high doping level samples used in this work.

183

2. Steady-state polarization: the current-voltage behavior apparently showed that the corrosion of GaAs is a VB process, because p-GaAs corrodes much faster than n-type and n-GaAs under illumination condition had a limiting current. The steady-state polarization curves for n-GaAs in dark conditions and p-GaAs showed Tafel regions, where the slopes were~350-400 mV per decade and ~110-130 mV for p-GaAs for n-GaAs and p-GaAs respectively. The reasons for the unexpectedly high Tafel slope for n-GaAs in dark conditions remains unknown. For p-GaAs, the obtained Tafel slope can be explained in terms of the slow oxidation steps, in contrast to the fast hole generation rate.

At sufficiently high anodic potentials, n-GaAs breaks down and p-GaAs passivates. Passivation of p-GaAs is explained by the slow dissolution of the corrosion product away from the surface. For n-GaAs, easier breakdown was found for the higher doping level samples. This excludes inversion layer formation as the mechanism for breakdown. Calculation of the width of space charge region at breakdown potential showed that tunneling was unlikely and avalanche breakdown was the only choice to account for the breakdown. However, band bending at the breakdown potential was found to be much smaller than that for a metal-GaAs Schottky contact. This was explained by the presence of defects at the GaAs surface, which can result from the etching and cleaning procedures and intrinsic dislocations. Experiments also showed that the rougher the n-GaAs surface, the earlier the onset of breakdown.

3. Flatband potential and band bending: Flatband potentials for both n- and p-GaAs were obtained from direct Mott-Schottky measurements and the fitted impedance spectra. The flatband potential in the basic solution was more negative than that in the acidic solution. Due to the instability of GaAs in the aqueous solutions, the simple equivalent circuit in direct Mott-Schottky measurement was not sufficient to describe the interface. Discrepancies between the two measurement methods were discussed and the suggested frequency range for direct Mott-Schottky measurement

was given (> 15 Hz). It was also pointed out that using high frequency is not always good, especially for the samples used in this thesis work, *i.e.*, epitaxial layers on a GaAs substrate. Flatband potentials obtained by fitting the impedance spectra were more reliable and can be used to calculate the band bending.

4. Mechanism: The mechanism for GaAs corrosion was mainly inferred from the polarization curves and impedance spectra results. The major difference in polarization curves for *n*-GaAs under dark and illumination conditions occurred because of the difference in hole concentration at the surface, which suggested that at potentials before breakdown the capture of holes was the slowest step in the overall process. Impedance investigation over the whole potential region from OCP to breakdown indicated that a different equivalent circuit must be used to fit the impedance spectra in the Tafel region and the breakdown region. Under illumination conditions, recombination impedance was observed in the potential region close to the OCP.

Simulation of the possible mechanisms for *n*-GaAs corrosion was carried out and the simulated results were compared to the experimental data. It was shown that while the breaking of the first bond is the rate-determining step at potentials before breakdown, further oxidation of the corrosion intermediate ($AsGa^+$) by itself becomes the slowest step after breakdown, resulting in an inductive loop in impedance spectra. After breakdown, due to the high concentration of charge carriers at surface, the potential applied did not fall mainly in the space charge region. The potential distribution across the Helmholtz layer had to be considered, which could explain the additional capacitive loop in the impedance spectra.

In summary, the objectives set out in Chapter 2 have been accomplished. The true flatband potential from impedance spectroscopy fitting has been obtained (Objective 2 in Section 2.4). This flatband potential can be used to determine the band bending at the surface in a given potential region, i.e., from OCP to potentials before breakdown in which a depletion layer is formed at the interface. However,

185

when GaAs reaches breakdown, the potential applied mainly falls in the double layer, and surface charge concentration does not depend on the applied potential in the same way as before (Objective 2). From comparison of theoretical calculations and experimental results on breakdown potential, the breakdown mechanism was determined as avalanche in nature (Objective 5). The effects of doping levels on GaAs corrosion, including OCP, flatband potential, polarization curves and the corroded surface composition / morphologies, have been fully investigated (Objective 4). Finally, the decomposition mechanism for GaAs has been simulated and rate determining steps for different applied potential regions have been identified (Objective 3).

6.2 Future work

Possible future work in this topic includes:

1. Understanding of the Tafel slope for n-GaAs corrosion. The unusually large Tafel slope cannot be explained by the proposed mechanism and potential distribution presently.

2. More detailed examination of the surface composition for corroded GaAs is necessary. It is expected that the surface composition after corrosion in different potential regions is not the same.

3. The temperature dependence of the corrosion behavior can be examined to understand more about the band bending and charge carrier concentration at the GaAs surface.

Appendix A: Accurate Fermi energy level calculations

Electrons in material at thermal equilibrium follow the Fermi-Dirac distribution, given by Eq. (2.1), which is repeated here.

$$f(E) = \frac{1}{1 + \exp\left(\dfrac{E - E_F}{kT}\right)} \tag{7.1}$$

The number of electrons per unit energy interval $n(E)$ is given by the product of $f(E)$ and the density of electron states DOS(E).

$$n(E) = f(E) \cdot \text{DOS}(E) \tag{7.2}$$

DOS(E) can be obtained from the classic $E^{1/2}$ density of states.

$$\text{DOS}(E) = \frac{1}{2\pi^2}\left(\frac{2m^*}{\hbar^2}\right)^{3/2} E^{1/2} \tag{7.3}$$

The number of electrons for the total system is the integral of electron energy from zero to infinity.

$$N = \int_0^\infty n(E)dE = \int_0^\infty f(E) \cdot \text{DOS}(E)dE \tag{7.4}$$

Plugging in the expression of DOS(E), $i.e.$ Eq. (7.4) results in

$$N = \frac{1}{2\pi^2}\left(\frac{2m^* kT}{\hbar^2}\right)^{3/2} F\left(\frac{E_F}{kT}\right) \tag{7.5}$$

where $F(x)$ is called the Fermi integral:

187

$$F(x) = \int_0^{\infty} \frac{y^{1/2}}{1 + \exp(y - x)} dy \qquad (7.6)$$

The Fermi integral cannot be simply solved. Several kinds of approximations have been proposed so far. The three commonly used are Maxwell-Boltzmann approximation, Joyce-Dixon approximation and Nilsson approximation.

The Maxwell-Boltzmann works well for semiconductors at low doping levels, in which the Fermi energy level is far enough from E_c and E_v. Based on this, the Fermi integral can be simplified as

$$F(x) = \int_0^{\infty} \frac{y^{1/2}}{1 + \exp(y - x)} dy = \int_0^{\infty} y^{1/2} \exp(x - y) dy$$

$$= \exp(x) \int_0^{\infty} y^{1/2} e^{-y} dy = \exp(x) \cdot \frac{\sqrt{\pi}}{2} \qquad (7.7)$$

Therefore

$$n(E) = N_C \exp\left(\frac{E - E_F}{kT}\right) \qquad (7.8)$$

The Joyce-Dixon approximation is based on this equation

$$\frac{E_F - E_C}{kT} = \log \frac{N}{N_C} + \frac{1}{\sqrt{8}} \frac{N}{N_C} - \dots \qquad (7.9)$$

This approximation is valid for all cases in which the Fermi energy level is below the CB, that is, the semiconductor is non-degenerate.

The Nilsson approximation which is accurate within about 1% is obtained from this equation

$$\frac{E_F - E_C}{kT} = \frac{\log \dfrac{N}{N_C}}{1 - \dfrac{N}{N_C}} + \left(\frac{3\sqrt{\pi} \dfrac{N}{N_C}}{4}\right)^{2/3} + \frac{8\sqrt{\pi} \dfrac{N}{N_C}}{3\left(4 + \sqrt{\pi} \dfrac{N}{N_C}\right)^2} \qquad (7.10)$$

188

This method is used in this thesis for accurate calculation of Fermi energy because it can also be used for degenerate semiconductors, e.g., for n-GaAs at doping of 5×10^{18} cm^{-3}.

Because of high doping levels, the effective ionization of the dopant is another issue should be considered. The equations used in this thesis are as follows.

$$N_D(\text{effective}) = \frac{N_D}{1 + 2\exp\left(\frac{E_F + E_D}{kT}\right)} \tag{7.11}$$

and

$$N_A(\text{effective}) = \frac{N_A}{1 + 4\exp\left(\frac{E_F - E_A}{kT}\right)} \tag{7.12}$$

E_D and E_A are the energy levels of donors and acceptors respectively.

Combining Eqs (7.10) and (7.11) or (7.12), the effective doping level and Fermi energy level can be accurately obtained by iterative mathematic calculations.

References:

http://www.stanford.edu/class/ee243/course-reader/ee243_02_sec1.pdf

189

Appendix B: Basic parameters for GaAs and Si

@ 300K

Parameters	GaAs	Si
Crystal structure	Zinc Blende	Diamond
Group of symmetry	T_d^2-F43m	O_h^7-Fd3m
Number of atoms in 1 cm3	$4.42 \cdot 10^{22}$	$5 \cdot 10^{22}$
de Broglie electron wavelength	24 nm	n/a
Debye temperature	360 K	640 K
Density	5.32 g cm^{-3}	2.329 g cm^{-3}
Dielectric constant (static)	12.9	11.7
Effective electron mass m_e	$0.063 m_o$	$0.98 m_o$, $0.19 m_o$
Effective hole masses m_h	$0.51 m_o$	$0.49 m_o$
Effective hole masses m_{lp}	$0.082 m_o$	$0.16 m_o$
Electron affinity	4.07 eV	4.05 eV
Lattice constant	0.565325 nm	0.5431 nm
Optical phonon energy	0.035 eV	0.063 eV

190